APPLICATION OF THE FINITE ELEMENT
METHOD TO THE SCATTERING OF A
TWO-DIMENSIONAL, SEMI-INFINITE
PERIODIC STRUCTURE

THESIS
Perry N. Villanueva
Captain, USAF

AFIT/GE/ENG/99M-31

19990413 085   0

REPORT DOCUMENTATION PAGE			*Form Approved* OMB No. 0704-0188

1. AGENCY USE ONLY *(Leave blank)*	2. REPORT DATE March 1999	3. REPORT TYPE AND DATES COVERED Master's Thesis	

4. TITLE AND SUBTITLE
APPLICATION OF THE FINITE ELEMENT METHOD TO THE SCATTERING OF A TW0-DIMENSIONAL, SEMI-INFINITE PERIODIC STRUCTURE

5. FUNDING NUMBERS

6. AUTHOR(S)
Perry N. Villanueva, Captain, USAF

7. PERFORMING ORGANIZATION NAME(S) AND ADDRESS(ES)
Department of Electrical and Computer Engineering
Air Force Institute of Technology
2950 P Street
WPAFB, OH 45433-7765

8. PERFORMING ORGANIZATION REPORT NUMBER

AFIT/GE/ENG/99M-31

9. SPONSORING/MONITORING AGENCY NAME(S) AND ADDRESS(ES)
Dr. Kueichien C. Hill
AFRL/XPN
2951 K Street
WPAFB, OH 45433-7602
(937) 255-0277 / DSN 785-0277 / Email: hillkc@alcove.wpafb.af.mil

10. SPONSORING/MONITORING AGENCY REPORT NUMBER

11. SUPPLEMENTARY NOTES
Major Peter J. Collins, PhD
COMM: (937) 255-6565 Ext. 4304 / DSN: 785-6565 Ext. 4304
peter.collins@afit.af.mil

12a. DISTRIBUTION AVAILABILITY STATEMENT

Approved for public release; distribution unlimited

12b. DISTRIBUTION CODE

13. ABSTRACT *(Maximum 200 words)*

Infinite periodic structures have been studied heavily because of their efficient filtering capabilities. They generally exhibit sharp frequency roll-offs at the frequency band of interest. In the RF region of the electromagnetic spectrum, periodic structures find applications such as radomes and photonicbandgap materials. Most studies have been done with infinitely periodic arrays because it is convenient to collapse an infinite array into one representative period using Floquet Analysis. Truncating an infinite array introduces an edge and invalidates Floquet analysis over the entire array.

This thesis formulates a Finite Element Method (FEM) solution of a semi-infinite periodic array consisting of infinite cylinders. The array elements sufficiently far from the edge are implemented using the concept of a Physical Basis Function (PBF). The PBF concept is based on an a priori knowledge that the amplitudes of the currents in the periodic elements that are sufficiently far from an edge are constant. Implementation of the PBF concept allows the solution domain of the FEM to be bounded by introducing a periodic boundary that represents the truncated portion of the periodic array.

The periodic boundary is implemented by relating the fields there with a Floquet phase factor based on one periodic element external to the FEM domain. Performance of the periodic boundary at normal incidence is promising. At off-normal incidence, the implemented boundary performs poorly. Implementation of a periodic boundary by relating the fields there with a Floquet phase factor with one interior periodic element is the next stage in improving off-normal incidence performance.

14. SUBJECT TERMS
Computational Electromagnetics, Finite Element Method, Semi-Infinite Periodic Arrays

15. NUMBER OF PAGES 128

16. PRICE CODE

17. SECURITY CLASSIFICATION OF REPORT UNCLASSIFIED	18. SECURITY CLASSIFICATION OF THIS PAGE UNCLASSIFIED	19. SECURITY CLASSIFICATION OF ABSTRACT UNCLASSIFIED	20. LIMITATION OF ABSTRACT UL

The views expressed in this thesis are those of the author and do not reflect the official policy

or position of the Department of Defense or the United States Government.

APPLICATION OF THE FINITE ELEMENT METHOD TO THE

SCATTERING OF A TWO-DIMENSIONAL, SEMI-INFINITE

PERIODIC STRUCTURE

THESIS

Presented to the Faculty of the School of Engineering

of the Air Force Institute of Technology

Air University

In Partial Fulfillment of the

Requirements for the Degree of

Master of Science in Electrical Engineering

Perry N. Villanueva, B.S.E.E.

Captain, USAF

March 1999
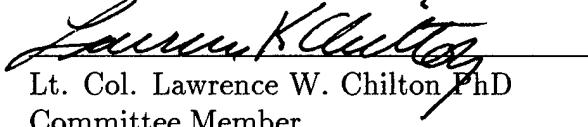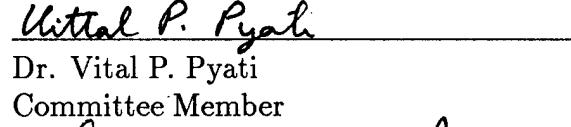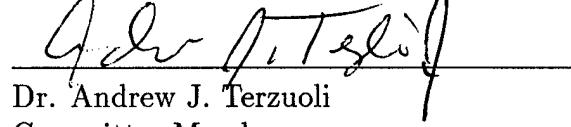
APPLICATION OF THE FINITE ELEMENT METHOD TO THE

SCATTERING OF A TWO-DIMENSIONAL, SEMI-INFINITE

PERIODIC STRUCTURE

Perry N. Villanueva, B.S.E.E.

Captain, USAF

Approved:

|	
Maj. Peter J. Collins PhD Thesis Advisor	11 MAR 99 Date
Lt. Col. Lawrence W. Chilton PhD Committee Member	11 Mar 99 Date
Dr. Vital P. Pyati Committee Member	11 Mar 99 Date
Dr. Andrew J. Terzuoli Committee Member	11 Mar 99 Date

Dedication

To my Lord and Savior Jesus Christ, for giving me knowledge, patience, guidance, and motivation; to my wife Jocelyn, whom I owe a lot for all she has done to free my time to pursue this research and for patiently and single handedly raising our children during my time at AFIT; and to my sons, Jonathan and Augustine, for reminding me oftentimes what the real meaning of life is all about, this thesis is humbly dedicated.

Acknowledgements

I would like to thank my advisor, Dr. Peter Collins for allowing me the oppurtunity to indulge in my interest in computational electromagnetics by giving me a very challenging, but important problem. To Dr. Lawrence Chilton for providing me with great advise in the mathematical aspects of the finite element method, I am truly grateful. To my sponsor, Dr. Kueichien Hill of AFRL/XPN, and to the the rest of my thesis committee, Drs. Andrew Terzuoli and Vittal Pyati, for their confidence and encouragement, and for critiquing this thesis. And finally, to all my Communications Lab roomies and my LO/EMAG classmates for all the times we shared, studying and otherwise, during this "significant emotional event" we call AFIT.

<div align="right">Perry N. Villanueva</div>

Table of Contents

List of Figures

List of Tables

xiv

Abstract

Infinite periodic structures have been studied heavily because of their efficient filtering capabilities. They generally exhibit sharp frequency roll-offs at the frequency band of interest. In the RF region of the electromagnetic spectrum, periodic structures find applications such as radomes where they allow a certain band of frequencies to pass through, andphotonic bandgap materials that block transmission at selected frequency bands. Most studies have been done with infinitely periodic arrays because it is convenient to collapse an infinite array into one representative period using Floquet Analysis. In reality, infinite arrays are not physically realizable. However, truncating an infinite array introduces an edge and invalidates Floquet analysis over the entire array.

This thesis formulates a Finite Element Method (FEM) solution of a semi-infinite periodic array consisting of infinitely long cylinders. The array elements sufficiently far from the edge are implemented using the concept of a Physical Basis Function (PBF). The PBF concept is based on an *a priori* knowledge that the amplitudes of the currents in the periodic elements that are sufficiently far from an edge are constant. Implementation of the PBF concept allows the solution domain of the FEM to be bounded by introducing a periodic boundary that represents the truncated portion of the periodic array.

The periodic boundary is implemented by relating the fields there with a Floquet phase factor based on one periodic element external to the FEM domain. Performance of the periodic boundary at normal incidence is promising. At off-normal incidence, the performance of the implemented boundary is below expectations. Implementation of a periodic boundary by relating the fields there with a Floquet phase factor with one interior periodic element is the next stage in the pursuit of improving off- normal incidence performance.

APPLICATION OF THE FINITE ELEMENT METHOD TO THE SCATTERING OF A TWO-DIMENSIONAL, SEMI-INFINITE PERIODIC STRUCTURE

I. Introduction

Frequency selective surface (FSS) design and analysis, especially in the microwave region of the electromagnetic spectrum, has been studied heavily during the last three decades. Interest in the exploitation of periodic structures technology occured because FSSs exhibit very desirable filtering characteristics. For example, enclosing an electromagnetic scatterer or radiator within an FSS provides the means for restricting transmission in and out of the enclosure to a sharply defined band of frequencies. This effectively "hides" an active radiator and the cavity enclosed within the FSS from being detected at any other frequency outside of the designed transmission band. Shaping the FSS to conform to its environment also helps minimize specular reflections. Thus, aircraft designers are given more options in developing low radar cross section (RCS) platforms. These important FSS characteristics provide avenues for the implementation of the modern version of an ancient military strategy of attacking the enemy without warning or very minimal indication of an impending attack. This effective way of concealing objects behind a periodic structure is part of the modern warfare strategy we now call "stealth" technologies.

1.1 Background

Although the science of periodic structures can be traced back to the end of the last century, accurate calculations were not achievable until the introduction of digital computers [20]. Faster calculations thus enabled the deeper study of these structures and implementation of new technologies such as complex radomes, photonic bandgap materials and phased array structures, to name a few.
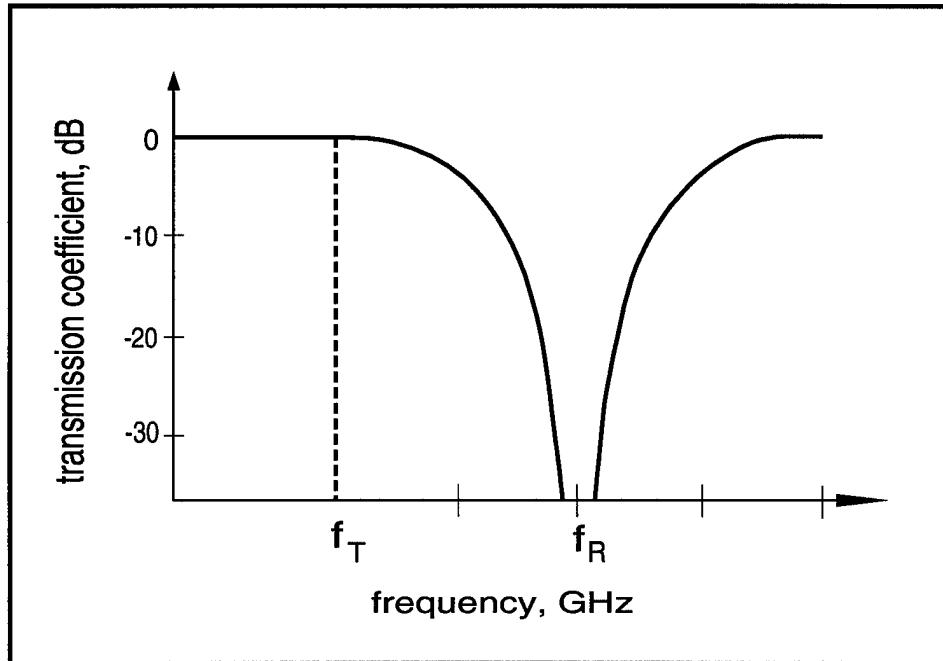
Figure 1.1   Typical Response of a Frequency Selective Surface [20].

Frequency selective surfaces behave as filters of electromagnetic waves. Their transmission and reflection properties vary with frequencies and incident angles. A typical response of an FSS is shown in Figure 1.1. In the figure, it shows that at a certain band of frequencies, the FSS acts as either a bandpass or a bandstop filter, depending on the physical characteristics of its periodic elements.

Periodic structures can be considered as one of two types. The first type consists of apertures of arbitrary shape "punched out" from a conducting sheet. The second type consists of conducting elements of arbitrary shape sandwiched inside a dielectric slab. Finite length dipoles are the simplest example for the second type [11].

The usual way of analyzing periodic structures is to take a representative period and designate it as a reference cell. For plane wave incidence, Floquet's periodicity condition stipulates that the amplitude of the field at any point in the array is equal to the field in the reference cell except for a phase factor. Essentially, Floquet analysis reduces an infinite domain problem to a finite domain one. Numerical techniques can then be utilized to calculate the structure's transmission

Traditionally, most "open region" or unbounded domain problems are numerically solved using the method of moments (MoM). The moment method provides a logical first step in the analysis of the scattering of periodic structures because the MoM is capable of determining the scattered fields by using an integral equation containing the free space Green's function that satisfies Sommerfeld's radiation boundary conditions. Integral equation techniques in their purest form, like the MoM for instance, are often restricted to computing the scattering from a limited number of geometries because implementation of the free space Green's function is often restricted to simple canonical forms. That makes the MoM computationally intensive when calculating complex geometries and geometries immersed in non-homogeneous dielectric materials without resorting to hybrid techniques.

More recently in the computational electromagnetics (CEM) field, partial differential equation (PDE) methods have come into greater use in scattering problems because of their ability to account for more complex geometries and inhomogeneous dielectric materials [10, 21]. The finite element method discretizes the problem domain into finite cells, also called grid or "mesh" elements. These mesh elements may be assembled from non-overlapping irregularly sized triangles or quadrilateral elements for two-dimensional space; tetrahedra or rectangular "bricks" for three- dimensional space. On the other hand, finite difference methods normally discretizes the problem domain with a uniformly spaced grid, preferably Cartesian [10].

PDE methods however require their problem domain to be finite. In order to characterize an infinite region normally associated with radiation and scattering problems, the PDE methods implement a fictitious boundary. Mathematically, this boundary allows incident energy to penetrate at the same time maintaining the the scattered field characteristics of outward propagation to infinity. The boundary must also prevent reflections back into the solution domain.

In real world applications, it is not possible to have infinitely long periodic surfaces. In the case of a radome, the surfaces have finite dimensions creating edges. With the advent of low observable large RCS contributors have been reduced to such an extent that edge effects

now become a major scattering source. Thus, edge effects become an increasingly important part of the analysis of the overall scattering of objects.

1.2 Problem Statement

In his dissertation, Collins [4] proposed an extension to Munk's [11] work to accommodate edges by using the concept of a "physical basis function" (PBF). Collins concluded that at some distance from an edge of a sufficiently long finite periodic structure, the perturbations in the amplitude of the currents induced by an incident field would approach a steady state. At this "central" location where a steady state amplitude is attained, Floquet analysis can be used to determine the impedance or admittance of the elements. Then, the central portion of the array is coupled to the edge element basis functions in a moment method solution.

The large computational expense of the moment method in calculating the scattered fields of complex scatterers and inhomogeneous materials prompted this research. FEM's ability to compensate for the MoM's shortfalls in the areas described above made it the likely candidate for this investigation. Thus, the objective of this research is to devise a Finite Element Method formulation for modeling a semi-infinite periodic array by incorporating the concept of a physical basis function as a model for array elements sufficiently far from edges.

1.3 Scope

The focus of this thesis is to establish the validity of the finite element method to solve truncated periodic structures. Thus, in order to perform a proof-of-concept, the simplest cases were considered. In this case it is appropriate to confine the solution domain to two-dimensional space. Confining the geometry to two dimensions makes it sufficient to use the scalar wave or Helmholtz equations without worrying about *spurious modes*[1].

---

[1]Spurious modes are artifacts of numerical calculations that often appear in the solution when using the vector Finite Element method. They have no physical meaning and are wrong answers [19].

The structure used to develop the concepts of this research consists of perfect electrical conducting (PEC) cylinders. Dielectric materials are not used other than the perfectly matched anisotropic (PMA) absorbing layers [15] on the boundary of the solution domain.

PMA layers are used to enclose the solution domain as opposed to an analytic boundary condition [2] in order to minimize the number of finite elements in the solution domain. The PMA absorbing boundary turns out to be a better choice for implementing a periodic boundary of a planar semi-infinite periodic structure since it allows a rectangular boundary. Rectangular boundaries enclose long slender objects without leaving a lot of free space in the solution domain. In contrast, the analytic boundary method requires a circular boundary.

1.4 Thesis Organization

The remainder of this thesis is organized as follows. Chapter 2 provides the electromagnetics background for the Finite Element Method applied to periodic structures. Chapter 3 explains the methodology used in completing the research. The results of the simulations and its validation are shown in Chapter 4. Conclusions from this FEM research, including proposed areas for future study are stated in Chapter 5. Appendix A includes all the field plots from the geometries of interest. They include contour and surface plots. In Appendix B, the modifications to the codes formulated by Pelosi, et al. [12] are included, as well as the mesh construction file of the structure used to test the hypothesis in this thesis.

II. Summary of Current Knowledge

2.1 Overview

The digital computer allows the computational electromagnetics (CEM) practitioner to add the Finite Element Method to his portfolio of numerical tools because of its greater potential in solving more complex, real-world engineering problems.

This chapter presents the summary of current knowledge leading to the finite element method formulation of the solution to the scattering of a semi-infinite periodic structure in two dimensions.

2.2 Literature Review

2.2.1 Infinite Periodic Structures.

The study of FSS or infinitely periodic structures begins by finding a method of reducing the entire array into one representative element or reference cell. Floquet's Theory provides the methodology. When a plane wave is incident on an infinitely periodic array, the induced fields at the elements in the array are also periodic. In other words, the amplitude of the fields generated by every cell in the array are identical to the reference cell except for a linear phase shift factor [11]. For an incident plane wave of the form

$$
\begin{aligned}
\mathbf{E}^i(\mathbf{R}) &= \hat{\mathbf{e}}_i E^i e^{(-j\beta \hat{\mathbf{s}} \cdot \mathbf{R})} \\
&= \hat{\mathbf{e}}_i E^i e^{-j\beta(s_x x + s_y y + s_z z)},
\end{aligned}
\tag{2.1}
$$

where: $\hat{\mathbf{e}}_i$ is the polarization vector

$\hat{\mathbf{s}}$ is the propagation vector,

the total electric field at a point on the qm^{th} cell (the cell in the qth row and m^{th} column of the array) can be expressed as a function of the field at the equivalent location on the reference cell at the origin as [11]

$$
\mathbf{E}(r_{qm}) = \mathbf{E}(r_{00}) e^{-j\beta(qD_x s_x + mD_z s_x)},
\tag{2.2}
$$
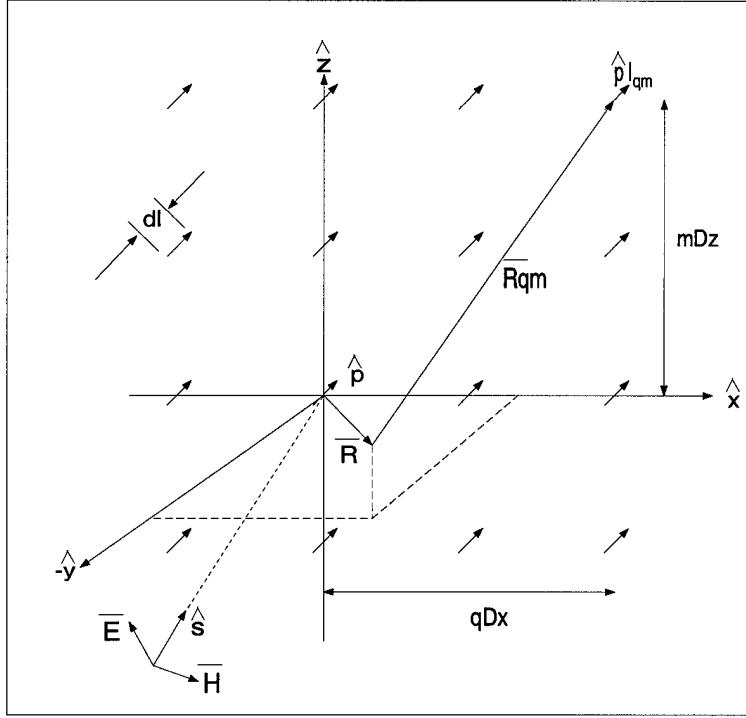
Figure 2.1   An Array of Hertzian Dipoles in Free Space [11].

or the magnetic field as

$$\mathbf{M}(r_{qm}) = \mathbf{M}(r_{00})e^{-j\beta(qD_x s_x + mD_z s_z)}, \tag{2.3}$$

where: D_x is the period in the $\hat{x}$ direction

D_z is the period in the $\hat{z}$ direction

β is the wave number.

For an infinite array of Hertzian dipoles (of differential length, dl) as shown in Figure 2.1, antenna theory gives us the magnetic vector potential at an arbitrary observation point a distance $\mathbf{R}$ from the dipole at the qth row and m^{th} column as [11]

$$d\mathbf{A}_{qm} = \hat{p}\frac{\mu I_{qm}dl}{4\pi}\frac{e^{-j\beta R_{qm}}}{R_{qm}}, \tag{2.4}$$

where $\hat{p}$ is the unit vector in the direction of the current elements. Note that the observation point could also be out of the plane where the dipoles are located.

Taking all the contributions from every element in the array, and relating the Floquet currents with respect to the current in the reference element gives

$$
\begin{aligned}
d\mathbf{A} &= \sum_{q=-\infty}^{\infty} \sum_{m=-\infty}^{\infty} \hat{p} \frac{\mu I_{qm} dl}{4\pi} \frac{e^{-j\beta R_{qm}}}{R_{qm}} \\
&= \sum_{q=-\infty}^{\infty} \sum_{m=-\infty}^{\infty} \hat{p} \frac{\mu (I e^{-j\beta q D_x s_x} e^{-j\beta m D_z s_z}) dl}{4\pi} \frac{e^{-j\beta R_{qm}}}{R_{qm}} \\
&= \sum_{q=-\infty}^{\infty} e^{-j\beta q D_x s_x} \left[\hat{p} \frac{\mu I dl}{4\pi} \sum_{m=-\infty}^{\infty} \frac{e^{-j\beta R_{qm}}}{R_{qm}} e^{-j\beta m D_z s_z} \right].
\end{aligned}
\tag{2.5}
$$

The electric field directly obtained from Equation (2.5) is a very slowly converging series. However, using the Poisson sum formula

$$
\sum_{m=-\infty}^{\infty} e^{jm\omega_o t} F(m\omega_o) = T \sum_{n=-\infty}^{\infty} f(t + nT),
\tag{2.6}
$$

and Fourier transforming the electric field to the spectral domain, Munk [11] derived the far-field electric field of an array of Hertzian dipoles in a lossless medium, with the reference element shifted a distance $\mathbf{R}'$ from the origin, as

$$
d\mathbf{E}(x,y,z) = \frac{\eta I dl}{2 D_x D_z} \sum_{k=-\infty}^{\infty} \sum_{n=-\infty}^{\infty} \frac{e^{-j\beta(\mathbf{R}-\mathbf{R}')\cdot\hat{\mathbf{r}}}}{r_y} [(\hat{r} \cdot \hat{p})\hat{r} - \hat{p}].
\tag{2.7}
$$

For finite length dipole elements, the electric field is

$$
\mathbf{E}(x,y,z) = \frac{\eta}{2 D_x D_z} \sum_{k=-\infty}^{\infty} \sum_{n=-\infty}^{\infty} \frac{e^{-j\beta\mathbf{R}\cdot\hat{\mathbf{r}}_\pm}}{r_y} [(\hat{r}_\pm \cdot \hat{p})\hat{r}_\pm - \hat{p}] \int_{Ref.Elem.} I_{00} e^{+j\beta\mathbf{R}'\cdot\hat{\mathbf{r}}} dl
\tag{2.8}
$$

where: $\hat{p}$ is the unit vector along the dipole's length

$[(\hat{r}_\pm \cdot \hat{p})\hat{r}_\pm - \hat{p}]$ is the polarization vector

$\hat{r}_\pm = \hat{x}(s_x + \frac{k\lambda}{D_x}) \pm \hat{y}r_y + \hat{z}(s_z + \frac{n\lambda}{D_z})$

$r_y = \sqrt{1 - (s_x + \frac{k\lambda}{D_x})^2 - (s_z + \frac{n\lambda}{D_z})^2}$ whose root is either positive real

   or negative imaginary

k, n are the new row and column indices in the spectral domain.

Having found the electric field radiated by the dipoles in the array, the mutual coupling (or impedance matrix) between them can be calculated. Since the excitation vector entries are known from the incident field, the system's response can be solved [9,18].

2.2.2 Semi-Infinite Periodic Structures. Semi-infinite periodic structures present a different problem. Although the available literature remains relatively sparse, several approaches have been published.

Wasylkiwskyj [22], in 1973, analyzed the mutual coupling effects in a semi-infinite array where he used the Weiner-Hoph factorization procedure to to solve an infinite order difference equation of the currents formulated at the antenna ports.

Cwik and Mittra [6] investigated curved and truncated strip arrays. Their technique requires two piecewise approximations. The first approximation assumes the induced currents in every element to be identical as if belonging to an infinite array. Then they replaced the edge element currents with currents found from the solution of a very small finite array. Unfortunately, this method does not perform well when the angle of incidence is near grazing because it fails to take into account the increased significance of the coupling between the edge elements and the inner elements.

Collins' approach to the edge problem involves a modification to the Poisson Sum Formula used in the analysis of infinite periodic arrays. The one-sided Poisson Sum Formula that he developed specifically for semi-infinite periodic arrays is derived by defining $F(m\omega_o)$ in Equation (2.6)

> ...to be the product of an infinite domain continuous function $G(\omega_o)$ and the Heaviside unit step function shifted by $\frac{\omega_o}{2}$ to capture the entire $m = 0$ term [5].

Following an inverse Fourier transformation, the one-sided Poisson Sum Formula can be expressed as

$$\sum_{q=0}^{\infty} e^{jq\omega_o t} G(q\omega_o) = T \sum_{k=-\infty}^{\infty} \left\{ \frac{g(t \pm kT)}{2} + \frac{j}{2\pi} \int_{-\infty}^{\infty} \frac{g(\tau)e^{-j\frac{\omega_o}{2}(t \pm kT - \tau)}}{t \pm kT - \tau} \right\} d\tau. \qquad (2.9)$$
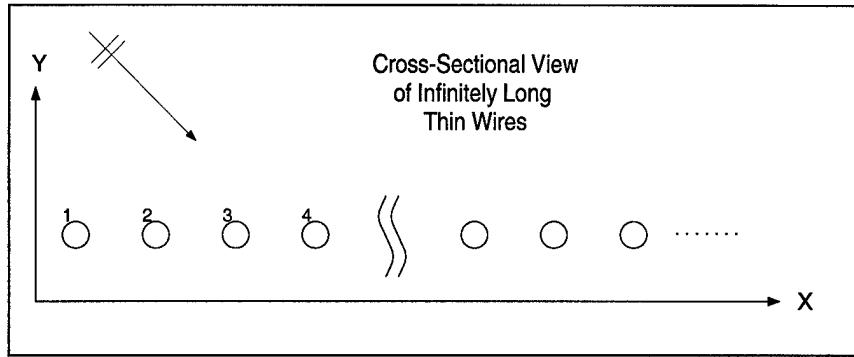
Figure 2.2   A Semi-Infinite Array of Long Thin Wires in Free Space

Note that the second term in the right hand side is a principal value integral and can be evaluated using residue calculus.

In the two dimensional case where the test geometry was an array of infinitely long thin wires which are periodically spaced extending all the way to infinity (see Figure 2.2), Collins showed that there will be some distance amplitudes will be approximately Over this section, the array where Munk's periodic characteristics. to the edge

An analog in the Finite Element Methods to the technique just described is what motivated this research.

2.2.3   The Finite Element Method Model of a Periodic Structure.   Like all numerical computation algorithms, the finite element method requires a problem domain that is finite. For the FEM however, this requirement is due to the physical discretization of the domain. In order to fully enclose a structure that is infinitely long but periodic, Floquet analysis is utilized. Floquet theory serves as the tool for collapsing an entire array into a representative cell, similar to the one previously described in the method of moments.

Implementation of the FEM on periodic structures has already been accomplished by others. Gedney, et al. [8] characterized periodic gratings, while McGrath [10] applied the FEM to phased array antennas.

Referring to Figure 2.3, a unit cell representing a periodic element of an infinite array is enclosed by an imaginary rectangular boundary, $\partial\Omega$. The top and bottom boundaries, $\partial\Omega_U$ and $\partial\Omega_D$, represent radiation boundaries. The two side walls, $\partial\Omega_L$ and $\partial\Omega_R$, represent

UNIT CELL

$\partial\Omega_U$

ε_o, μ_o

$\partial\Omega_L$

Periodic
Element

$\partial\Omega_R$

$\partial\Omega_D$
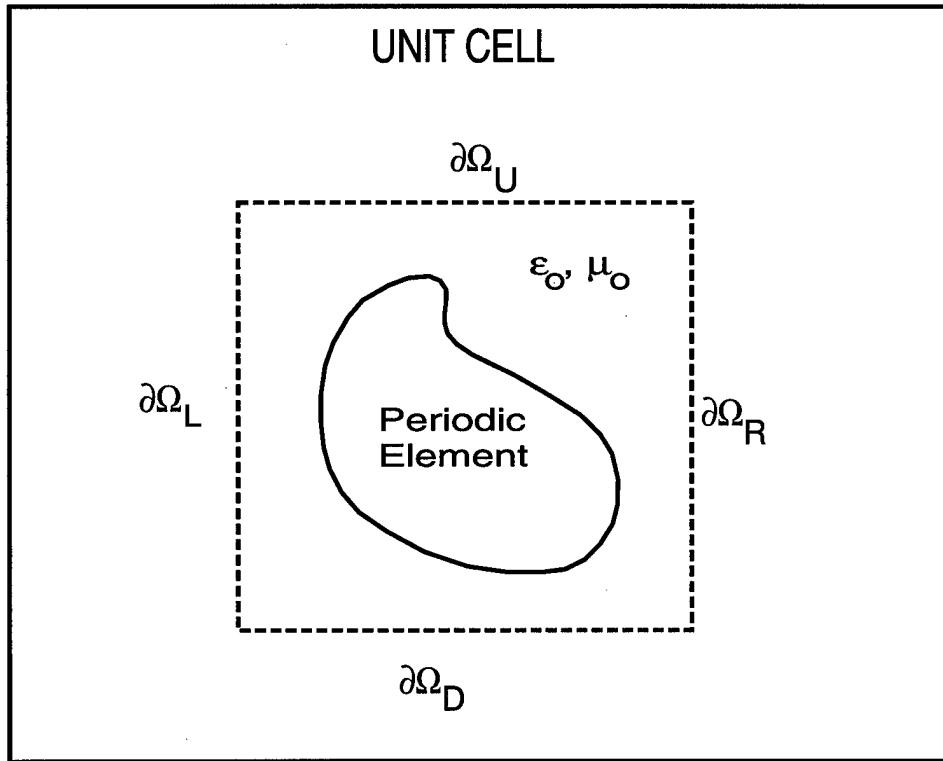
Figure 2.3   Representation of a Periodic Element for FEM Implementation

periodic boundaries. In order to account for the interaction between cells, McGrath compares the periodic boundary to "open-circuit" waveguide side walls [10]. The mesh elements in the computation region, however, must be symmetric. That is the left and right halves of the cell must be a mirror image of each other. This further implies that the nodes on the left boundary of the cell must have the same vertical coordinates as the nodes on the right boundary. In effect, the procedure amounts to a "wrapping around" of the left boundary into the right boundary, analogous to performing a circular convolution in digital signal processing.

The method used by McGrath combines the Finite Element Method with Floquet Modal Expansion. Hybrid methods, especially the ones in combination with integral methods like the MoM, essentially model the exact representation of the electromagnetic fields outside the domain of the problem. Like in the "pure" MoM [9], this makes a point on the FEM boundary, $\partial\Omega$, interact with all other points on the boundary. This *non-local* behavior essentially creates a dense coupling matrix, thereby requiring more computational resources.

The other type of FEM boundary problem implements an absorbing boundary enclosing the domain. With this method, test points (or nodes) in the the domain, Ω, interact only with *local* or neighboring points. This implementation produces a sparse coupling matrix, a big plus when computational efficiency is a big factor in solving a problem. This is one area where the FEM is superior to the MoM or other integral methods.

2.2.4   Software Implementation for a Two-Dimensional, Semi-Infinite Periodic Structure.   McGrath developed a three-dimensional finite element code called Phased Array Antenna Analysis (PARANA) to solve infinite periodic structures as phased array antenna geometries. This code is very versatile and can handle different types of problems such as two-port waveguide devices, array radiation, reflection and transmission from infinitely periodic structures, and array scattering. However, downgrading PARANA in order to handle a two-dimensional case would be counter-productive.

Pelosi, et al., in their book [12], released a finite element code specifically for two-dimensional problems. Therefore, it is the belief of this author that it would be simpler to modify this code to present a proof-of-concept problem involving two-dimensional, semi-infinite periodic geometries.

2.3   Development Approach

Figure 2.4 illustrates the geometry of interest in this research. It involves a semi-infinite periodic geometry in two-dimensional space. The problem domain consists of cylinders enclosed in Perfectly Matched Anisotropic (PMA) absorbing layers.

The analysis of a semi-infinite periodic structure begins by considering Collins' implementation of a physical basis function. The FEM model consists of an edge element or cell followed by a finite number of similar cells extending to the right of the edge element. The finite number of cells, together with enclosing the geometry with PMA absorbing layers, takes care of the problem of having an infinite calculation domain or an infinite number of unknowns.
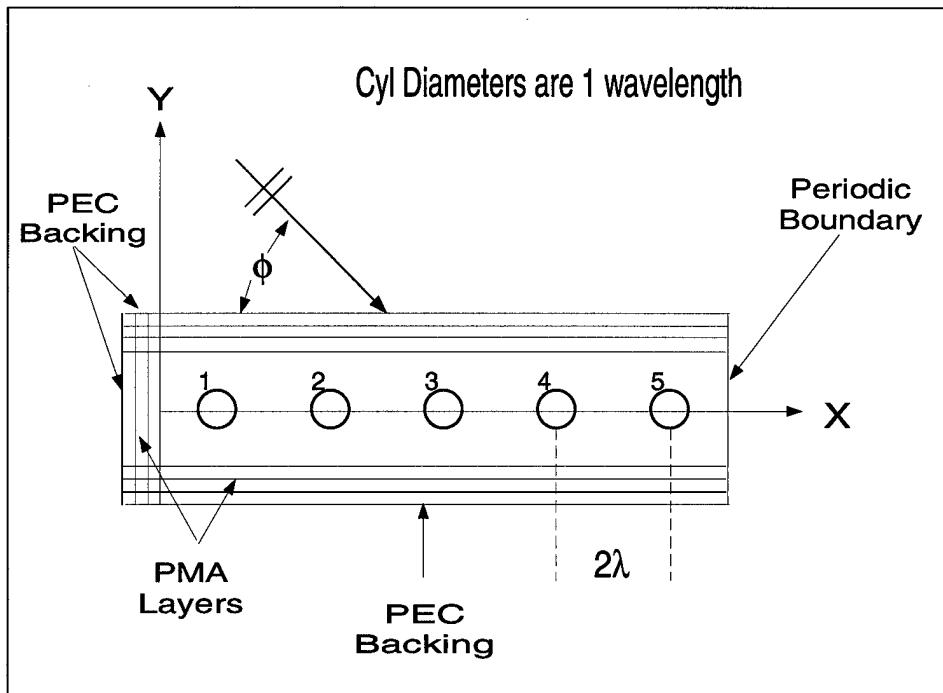
Figure 2.4   Five-Cylinder Periodic Array Enclosed in PMA and a Periodic Boundary

To take into account the fact that the structure actually extends indefinitely to the right, a boundary there must be one that simulates a infinitely extending periodic boundary. McGrath provides a hint as to how to characterize this boundary. The "open-circuit" boundary method previously described provides the means for taking into account the other cylinders to the right of the boundary. However, instead of folding it over onto the left-hand side boundary of a periodic cell within the geometry, the wrapping-over occurs with a cell immediately to the right of the periodic boundary, a periodic cell not within the bounds of the problem domain, Ω. Periodicity at the boundary takes into consideration the contribution of more periodic scatterers outside the region Ω.

Using an absorbing boundary in the FEM formulation accounts for the fact that the enclosed region, Ω, as a whole, is not a periodic one although its cells are.

2.4   Summary

This chapter presents the chronological development leading to the solution of the semi-infinite array problem using the method of moments and some hybrids of the MoM.

This chapter also presents a parallel solution to the infinite array problem using the finite element method. The next chapter details the FEM approach to solving the semi-infinite array problem.

III. Methodology

3.1 Introduction

The solution of a boundary value problem using the Finite Element Method can be successfully implemented by stepping through a very structured procedure. After the definition of the boundary value problem, the solution can be solved in five steps [12,21], namely:

1. Discretize the problem domain into finite elements.

2. Apply the functional (Wave or Helmholtz equation) over each element in the region.

3. Apply the boundary conditions and collate the contribution from each finite element in the region to form a global or coupling matrix.

4. Solve the system of equations.

5. Process the data to extract the pertinent information and create a visual representation of the quantities of interest.

The first step, preprocessing, is to *mesh* the region where the solution is desired. This can be accomplished by using graphic design or Computer-Aided Design (CAD) software. This is a mandatory step for all numerical solutions. This step is where the coordinates of *nodes* or points in the region are passed on to the numerical algorithm.

The second, third and fourth steps belong to the finite element method algorithm. This is where the differential equation is mapped into a discrete system so that it can be numerically processed in a digital computer. In the second step, the integro-differential equation is discretized into a set of linear equations so that it can be converted into matrix format. It is also in this step where the integro-differential equation is enforced on every element of the grid.

The third step is required if a boundary condition must be explicitly enforced. For example, a Dirichlet boundary condition occurs when at the surface of a Perfect Electrical Conductor (PEC), the tangential electric fields are zero. This type of condition must be explicitly enforced in the algorithm. A Neumann boundary condition, on the other hand,

specifies the normal derivative at the boundary. For an incident plane wave with a transverse magnetic (TM) polarization, the normal derivative of the magnetic fields on the surface of a PEC are zero.

The fourth step is choosing a solving mechanism for the system. Galerkin's method is the preferred method in the finite element method. This mechanism converts a differential equation into a set of linear equations for numerical computation. It essentially comes down to solving a matrix equation of the form

$$[A][x] = [b]. \tag{3.1}$$

The matrix $[A]$ is the called the coupling matrix where its elements depend on the inter-relationships of the nodes in the grid. The vector $[x]$ is the set of unknown parameters, and the vector $[b]$ is a vector of forcing or excitation functions. Solvers then essentially invert the matrix $[A]$ and multiply it by $[b]$ to get the solution vector $[x]$.

The final step is the post-processing step where the solution vector is processed and presented in a visual format that is conducive to analysis.

3.2   Theoretical Background

Throughout this document, the fields indicated herein are assumed to be time-harmonic with an $e^{j\omega t}$ dependence which is suppressed. Also, the analysis assumes a transverse magnetic TM_z polarized incident plane wave illumination so that the electric fields are the unknown quantities. If the magnetic field equations are desired, the duality principle can be used on the equations presented here.

In two-dimensional space, where a cylindrical scatterer is illuminated by a plane wave of transverse magnetic (TM) polarization as illustrated in Figure 3.1, the fields in the scatterer's vicinity can be obtained by the two-dimensional wave equation

$$\nabla_t \cdot \left(\frac{1}{\mu_r} \nabla_t E_z(x,y) \right) + k_o^2 \epsilon_r E_z(x,y) = f(x,y), \tag{3.2}$$
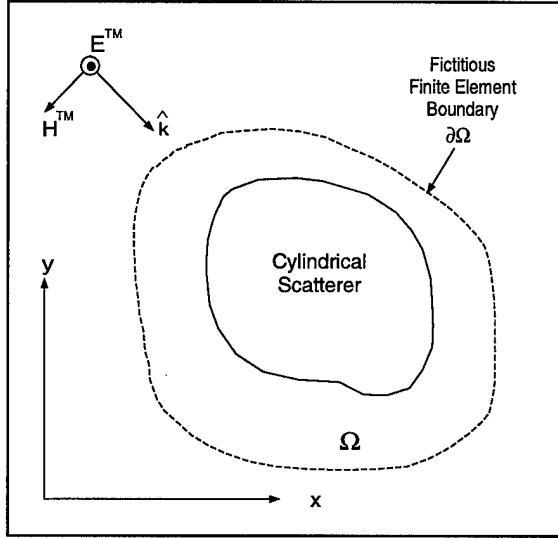
Figure 3.1   Two-Dimensional Scattering Configuration for Cylindrical Scatterers

where: $\nabla_t = \hat{\mathbf{x}}\frac{\partial}{\partial x} + \hat{\mathbf{y}}\frac{\partial}{\partial y}$,

k_o is the free space wave number,

ϵ_r is the relative permittivity of the medium,

μ_r is the relative permeability of the medium, and

$f(x,y)$ is the forcing function or external excitation.

Equation (3.2) is considered as a *strong* form of the wave equation because the differential operating on the unknown is second order. In order to apply the finite element method to Equation (3.2), the order of the differential operator must be reduced to one. This results in the *weak* form of the wave equation.

If we let a function $\tilde{E}_z$ approximate the unknown function E_z, the equality in Equation (3.2) no longer holds but instead results in a non-zero *residual*,

$$r(x,y) = \nabla_t \cdot \left(\frac{1}{\mu_r}\nabla_t \tilde{E}_z(x,y) \right) + k_o^2 \epsilon_r \tilde{E}_z(x,y) - f(x,y). \qquad (3.3)$$

The ideal value for $\tilde{E}_z$ is one that reduces the residual to zero over the entire domain, Ω. However, that is usually not numerically achievable all over the points in the domain. Instead it is more practical (and can be more easily implemented) to find an approximation $\tilde{E}_z$ that would reduce the residual to a minimum value at all points in Ω. The minimization process

can be done by weighting the residual over M subdomians. Geometrically, the residue must have no projections onto each of the M weighting functions. Mathematically, taking the inner product of the weighting functions with the residue gives the best approximation to the solution. Thus,

$$\int\int_\Omega W(x,y)r(x,y)d\Omega = 0. \tag{3.4}$$

Substituting Equation (3.3) into Equation (3.4) and dropping the functional notation of dependency in x and y, the wave equation becomes

$$\int\int_\Omega \left[W\nabla_t \cdot \left(\frac{1}{\mu_r}\nabla_t\tilde{E}_z \right) + Wk_o^2\epsilon_r\tilde{E}_z - Wf \right] ds = 0. \tag{3.5}$$

It is usually the case in Galerkin's method that the weighting functions and the basis functions are the same.

Applying the vector identity (Green's theorem or integration by parts),

$$\nabla \cdot (q\mathbf{A}) = q\nabla \cdot \mathbf{A} + \nabla q \cdot \mathbf{A}, \tag{3.6}$$

on the first term on the left-hand side of Equation (3.5) results in

$$W\nabla_t \cdot \frac{1}{\mu_r}\nabla_t\tilde{E}_z = \nabla_t \cdot \left(\frac{1}{\mu_r}W\nabla_t\tilde{E}_z \right) - \frac{1}{\mu_r}\nabla_t W \cdot \nabla_t\tilde{E}_z. \tag{3.7}$$

Substituting Equation (3.7) into Equation (3.5) results in

$$\int\int_\Omega \left[\nabla_t \cdot \left(\frac{1}{\mu_r}W\nabla_t\tilde{E}_z \right) - \frac{1}{\mu_r}\nabla_t W \cdot \nabla_t\tilde{E}_z + k_o^2\epsilon_r W\tilde{E}_z - W \right] ds = 0. \tag{3.8}$$

Application of the Divergence Theorem,

$$\int\int_\Omega \nabla_t \cdot \left(\frac{1}{\mu_r}W\nabla_t\tilde{E}_z \right) ds = \oint_{\partial\Omega} \frac{1}{\mu_r}W(\nabla_t\tilde{E}_z \cdot \hat{n})dl, \tag{3.9}$$

on the first term of the left-hand side of Equation (3.8) results in the *weak* form the the wave equation.

$$\iint_\Omega \left[-\frac{1}{\mu_r} \nabla_t W \cdot \nabla_t \tilde{E}_z + k^2 \epsilon_r W \tilde{E}_z - W f \right] ds + \oint_{\partial\Omega} \frac{1}{\mu_r} W (\hat{n} \cdot \nabla_t \tilde{E}_z) dl = 0, \qquad (3.10)$$

where $\partial\Omega$ represents a closed contour enclosing the domain, and $\hat{n}$ is the outward pointing unit normal vector on the contour.

In free space and in the absence of excitation sources, the weak form of the wave equation reduces to the weak form of the Helmholtz equation

$$\iint_\Omega \left[-\frac{1}{\mu_r} \nabla W \cdot \nabla \tilde{E}_z + k^2 \epsilon_r W \tilde{E}_z \right] ds + \oint_{\partial\Omega} \frac{1}{\mu_r} W (\hat{n} \cdot \nabla \tilde{E}_z) dl = 0. \qquad (3.11)$$

3.2.1 Formulation of a Circular Absorbing Boundary. The finite element method, as its namesake implies, requires a geometric domain that is finite. However, that does not mean that the domain of the problem must also be finite [17]. This important distinction enables the FEM to solve problems with unbounded regions, such as scattering and radiation problems. Typically, propagation problems are solved by seeking the solution to the wave equation or the Helmholtz equation.

The physical interpretation of the solution to the wave equation or the Helmholtz equation is an outward traveling wave, where the fields asymptotically decay to zero at infinity. Applying the FEM to such problems already imposes difficulties in its implementation. The biggest hurdle is that the domain must be finite. The next hurdle is how can an infinite domain problem be simulated by a numerical algorithm that requires a finite solution domain and still capture the characteristics of an outwardly expanding solution.

In order to overcome both difficulties, an absorbing boundary condition (ABC) must be specified. Absorbing boundaries accomplish the task of absorbing all scattered energy from the enclosed scatterer (similar to a *black body*) and effectively preventing reflected energy back into the interior region or the solution domain. It also acts as a bounding surface for the mesh elements.
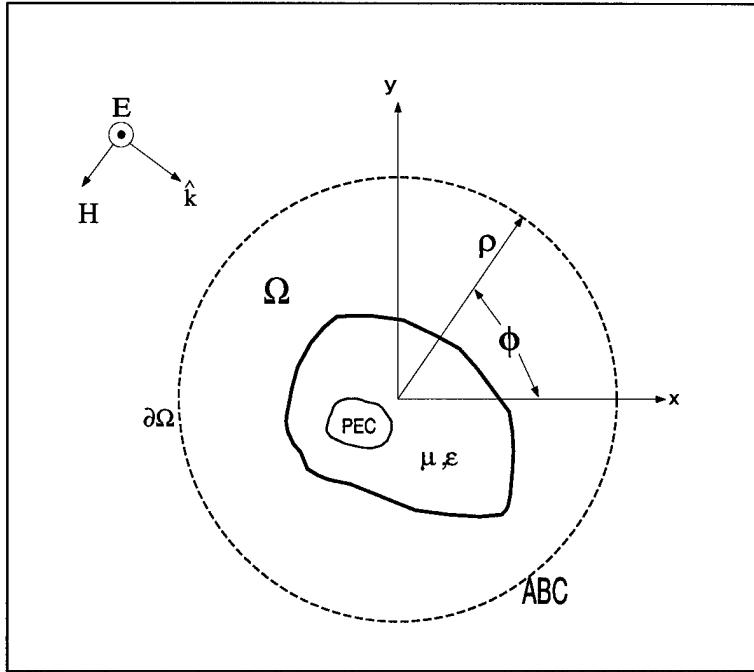
Figure 3.2   Cylindrical Scatterer Enclosed in a Fictitious Circular Absorbing Boundary

Generally, analytic absorbing boundaries represent the Green's integral at the boundary with an *a priori* approximation. For instance, Bayliss and Turkel applied the *a priori* knowledge of the Hankel function approximation for cylindrical wave propagation. In hybrid methods, however, the Green's integral on the boundary is numerically evaluated directly [17]. This distinction explains why absorbing boundary conditions preserve the sparsity of the *coupling* matrix. On the other hand, one important disadvantage of the absorbing boundary condition is that its accuracy drops off when the *a priori* approximation is no longer satisfied.

The development of absorbing boundaries in FEM is generally credited to Engquist and Majda(see [7]) who introduced the basic concepts using a planar boundary. Bayliss and Turkel [2] built on Engquist and Majda's ideas and proposed a circular absorbing boundary. Bayliss and Turkel developed a second order differential operator by starting from the assymptotic Hankel expansion approximation of an outward traveling electromagnetic field. Since the Hankel functions characterize cylindrical wave propagation, Bayliss and Turkel's model requires a circular absorbing boundary. Figure 3.2 illustrates such implementation.

Incorporating the second-order Bayliss and Turkel ABC model into the weak Helmholtz functional, Equation (3.11), and decomposing the total field into its scattered and incident field components results in (see [12,13,21] for derivation)

$$\int\int_{\Omega}\frac{1}{\mu_r}\nabla_t W \cdot \nabla_t E_z^s d\Omega - \int\int_{\Omega}k_o^2\epsilon_r W E_z^s d\Omega + \oint_{\partial\Omega}[W\alpha(\rho)E_z^s - \beta(\rho)\frac{\partial W}{\partial\phi}\frac{\partial E_z^s}{\partial\phi}]\rho d\phi$$

$$= -\int\int_{\Omega}\frac{1}{\mu_r}\nabla_t W \cdot \nabla_t E_z^i d\Omega + \int\int_{\Omega}k_o^2\epsilon_r W E_z^i d\Omega + \oint_{\partial\Omega}W\frac{\partial E_z^i}{\partial\rho}\rho d\phi, \quad (3.12)$$

where: $\alpha(\rho) = jk + \frac{1}{2\rho} - \frac{\beta(\rho)}{4\rho^2}$

$\beta(\rho) = \frac{1}{2(jk+\frac{1}{\rho})}$.

From this point on, the ∇ operator indicates two-dimensional differentiation and the unknown function E_z represents the approximating function introduced in the previous section without the *tilde* notation.

Discretizing Equation (3.12) above would result in a linear equation of the form shown previously in Equation (3.1). Note that the right hand side of Equation (3.12) is associated with the incident field, which from a scattering problem point of view is a known parameter.

3.2.2 *Formulation of a Perfectly Matched Anisotropic Absorbing Boundary.*

The circular absorbing boundary is a major development in the implementation of the FEM to electromagnetic scattering analysis. The only restriction in its application is that it must be strictly circular in shape. That could be a drawback when the scatterer being enclosed is elongated. For elongated scatterers, a circular boundary requires a larger radius, creating a larger area with nothing but free space. Although the coupling matrix remains sparse due to the "nearest neighbor" or local nature of the coupling between the nodes on the grid, its size would require computation on free space areas which are not of interest.

For problems regarding slender or elongated bodies, such as aircraft, a rectangular boundary is a logical geometry. A computational boundary analogous to that of absorbers used in anechoic chambers was formulated. Berenger [3] first proposed the idea of a rectangular enclosure for an absorbing boundary for use in the Finite Difference, Time-Domain
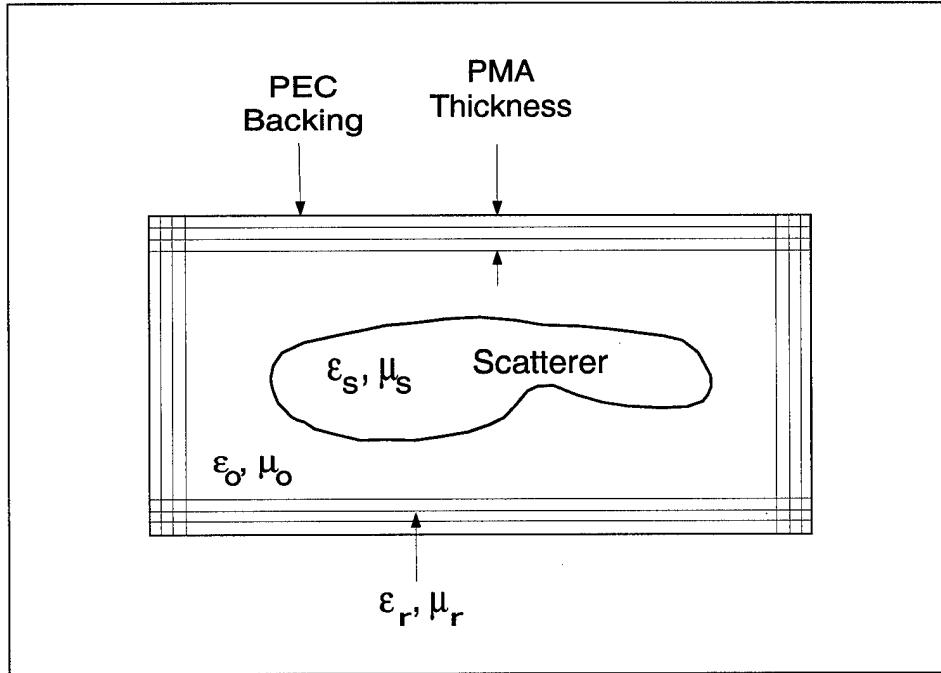
Figure 3.3   Cylindrical Scatterer Enclosed in a Fictitious PMA Boundary

(FDTD) numerical method. Berenger's technique, however, modifies Maxwell's equations to accommodate FDTD's time stepping routines. Sacks, et al. [15] then modified Berenger's formulation and used anisotropic materials in order to implement the formulation in FEM without the modifications to Maxwell's equations.

The idea is to enclose the scatterer with a rectangular boundary located in the near zone similar to the circular boundary (see Figure 3.3). The artificial absorbing materials used are anisotropic and usually implemented with layers of absorbers above a conducting surface, much like the absorber configurations in an anechoic chamber. A perfectly matched anisotropic (PMA) absorber features perfect absorption of any arbitrarily polarized plane wave of infinite frequency bandwidth and any angle of incidence. Although the interface between free space and the anisotropic material is reflectionless, the conducting surface which backs the finite set of PMA layers would certainly produce a reflection. However, careful selection of the layer thickness and ϵ and μ of the material reduces reflections back into the computational domain to the point where they don't perturb the solution significantly.

Starting from Equation (3.11), the fields in the interior region, Ω, can be decomposed into two subregions, the free space region and the PMA region. In the free space region the weak Helmholtz equation is

$$\int\!\!\int_{\Omega-\Omega_A} \frac{1}{\mu_r}\nabla W \cdot \nabla E_z d\Omega - \int\!\!\int_{\Omega-\Omega_A} k_o^2\epsilon_r W E_z^s d\Omega + \oint_{\partial(\Omega-\Omega_A)} W(\hat{n}\cdot\nabla E_z)dl = 0, \quad (3.13)$$

where: $\Omega - \Omega_A$ denotes the free space computational region

Ω_A is the computational region in the PMA absorber.

Similarly, the Helmholtz equation characterizing the fields in the PMA absorber region is

$$\int\!\!\int_{\Omega_A} \frac{1}{[\overline{\mu}]}\nabla W \cdot \nabla E_z d\Omega - \int\!\!\int_{\Omega_A} k_o^2[\overline{\epsilon}] W E_z^s d\Omega + \oint_{\partial\Omega_A} W(\hat{n}\cdot\nabla E_z)dl = 0, \quad (3.14)$$

where $[\overline{\mu}]$ and $[\overline{\epsilon}]$ are tensors characterizing the PMA and are of the form [15]

$$[\overline{\mu}] = \mu_o \begin{bmatrix} a & 0 & 0 \\ 0 & b & 0 \\ 0 & 0 & c \end{bmatrix} \quad (3.15)$$

and

$$[\overline{\epsilon}] = \epsilon_o \begin{bmatrix} a & 0 & 0 \\ 0 & b & 0 \\ 0 & 0 & c \end{bmatrix}. \quad (3.16)$$

The diagonal elements a, b, and c in the permittivity and permeability tensors are complex numbers. For perfect impedance matching between free space and the anisotropic medium

$$\frac{[\overline{\mu}]}{\mu_o} = \frac{[\overline{\epsilon}]}{\epsilon_o} = [\Lambda] = \begin{bmatrix} a & 0 & 0 \\ 0 & b & 0 \\ 0 & 0 & c \end{bmatrix}. \quad (3.17)$$

Referring to Figure (3.3), the contour integral in Equation (3.14) includes two boundaries, the PEC backing and the interface between free space and the PMA. The contour

integral at the PEC vanishes because of the tangential electric fields there are zero. The other part of the contour integral in Equation (3.14) is the same as the contour integral of Equation (3.13). However, since their surface normals are opposite in direction, they cancel out. Hence, Equation (3.13) becomes

$$\iint_{\Omega-\Omega_A} \frac{1}{\mu_r} \nabla W \cdot \nabla_t E_z^s d\Omega - \iint_{\Omega-\Omega_A} k_o^2 \epsilon_r W E_z^s d\Omega$$
$$= -\iint_{\Omega-\Omega_A} \frac{1}{\mu_r} \nabla_t W \cdot \nabla_t E_z^i d\Omega + \iint_{\Omega-\Omega_A} k_o^2 \epsilon_r W E_z^i d\Omega, \qquad (3.18)$$

after decomposing the total field into its scattered and incident components. Similarly, the field equation in the PMA region is

$$\iint_{\Omega_A} a \frac{\partial W}{\partial y} \frac{\partial E_z^s}{\partial y} d\Omega + \iint_{\Omega_A} b \frac{\partial W}{\partial x} \frac{\partial E_z^s}{\partial x} d\Omega - \iint_{\Omega_A} k_o^2 c W E_z^s d\Omega$$
$$= \iint_{\Omega_A} \nabla_t W \cdot \nabla_t E_z^i d\Omega + \iint_{\Omega_A} k_o^2 W E_z^i d\Omega, \qquad (3.19)$$

where a, b, and c are the diagonal elements of the complex permittivity and permeability tensors characterizing the PMA material. Note that the material parameters on the right hand side of Equation (3.19) are set to unity because the PMA exists only for the scattered field and not for the incident field.

3.3 Finite Element Grid Generation of the Problem

Discretizing or *meshing* the problem domain is usually done by Computer-Aided Drafting (CAD) packages. The software package that was utilized [12] was not sufficiently automated, nor was it enclosed in a graphical user interface (GUI). The problem domain is constructed with a set of non-overlapping quadrilateral *blocks*. A block is defined as a four-sided object in two-dimensional space whose sides can be characterized by second-order curves [12,16]. A side can be specified by a set of two end points and an intermediate point. As seen in Figure 3.4, a block can thus be defined with a total of eight points. The blocks are further subdivided into smaller triangular mesh elements in the mesh generator.
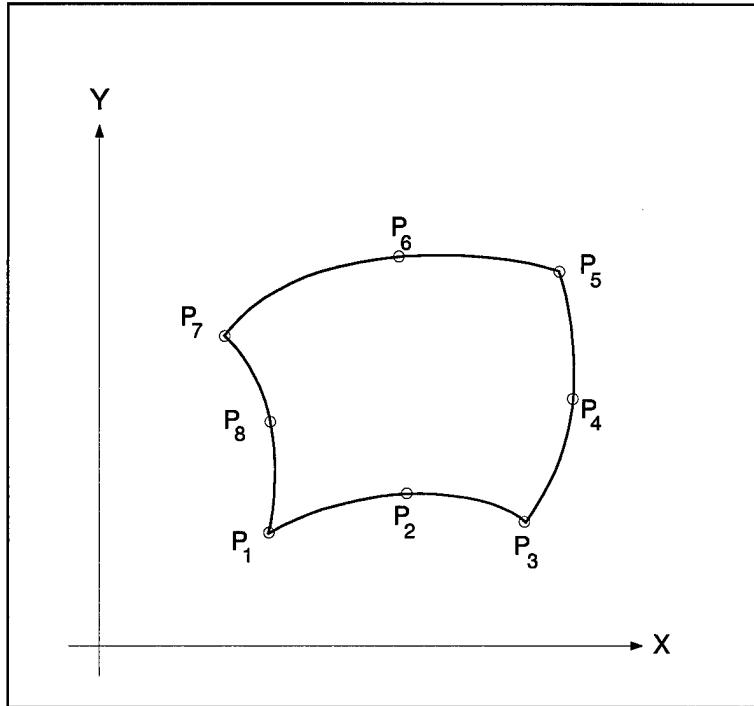
Figure 3.4   Generic Quadrilateral Block Description [12]

The geometry input file to the mesh generator requires three sections to fully define the domain of the problem. The first section describes the set of non-overlapping quadrilateral blocks, their node numbering sequence based on a global node numbering system for the whole geometry, and the material assignment of each block. Description of the block requires the sequential order of nodes around the block in a counterclockwise direction. The second section specifies the Cartesian coordinates of each node in the region. The last section describes how each particular block is to be subdivided into finer sections. The geometry input file used in this research is included in the Appendix B.

The output of the mesh generator is the file that the FEM code reads. This file consists of a header and four sections. The first section specifies the list of the mesh elements, either triangular or quadrilateral, the nodes that make up the element (three for first-order triangles and four for first-order quadrilaterals), and a flag indicating which material the mesh elements belong to. The second section specifies the nodes and their Cartesian coordinates again, as they may have been renumbered by the optimization routine (i.e. Delaunay regularization) in the mesh generator [12]. The third and fourth sections list the edges and edge labels

Geometry	Boundary Type	Cylinder Diameter	Incident Angles
5-Cylinder	Periodic	1λ	$0° - 90°$; $5°$ increments
	PMA	1λ	$0° - 90°$; $5°$ increments
15-Cylinder	PMA	1λ	$0° - 90°$; $5°$ increments

Table 3.1   Geometry Descriptions for the Analysis of a Semi-Infinite Periodic Structure

of each element in the grid. The third and fourth sections are particularly useful when using vector finite elements for computing three-dimensional scattering. However, since this research is confined to two-dimension scattering, edges and edge labels are not particularly used.

Table 3.1 shows the geometries of interest which consist of three sets, each made up of two-dimensional cylindrical scatterers. The first set is a semi-infinite periodic array of five cylinders shown in Figure 2.4. The solution domain is bounded by a rectangular enclosure consisting of Perfectly Matched Anisotropic (PMA) absorber layers on three sides and by a periodic boundary on one side. The PMA boundaries enclose the domain on the top and bottom sides and on the left side of the periodic structure. The periodic boundary is located on the right side of the structure. The cylinders are periodically spaced 2λ apart. There is also a five-cylinder finite array that is fully enclosed by a rectangular PMA boundary. Both geometries have cylinders that are 1λ in diameter.

The other geometry set is a finite array of fifteen cylinders, shown in Figure 3.5. The cylinders are also periodically spaced 2λ apart. The fifteen-cylinder array is fully enclosed by a rectangular box of PMA absorbing layers.

The fields that are scattered by the 5-cylinder and the 15-cylinder finite arrays are used for comparison with the fields scattered by the 5-cylinder periodic array. By comparing the fields in the vicinity of the edge cylinders with the fields in the vicinity of the cylinder next to the periodic boundary, a measure of the effectiveness of the implemented periodic boundary is obtained.

To mesh each one of the specified geometries, intermediate grid points are defined and the problem domain divided into blocks. Intermediate grid points are usually defined
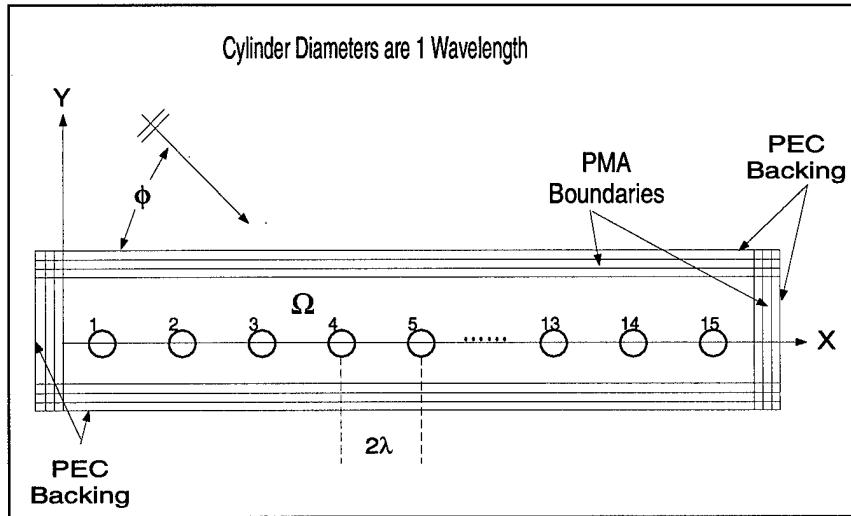
Figure 3.5   Geometry Description for 15-Cylinder Finite Array Fully Enclosed in a Rectangular PMA Boundary

on interfaces between two materials, like the interface between the PMA and the free space inside the problem domain, or on PEC boundaries. This graphical description of the problem domain is the required input to the mesh generator.

The grid or mesh generator can mesh the domain with elements that are either triangles or quadrilaterals. Triangles are usually preferred because they can readily approximate any complex shape. The degree of approximation can be adjusted by increasing or decreasing the number of triangles in the mesh. For example, to accurately render an arbitrarily complex shaped domain, smaller triangles, and therefore more of them, are required. More triangles mean more nodes (or vertices of the triangles) which translate to more unknowns required to compute the solution to the fields in the domain. Alternatively, a coarser approximation to the same domain requires fewer triangles, which translates to a smaller number of unknowns. The decision to increase or decrease the number of mesh elements depends on several factors. These are the computational resources available, the desired accuracy of the solution, and the time it takes to obtain the solution.

In the finite element method applied to electromagnetic field problems, a rule of thumb is to have the lengths of the sides of triangles about $\frac{\lambda}{10}$ [16,21]. For this research, the domain is meshed with triangle side lengths of $\frac{\lambda}{8}$. This decision is based on consideration of the
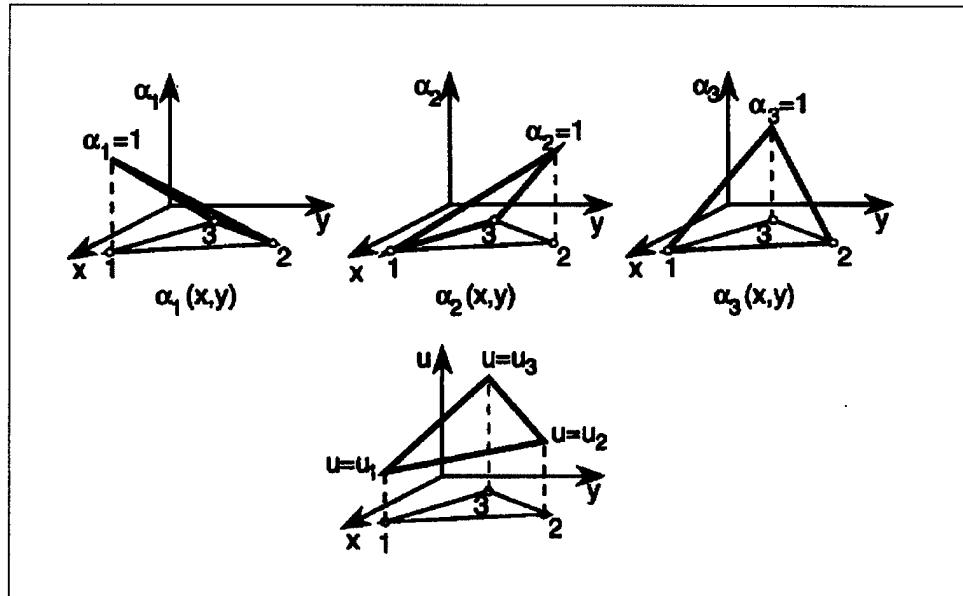
Figure 3.6   Shape Functions and Linear Approximations of Fields Inside a Triangular Mesh Element [12]

time it takes to mesh the problem domain, especially with the fifteen-cylinder finite periodic array. The other factor affecting the decision to use $\frac{\lambda}{8}$ is to minimize the number of nodes or unknowns in the problem domain.

3.4   Discretization of the Weak Form of the Wave Equation

Discretizing the weak Helmholtz or wave equations by representing them as a linear system of equations comes after meshing the problem domain. This can be done by approximating the fields inside each mesh element with a set of linear basis functions, also commonly known as *shape functions*. For first-order triangles, the approximating function is

$$\tilde{E}^{(e)} = \sum_{i=1}^{3} \alpha_i^{(e)} \tilde{E}_i^{(e)} \qquad (3.20)$$

where the $\alpha_i^{(e)}$'s are the basis functions or *shape functions* for each of the nodes of the eth element in the mesh (see Figure 3.6). The triangles used throughout this reseach are first order, meaning they have a total of three nodes. $\tilde{E}_i^{(e)}$ are the yet unknown coefficients of the basis functions and they represent the values of the fields at each node of the eth mesh element.

3-14

Shape functions approximate geometrical patterns with polynomial expressions. For triangular mesh elements, the basis or shape functions are usually expressed in what Silvester defines as *simplex coordinates*. Simplex coordinates transform shape functions defined in the Cartesian coordinate system to a coordinate system that is independent of position. This is important since the triangular elements that make up the grid do not, in general, have the same aspect ratios or are similarly collocated in space. For example, one triangle in the mesh may have a different orientation compared to another one in the mesh. The simplex coordinate transformation equations are [16]

$$
\begin{bmatrix} \alpha_1 \\ \alpha_2 \\ \alpha_3 \end{bmatrix} = \frac{1}{2A} \begin{bmatrix} (x_2 y_3 - x_3 y_2) & (y_2 - y_3) & (x_3 - x_2) \\ (x_3 y_1 - x_1 y_3) & (y_3 - y_1) & (x_1 - x_3) \\ (x_1 y_2 - x_2 y_1) & (y_1 - y_2) & (x_2 - x_1) \end{bmatrix} \begin{bmatrix} 1 \\ x \\ y \end{bmatrix}, \tag{3.21}
$$

where the area of the triangle is:

$$
A = \frac{1}{2}[(x_2 - x_1)(y_3 - y_1) - (x_3 - x_1)(y_2 - y_1)].
$$

Further, the shape functions have the following property

$$
\alpha_{i_{(x_j, y_j)}} = \begin{cases} 1 & \text{if } i = j \\ 0 & \text{if } i \neq j \end{cases}. \tag{3.22}
$$

The matrix formulation can be achieved by defining a weighting or testing function and taking its inner product with the basis functions. The most preferred method, Galerkin's method, requires the weighting function to be equal to the basis functions.

Note that the only reason for discretizing an integro-differential equation is to obtain N linearly independent algebraic equations so that it can be implemented numerically [14]. Galerkin's method of applying weighting functions to the differential equation, and making it equal to the basis function exactly does that process.

Discretizing the Helmholtz equations in the the PMA-enclosed free space and inside the PMA material is implemented simply by substituting the approximating functions of Equation (3.20) into Equations (3.18) and (3.19). Doing so results in

$$\frac{1}{\mu_r}[S_x^{(e)}][E^{s(e)}] + \frac{1}{\mu_r}[S_y^{(e)}][E^{s(e)}] - k_o^2\epsilon_r[T^{(e)}][E^{s(e)}] = [B_{FreeSpace}^{(e)}] \qquad (3.23)$$

in the free space portion of the computational region and

$$a[S_x^{(e)}][E^{s(e)}] + b[S_y^{(e)}][E^{s(e)}] - k_o^2 c[T^{(e)}][E^{s(e)}] = [B_{PMA}^{(e)}] \qquad (3.24)$$

inside the PMA material. The right hand side of both Equations (3.23) and (3.24) above are associated with the incident fields so that they are usually known quantities. The coefficient matrices are

$$[S_x^{(e)}] = \int\int_{\Delta^{(e)}} \frac{\partial \alpha_i^{(e)}}{\partial x} \frac{\partial \alpha_j^{(e)}}{\partial x} dS \qquad (3.25)$$

$$[S_y^{(e)}] = \int\int_{\Delta^{(e)}} \frac{\partial \alpha_i^{(e)}}{\partial y} \frac{\partial \alpha_j^{(e)}}{\partial y} dS \qquad (3.26)$$

$$[T^{(e)}] = \int\int_{\Delta^{(e)}} \alpha_i^{(e)} \alpha_j^{(e)} dS. \qquad (3.27)$$

The fields in each element of the mesh are calculated individually. Generally, interactions or coupling between nodes occur only between immediate neighbors. If a hybrid method is utilized, however, coupling may occur between nodes other than its immediate neighbor. Thus, when assembling the coupling or global matrix, the field value of a node from a triangle is summed up only with field values from neighboring nodes, resulting in a sparse matrix. The neighboring nodes may either belong to adjacent triangles or from the same triangle.

Part of the assembly process for the coupling matrix is the incorporation of any boundary conditions. A Dirichlet boundary condition exists in a problem domain when field values are prescribed for nodes on the boundary. For instance $E_z = f(t)$, where $f(t) = 0$ on the surface of a PEC for transverse magnetic (TM) polarization. Another type of boundary
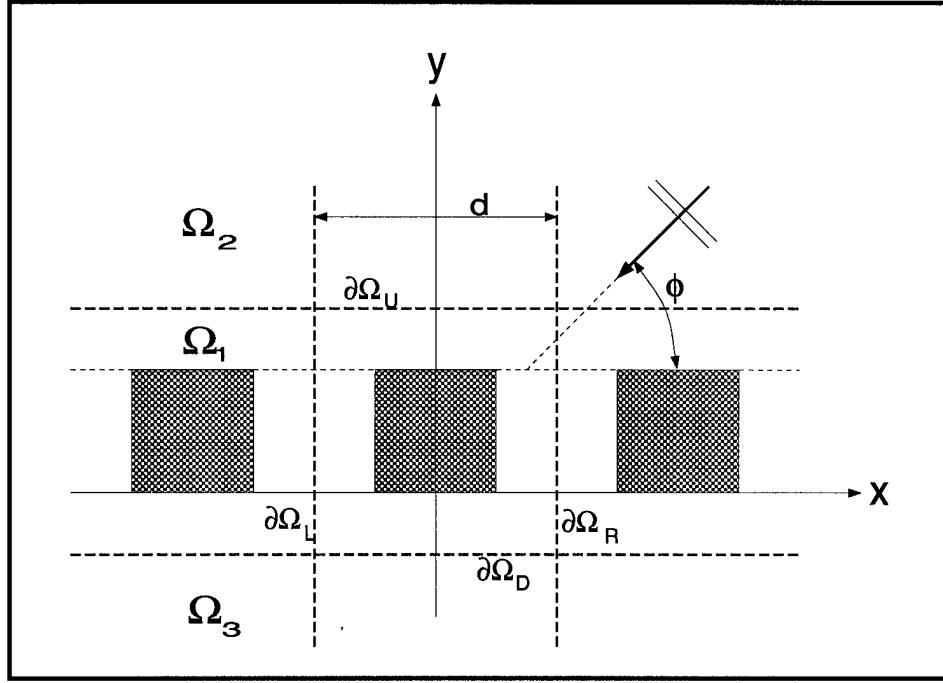
Figure 3.7   Two-Dimensional Periodic Structure [12].

condition is the Neumann boundary condition where $\frac{\partial H_z}{\partial n} = g(t)$. For Transverse Electric (TE) polarization, the magnetic field on the surface of a PEC vanishes so that $\frac{\partial H_z}{\partial n} = 0$.

3.5 Implementation of the Periodic Boundary

The main objective of this research is to find a way to mimic the fields generated by a semi-infinite periodic structure illuminated by a plane wave in free space with a substitute geometry that is finite. The technique proposed is by hybridizing the FEM with a Floquet modal expansion. Briefly, Floquet analysis takes advantage of the periodicity in an array and designates a periodic element or unit cell in an array to represent the entire array.

For a two-dimensional, infinitely periodic structure (one that is uniform in one direction and periodic in the other) as shown in Figure 3.7, the total fields induced by an incident TM_z-polarized plane wave on the array can be expressed as [12]

$$E_z^t(x + d, y) = E_z^t(x, y)e^{jkd\cos(\phi_i)}, \tag{3.28}$$

where d is the spatial period, k is the propagation constant in the medium, and ϕ_i is the incident angle.

Equation (3.28) says that the amplitudes of the fields in a periodic structure are essentially the same as that of some reference cell located at an arbitrary reference frame (say the origin in Cartesian coordinates) except for a phase factor.

For the periodic structure in Figure 3.7, Equation (3.11) applies to the region inside the fictitious boundary. The contour integral for a rectangular enclosure comprises four segments, $\partial\Omega_U$, $\partial\Omega_L$, $\partial\Omega_D$, and $\partial\Omega_L$. The weak Helmholtz equation inside the region is [10, 12]

$$\iint_\Omega \left[-\frac{1}{\mu_r}\nabla W \cdot \nabla E_z + k^2 \epsilon_r W E_z \right] ds + \int_{\partial\Omega_U} \frac{1}{\mu_r} W(\hat{n} \cdot \nabla E_z) dl$$
$$+ \int_{\partial\Omega_D} \frac{1}{\mu_r} W(\hat{n} \cdot \nabla E_z) dl + \int_{\partial\Omega_L} \frac{1}{\mu_r} W(\hat{n} \cdot \nabla E_z) dl$$
$$+ \int_{\partial\Omega_R} \frac{1}{\mu_r} W(\hat{n} \cdot \nabla E_z) dl = 0. \tag{3.29}$$

The top boundary, $\partial\Omega_U$, and the bottom boundary, $\partial\Gamma_D$, enforce the continuity of the tangential fields between the bounded region and free space above and below the structure, respectively. These are sometimes referred to as Floquet Harmonics [10]. The left boundary, $\partial\Omega_L$, and right boundary, $\partial\Omega_R$, enforce the periodic boundary and are related to each other by a Floquet phase factor.

$$\int_{\partial\Omega_R} \frac{1}{\mu_r} W(\hat{n} \cdot \nabla E_z) dy = \int_{\partial\Omega_L} \frac{1}{\mu_r} W(\hat{n} \cdot \nabla E_z) e^{jkd\cos(\phi_i)} dy. \tag{3.30}$$

In order to easily impose the periodic boundary conditions as described previously, there must be a one-to-one correspondence of nodes on each side of the periodic boundaries. For the 2-D geometry shown in Figure 3.7, this essentially means that each node on the right boundary must have the same y-coordinates as a corresponding node on the left boundary [10, 12]. This procedure is viewed as what McGrath calls "folding over the boundaries onto each other [10]."

A semi-infinite periodic structure can be similarly implemented. The top and bottom boundaries are terminated by PEC-backed PMA layers. The side boundary where the edge is

located is also terminated with PEC-backed PMA layers. On the right boundary, however, a periodic boundary is implemented. This is a necessary condition to account for the cylinders extending forever to the right.

As can be seen in Figure 2.4, the folding over of the right boundary onto the left boundary can not be accomplished on this particular domain because the array elements are not representative of a "unit cell" described in the infinite periodic array formulation. Periodicity at the right boundary was initially thought to be implemented by multiplying the amplitudes of the fields there by the Floquet phase factor, $e^{jkd \cos(\phi_i)}$.
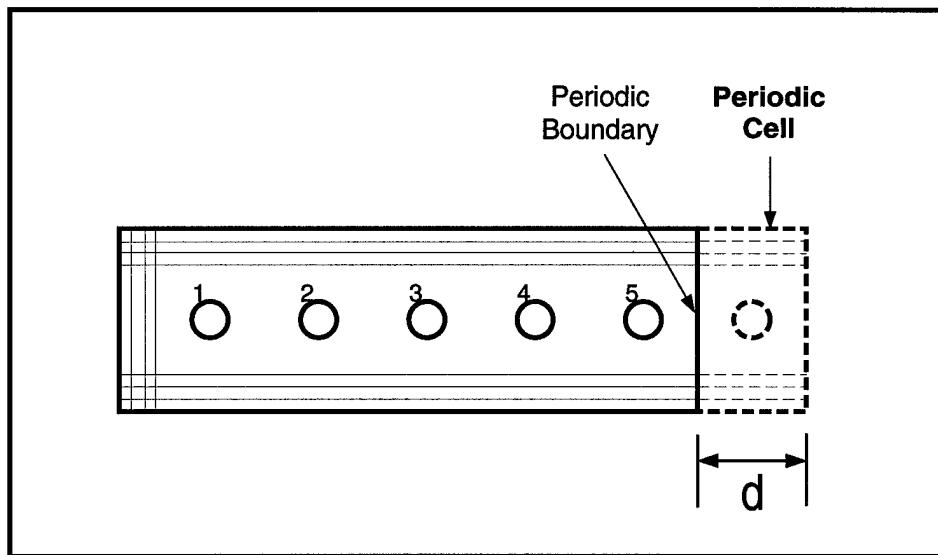

Figure 3.8   Implementation of a Single Periodic Boundary

This is equivalent to attaching a fictitious unit cell of period d, similar to the one previously described in the infinite array case, adjacent to the right boundary of the semi-infinite structure. Figure 3.8 illustrates the boundary implementation. The left boundary of the fictitious unit cell is related to its right boundary by Equation (3.28). To enforce the continuity of the fields across this boundary, the left hand boundary of the fictitious unit cell is made equal to the right boundary of the semi-infinite geometry. The right periodic boundary is then implemented in Equations (3.18) and (3.19) where they become

$$\iint_{\Omega-\Omega_A} \frac{1}{\mu_r} \nabla_t W \cdot \nabla_t E_z^s d\Omega - \iint_{\Omega-\Omega_A} k_o^2 \epsilon_r W E_z^s d\Omega + \int_{\partial\Omega_R} \frac{1}{\mu_r} W(\hat{n} \cdot \nabla E_z^s)e^{jkd\cos(\phi_i)}dy$$

$$= -\iint_{\Omega-\Omega_A} \frac{1}{\mu_r} \nabla_t W \cdot \nabla_t E_z^i d\Omega + \iint_{\Omega-\Omega_A} k_o^2 \epsilon_r W E_z^i d\Omega$$

$$+ \int_{\partial\Omega_R} \frac{1}{\mu_r} W(\hat{n} \cdot \nabla E_z^i)e^{jkd\cos(\phi_i)}dy \quad (3.31)$$

and

$$\iint_{\Omega_A} a\frac{\partial W}{\partial y}\frac{\partial E_z^s}{\partial y}d\Omega + \iint_{\Omega_A} b\frac{\partial W}{\partial x}\frac{\partial E_z^s}{\partial x}d\Omega - \iint_{\Omega_A} k_o^2 c W E_z^s d\Omega$$

$$+ \int_{\partial\Omega_R} \frac{1}{\mu_r} W(\hat{n} \cdot \nabla E_z^s)e^{jkd\cos(\phi_i)}dy$$

$$= \iint_{\Omega_A} \nabla_t W \cdot \nabla_t E_z^i d\Omega + \iint_{\Omega_A} k_o^2 W E_z^i d\Omega$$

$$+ \int_{\partial\Omega_R} \frac{1}{\mu_r} W(\hat{n} \cdot \nabla E_z^i)e^{jkd\cos(\phi_i)}dy. \quad (3.32)$$

It is important to note that the periodic boundary conditions in Equations (3.31) and (3.32) only apply to the boundary and not to the entire interior region in the domain, Ω. The discretization of Equation (3.31) and Equation (3.32) can be converted into matrix format by using Galerkin's method previously discussed.

3.6 The Finite Element Solution

Using Galerkin's method, Equations (3.31) and (3.32) can be discretized. The resulting equations are similar to Equations (3.23) and (3.24),

$$\left\{ \frac{1}{\mu_r}[S_x^{(e)}][E^{s(e)}] + \frac{1}{\mu_r}[S_y^{(e)}][E^{s(e)}] - k_o^2\epsilon_r[T^{(e)}][E^{s(e)}] \right\}\bigg|_{e^{jkd\cos(\phi_i)}} = [B_{FreeSpace}^{(e)}]\bigg|_{e^{jkd\cos(\phi_i)}}$$

$$(3.33)$$

and

$$\left\{ a[S_x^{(e)}][E^{s(e)}] + b[S_y^{(e)}][E^{s(e)}] - k_o^2 c[T^{(e)}][E^{s(e)}] \right\}\bigg|_{e^{jkd\cos(\phi_i)}} = [B_{PMA}^{(e)}]\bigg|_{e^{jkd\cos(\phi_i)}}. \quad (3.34)$$
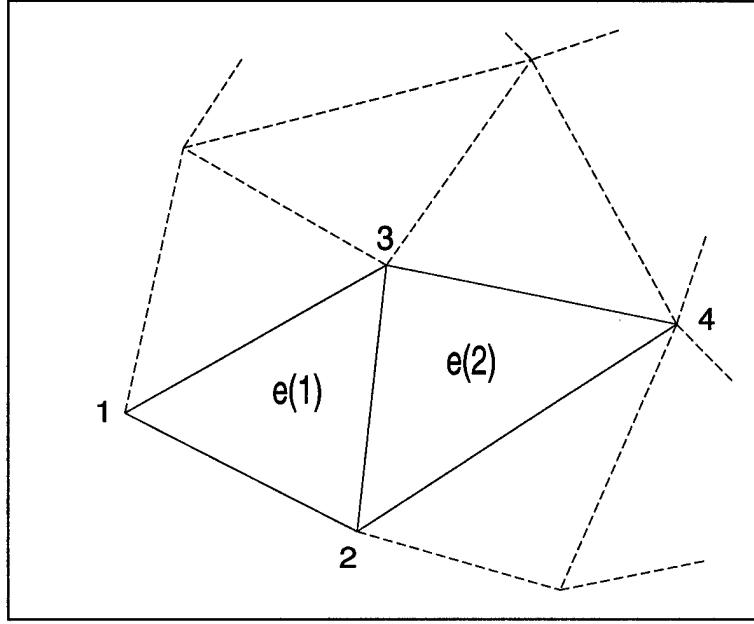
Figure 3.9   Node Interactions in an Element Matrix

The difference is when the node being considered is on the periodic boundary. The elements of matrices $[S_x^{(e)}]$, $[S_y^{(e)}]$, and $[T^{(e)}]$ that interact with the boundary node will be multiplied by the phase factor $e^{jkd\cos(\phi_i)}$. For example, in Figure 3.9, if node 1 in the first element belongs to the periodic boundary, then the element matrix $[S^{(e=1)}]$ is

$$[S^{(e=1)}] = \begin{bmatrix} e^{jkd\cos(\phi_i)}S_{11} & e^{jkd\cos(\phi_i)}S_{12} & e^{jkd\cos(\phi_i)}S_{13} \\ e^{jkd\cos(\phi_i)}S_{21} & S_{22} & S_{23} \\ e^{jkd\cos(\phi_i)}S_{31} & S_{32} & S_{33} \end{bmatrix}. \qquad (3.35)$$

The matrices $[T^{(e)}]$ and $[B^{(e)}]$ are implemented similarly to the procedure shown for $[S^{(e)}]$ above.

All the processes described in the previous section are incorporated in one subroutine in the code provided by Pelosi, et al. [12]. The rest of the code remained unmodified. Based on the flowchart shown in Figure 3.10, the modified subroutine only involves the branch where the absorbing boundary is made up of PMA layers. The flowchart for the modified subroutine for implementing the single periodic boundary is shown in Figure 3.11. Code

modification allowing for the incorporation of a semi-infinite periodic structure using the analytic ABC (circular boundary) is not implemented.

The FEM software utilizes subroutines from the freely available mathematical libraries of the Linear Algebra Package (LAPACK) program [1]. The LAPACK subroutines are mainly used for solving the linear equation shown in Equation (3.1) to obtain the fields in the solution domain.

3.7 Post-processing and Data Visualization

The output of the FEM consists of the value of quantities that are of interest in each node specified on the grid. In this research, the quantity of interest is the electric field since we were interested in the Transverse Magnetic (TM), or E-polarization scattering from a two-dimensional body. However, the mesh grid is usually not uniformly spaced. In order for graphical interfaces to display a coherent plot, the data points must be uniformly spaced. Thus, a graphical post-processor performs the function of interpolating between the data obtained in the FEM solution and extracting uniformly incremented data points. The post-processor provided in the software package is utilized without any modifications to the code other than changing the parameters to accommodate more nodes and mesh elements.

A Matlab code is written to take advantage of its powerful graphical environment. The output of the post-processor is converted to Matlab format to produce the contour map and the 3-dimensional surface plot of the fields. The Matlab code is shown in Appendix B.3.

3.8 Summary

This chapter shows the formulation used to modify the FEM solution for regions enclosed by PMA absorber layers to include semi-infinite periodic structures. The modifications involve removal of a PMA boundary on the opposite side of the edge where the semi-infinite structure is "cut" and substituting a periodic boundary in its place. The periodic boundary is formulated from the hypothesis that the periodic fields are produced from a spatially periodic structure. The next chapter shows the results of the formulations described in this chapter.
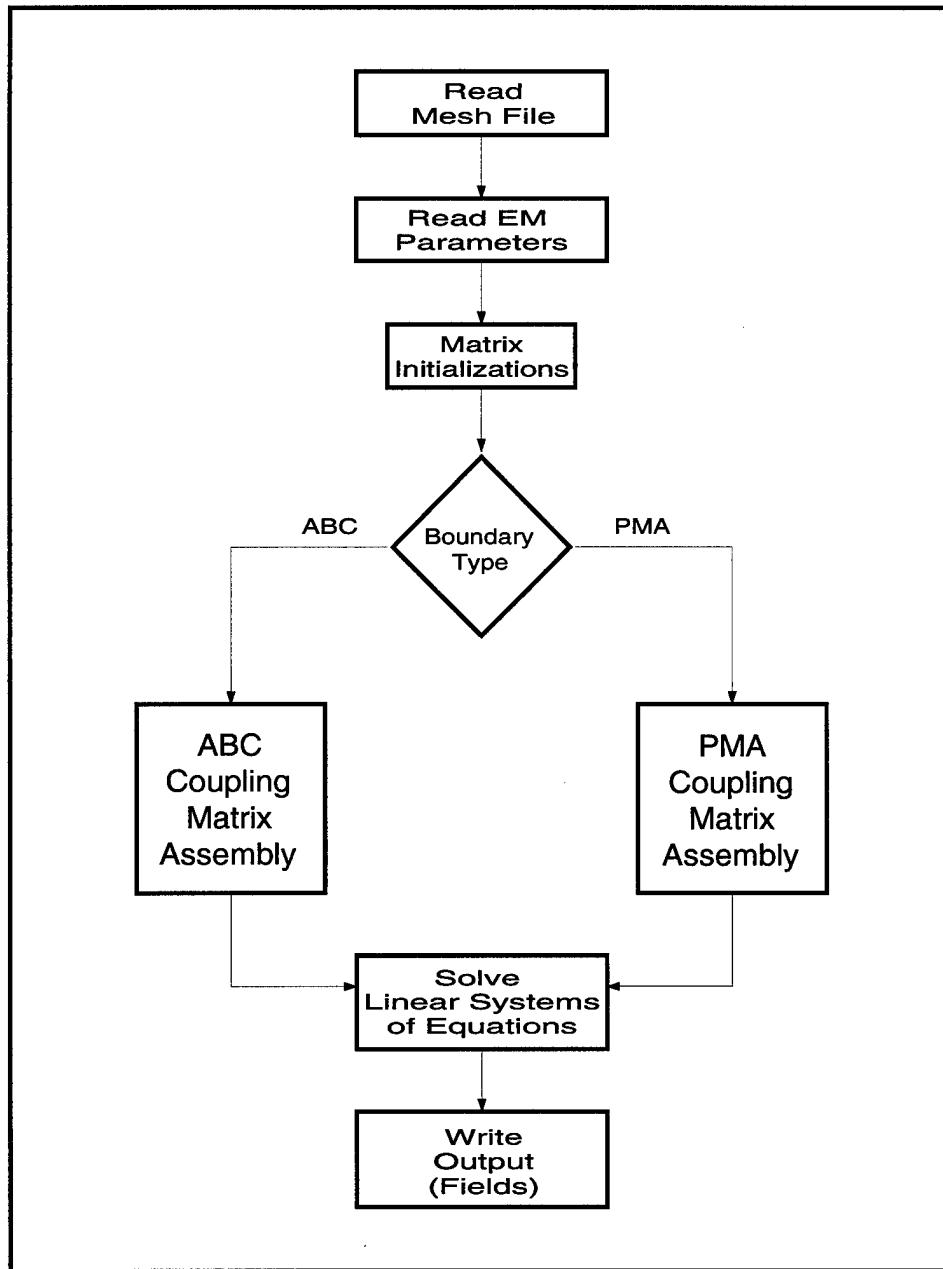
Figure 3.10   Flowchart for the FEM Code.
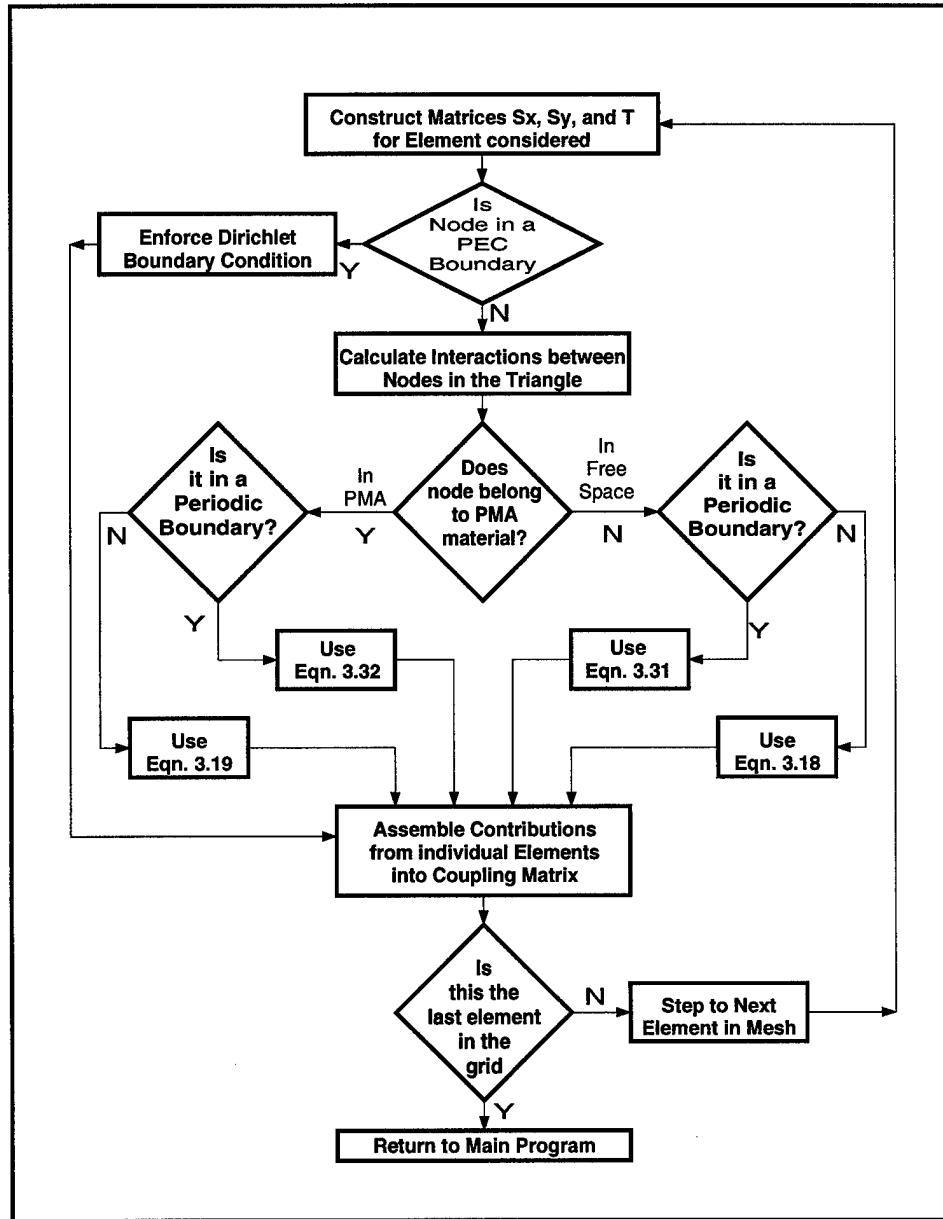
Figure 3.11 Flowchart for the Modified Subroutine for Implementing the Single Periodic Boundary.

IV. Analysis of Results

The previous chapter outlined the theory leading to the calculation of the fields scattered by a semi-infinite periodic structure. This chapter compares the FEM results from a periodic structure with two finite arrays of different lengths. The objective is to establish the validity of substituting a periodic boundary in place of the truncated part of a semi-infinite array. The concept of the physical basis function is used to verify this.

4.1 Comparison of a Fifteen-Cylinder Finite Periodic Array With A Five-Cylinder Finite Periodic Array at 90° Incidence.

The total field magnitude map generated by a plane wave illuminating the 15-cylinder array at 90° incidence is shown in Figure 4.1. Looking at the contour plot, 90° incidence is coming from the top, in the plane of the paper. Visually inspecting the contour map, the uniformity of the fields at the central portion of the array is evident. It also shows the perturbations at the edges. Further inward from the edges, the fields gradually approach a uniform pattern in the central portion of the array. The bottom plot of Figure 4.1 shows a surface plot of the fields.

To show the PBF concept, we start by taking the fields in the vicinity of the central cylinder (cylinder 8) and subtracting the fields from the adjacent cylinders (7 or 9, cylinder 1 is the left edge). The difference in field magnitudes between cylinders 8 and 7 is shown in Figure 4.2, and the difference in field magnitudes between cylinders 8 and 9 is shown in Figure 4.3. The difference plots show that the field values vary by no more than 1% of the field magnitudes in the vicinity of cylinder 8. This comparison is done by taking the highest magnitude of the field in the vicinity of cylinder 8 and the difference in field magnitudes between cylinder 8 and the the other cylinders,

$$\frac{max[Cyl_8 - Cyl_x]}{max[Cyl_8]} \; x \; 100\%. \tag{4.1}$$

Outlying Periods	Max. Field Difference	Percent Difference
Cylinder 7	0.021	1.0
Cylinder 6	0.043	2.0
Cylinder 5	0.070	3.3
Cylinder 4	0.093	4.4
Cylinder 3	0.130	6.2

Table 4.1   Percent Difference in Field Magnitudes Between the Central Period of the 15-Cylinder Finite Array and its Outlying Periods

Table 4.1 shows the percentage differences between the central cylinder (cylinder 8) and the outlying cylinders. For an arbitrary cutoff of 5% difference, it is safe to say that the fields after cylinder 3 can be defined as the "steady state" portion of the fields in the array. Therefore, in order to implement a semi- infinite cylinder, the truncation point or the placement of the periodic boundary must occur after 4 periods. To further provide a margin for numerical error as well as a "convenient" round number ratio between the number of the semi-infinite array is modeled with an additional of 5 periods before the truncation point. Figures 4.4 and 4.5 show the differences in field values between cylinders 8 and 6, and cylinders 8 and 5 respectively.
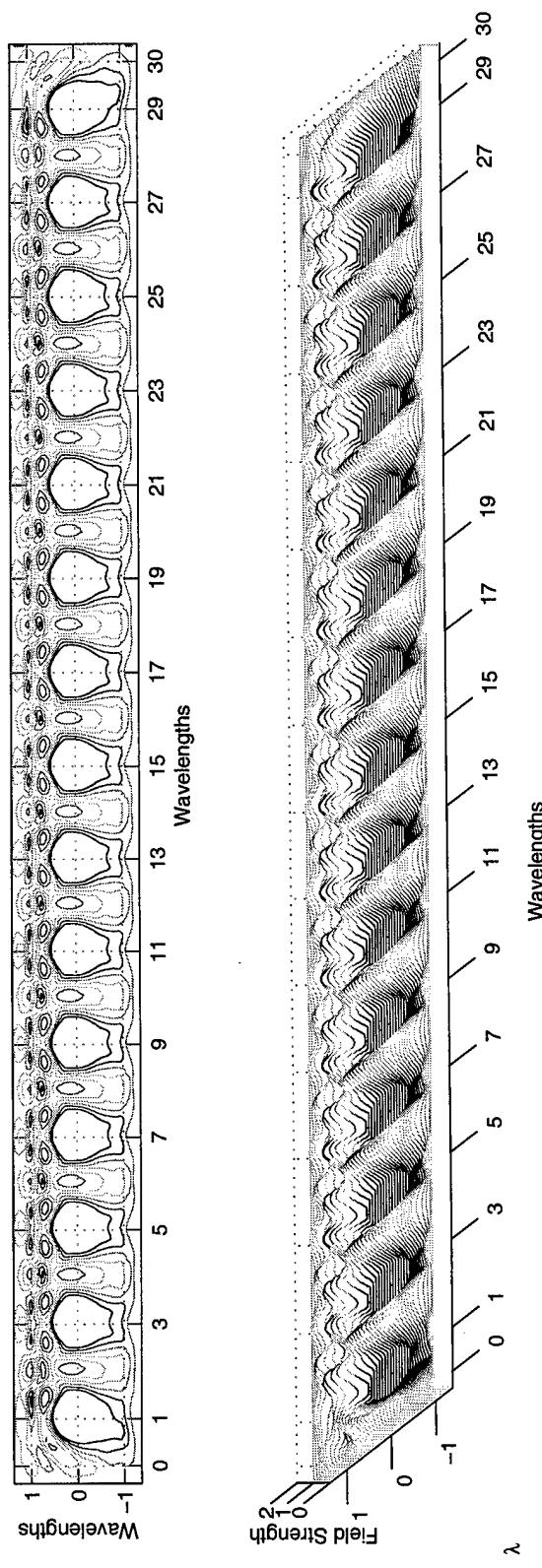
Figure 4.1 Contour Plot and Map of Total Field Values in a 15-Cylinder Finite Array at 90° Incidence.
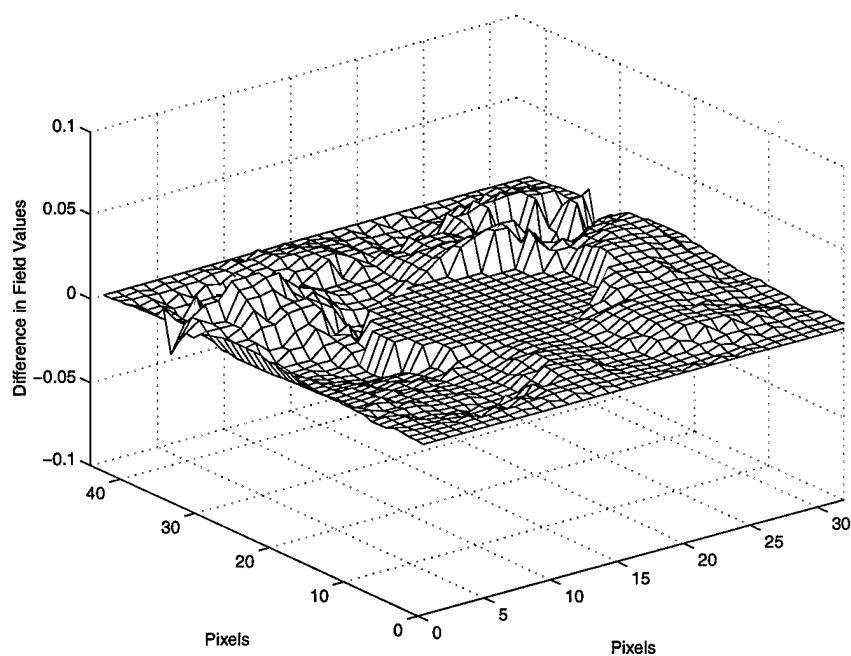
Figure 4.2   Difference in Field Values Between Cylinders 8 and 7 of the Fifteen-Cylinder Finite Array at 90° Incidence

Figure 4.6 shows the fields from a five-cylinder finite array. It is obvious that the fields are also nearly symmetric with respect to the center cylinder. It should be obvious that subtracting the fields of a five-cylinder array from the fields of a fifteen-cylinder array, with the left edges aligned, would result in a large variation in the difference plots at the fifth cylinder. Figure 4.7 shows the difference in field values for the first five cylinders of the 15-cylinder finite array and the 5-cylinder finite array. Figure 4.8 shows the difference in field values at the fifth cylinder. Note the scale difference from the previous plots.

4.2   Comparison of a Fifteen-Cylinder Finite Periodic Array With A Five-Cylinder Semi-Infinite Periodic Array at 90° Incidence.

The purpose of implementating a periodic boundary on the truncated part of a periodic array is to simulate a physical continuity of periodic elements. It should also eliminate the edge diffraction that would otherwise occur at the discontinuity. As seen from the previous section, the right boundary of the 5-cylinder array showed huge differences in the fields.

4-4
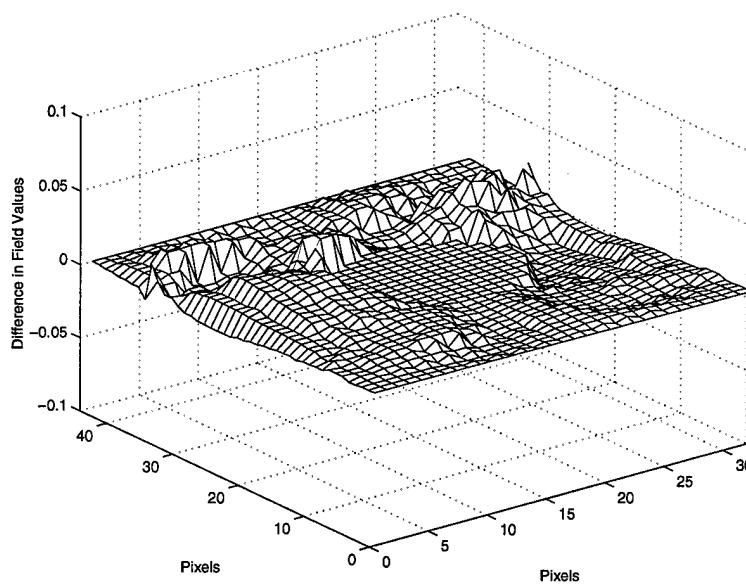
Figure 4.3   Difference in Field Values Between Cylinders 8 and 9 of the Fifteen-Cylinder Finite Array at 90° Incidence
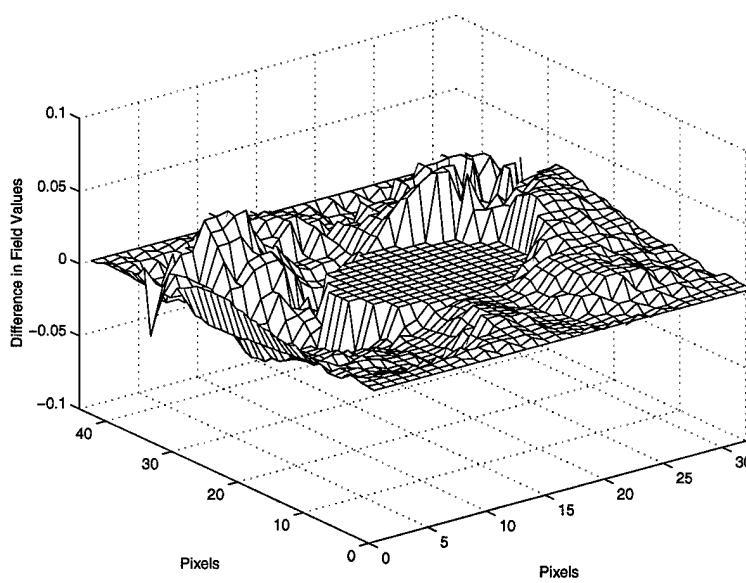

Figure 4.4   Difference in Field Values Between Cylinders 8 and 6 of the Fifteen-Cylinder Finite Array at 90° Incidence
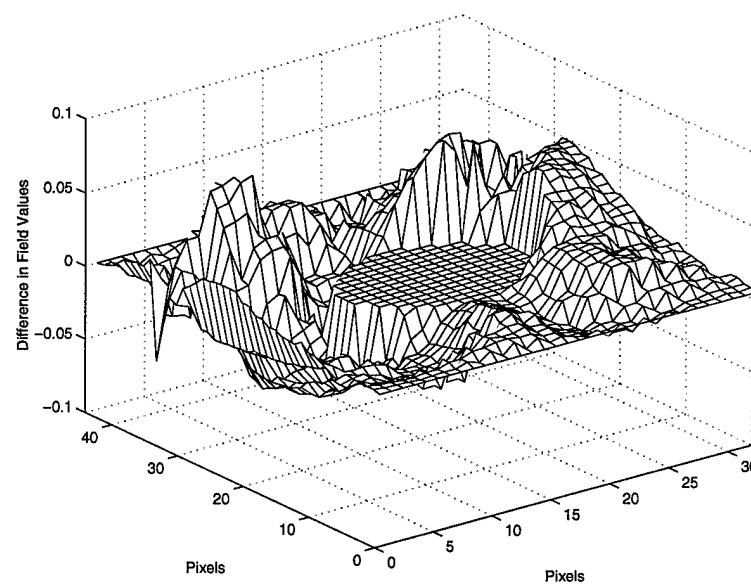
Figure 4.5   Difference in Field Values Between the Areas of Cylinders 8 and 5 in the 15-Cylinder Finite Array at 90° Incidence
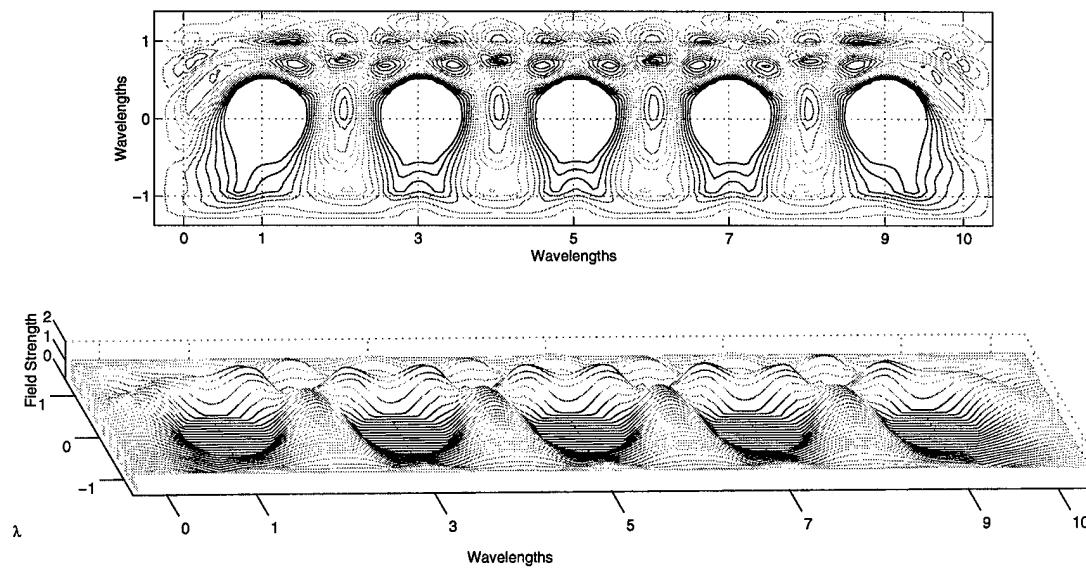

Figure 4.6   Contour Plot and Total Field Map of a 5-Cylinder Finite Array at 90° Incidence
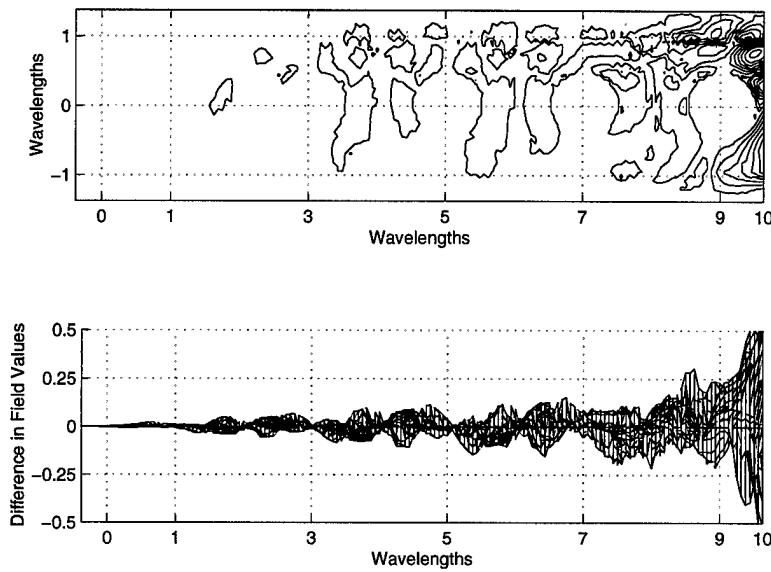
Figure 4.7   Contour Plot and Difference in Field Values Between the First Five Cylinders of the 15-Cylinder and 5-Cylinder Finite Arrays at 90° Incidence
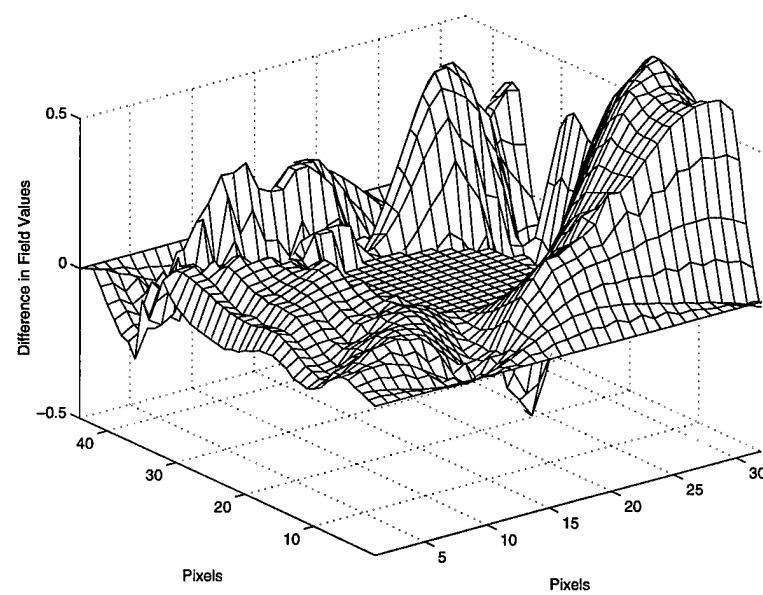

Figure 4.8   Cylinder 5 Field Differences Between the 5-Cylinder Finite Array and the 15-Cylinder at 90° Incidence
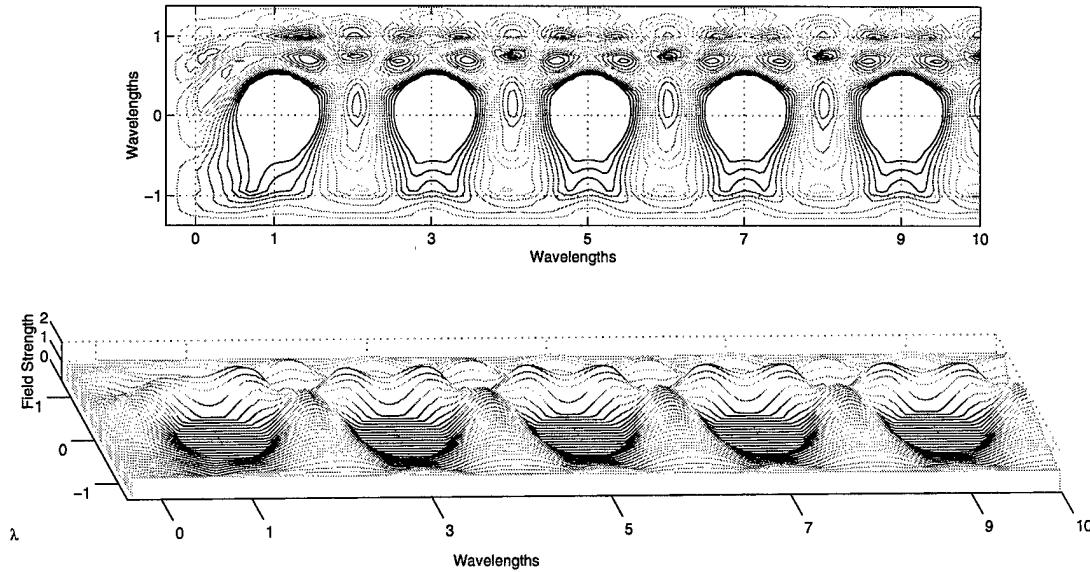
Figure 4.9   Difference in Cylinder 5 Field Values for Both 15-Cylinder Finite and 5-Cylinder Semi-Infinite Arrays at 90° Incidence.

Taking the 5-cylinder finite array and replacing the right edge with a periodic boundary converts the geometry into a semi-infinite geometry as far as FEM is concerned.

Figure 4.9 shows the total fields of the semi-infinite array. Visually inspecting the fields, one can see the significant change in the field behavior near the periodic boundary. Figure 4.11 shows the difference in field values between cylinder 5 of the 15-cylinder finite array and cylinder 5 of the simulated semi-infinite array. Comparing Figure 4.11 with Figure 4.8, the periodic boundary performs effectively.

4.3 Other Incidence Angles

The results presented thus far involved 90° incidence. For off-normal incidence, the periodic boundary does not perform as well as at normal incidence. This is evident in the field plots of the semi-infinite array. Taking the 75° incidence as an example, the contour and field map from the semi-infinite array is shown in Figure 4.12. The field and contour map from the finite array is shown in Figure 4.13.

Looking at the field patterns in the vicinity of the cylinder next to the periodic boundary (right edge) in Figure 4.12, and comparing that with the field pattern one can see the
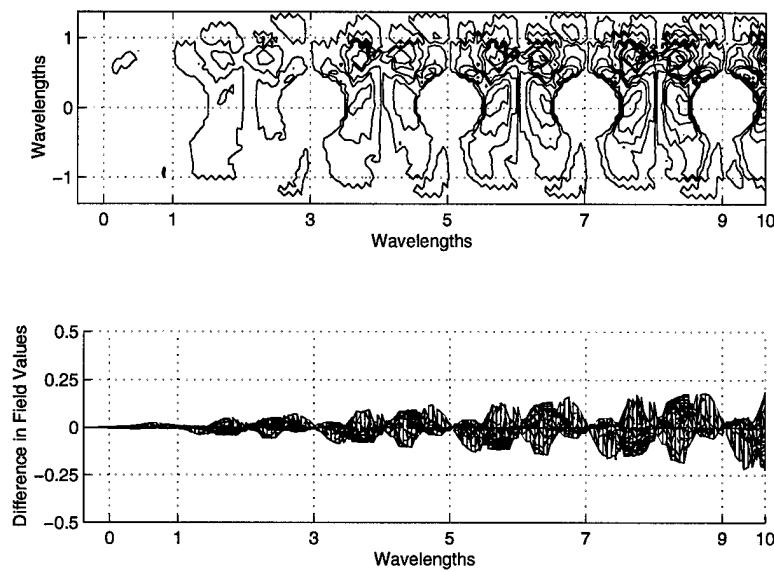
Figure 4.10   Difference in Field Values for Both 15-Cylinder Finite and 5-Cylinder Semi-Infinite Arrays at 90° Incidence.
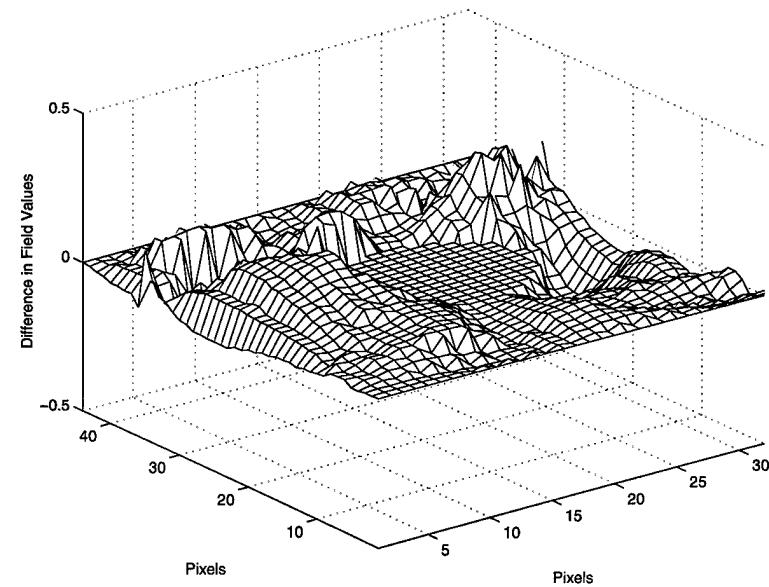

Figure 4.11   Difference in Cylinder 5 Field Values for Both 15-Cylinder Finite and 5-Cylinder Semi-Infinite Arrays at 90° Incidence.
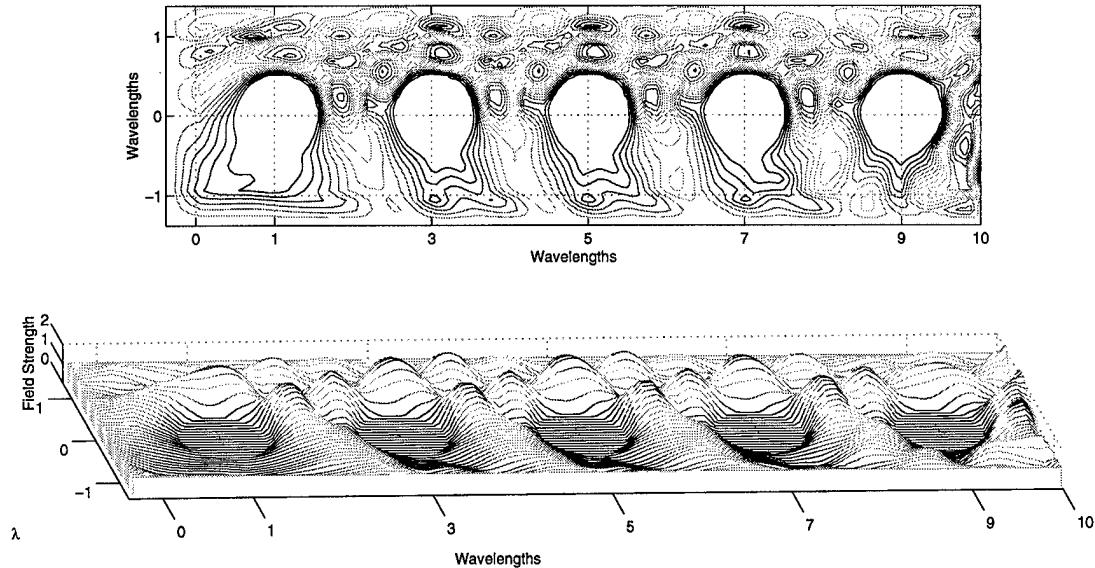
Figure 4.12   Contour Plot and Total Field Map of a 5-Cylinder Semi-Finite Array at 75°
Incidence

discrepancies in the implemented periodic boundary. Comparing fifteen-cylinder array shown in Figure 4.1 with the five-cylinder can immediately recognize the disturbance in periodic boundary. The fields do not with a periodic array.

The difference in the field values between the first five periods of the fifteen-cylinder finite array and semi-infinite array is shown in Figure 4.14. The difference in the field values between the fifteen-cylinder finite array and the five-cylinder finite array is shown in Figure 4.15. is apparent that the periodic boundary does not perform as expected.

Several factors may contribute to the failure of the periodic most likely explanation is that the boundary is the solution domain. The phase factor, at the periodic boundary would At normal incidence and therefore While at other incident angles, reflection at the boundary occurs and energy would be added into the solution.

4.4   Alternative Implementation of the Periodic Boundary

The periodic boundary implementation presented here suggests that the performance of an "open-circuit" boundary is not sufficient in fully characterizing the fields in a semi-infinite periodic array. The next logical step, given enough time, would be to implement a
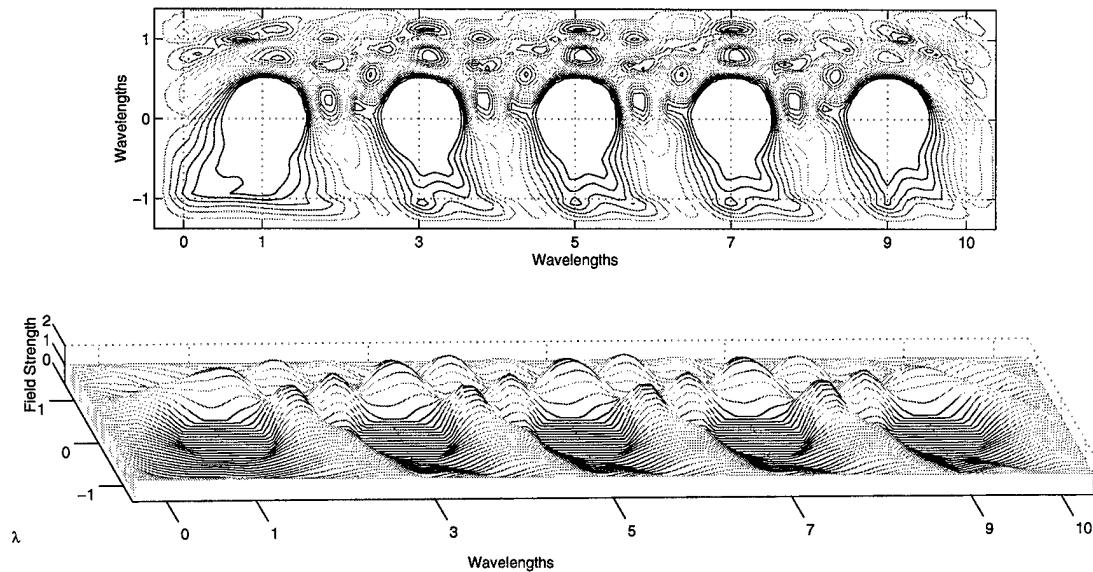
Figure 4.13   Contour Plot and Total Field Map of a 5-Cylinder Finite Array at 75° Incidence
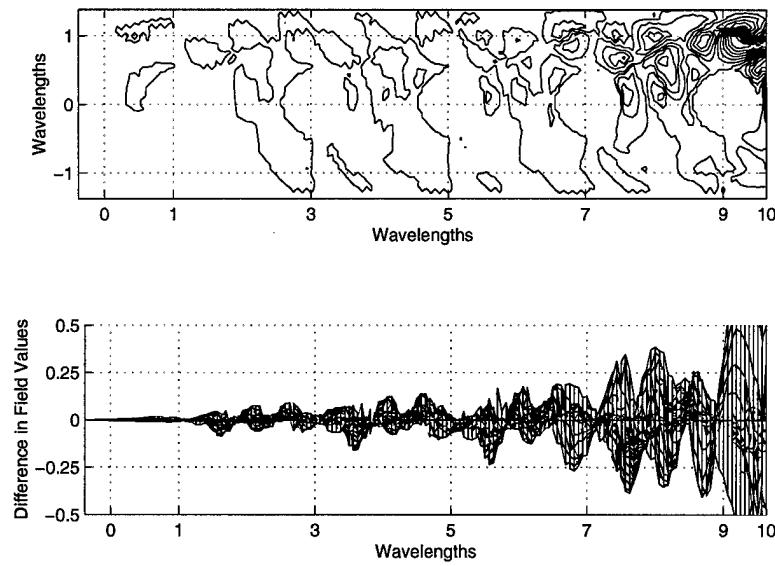

Figure 4.14   Contour Plot and Field Difference Plot for the First Five Periods of the 15-Cylinder and 5-Cylinder Finite Arrays at 75° Incidence
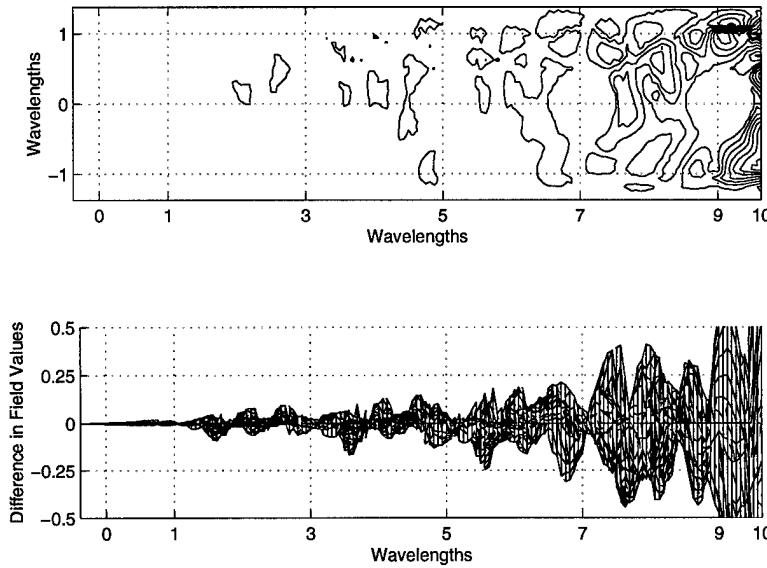
Figure 4.15   Contour Plot and Field Difference Plot for the First Five Periods of the 15-Cylinder Finite Array and the Semi-Finite Array at 75° Incidence

"folding over" of the periodic boundary with the opposite side of the unit cell containing cylinder 5 (the cylinder next to the periodic boundary). Referring to Figure 4.16, the field values at the nodes in the periodic boundary are related to the field values a distance of one period from the boundary.
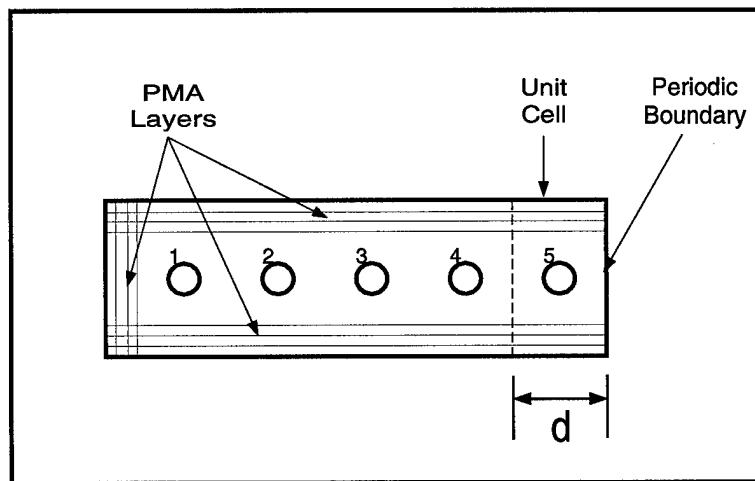
Figure 4.16   Implementation of a Single Periodic Boundary by Relating the Fields in the
Interior One Periodic From the Periodic Boundary

V. Conclusion and Recommendations

5.1 Conclusion

The objective of this thesis is to provide a framework for developing a Finite Element Method solution to semi-infinite periodic arrays by utilizing the concept of a physical basis function. It is known beforehand that the amplitude of the currents induced on the elements far enough from the edge of a semi-periodic array are constant. Based on that pretext, a periodic boundary using a Floquet expansion is implemented at a sufficient distance from the edge of a semi-infinite periodic array. However, as seen in the previous chapter, the implementation was only effective at normal incidence.

5.2 Recommendations for Further Study

A next logical step is to implement the periodic boundary by relating the fields there with the fields one interior period from the boundary (the truncation point). This amounts to performing the same procedures as in the implementation of an infinitely periodic array. However, the interior "quasi-boundary" exhibits coupling with other interior nodes outside the unit cell (see Figure 4.16).

Another approach might be implemented by using the vector finite element method (VFEM) on the "open-circuit" boundary implementation. VFEM is primarily implemented to fix the problem of spurious modes, but could be used here since the periodic boundary may be contributing anomalous solutions at off-normal incidence.

Although the length of the periodic array used is sufficiently long, the central portion of the array where the field amplitudes are "constant" is narrow. A longer steady state region would ensure that the edge effects are fully "damped" by the time it reaches the central portion of the array. A longer array would mean more nodes and elements in the finite element solution domain. Meshing usually takes a long time, and larger problems would mean longer mesh times. Thus, a more efficient or optimized mesh generator needs to be developed.

Usually in scattering and radiation problems, the RCS is one quantity of interest. RCS calculations can be done by taking a contour integral around the solution region and projected into the far field.

Finally, once the problem of calculating off-normal incidence is fixed, several applications can be implemented. Since the FEM accommodates dielectrics handily, application of material treatments for metallic edges can be studied.

Appendix A.

## A.1 Field Plots for the Fifteen-Cylinder Finite Periodic Structure
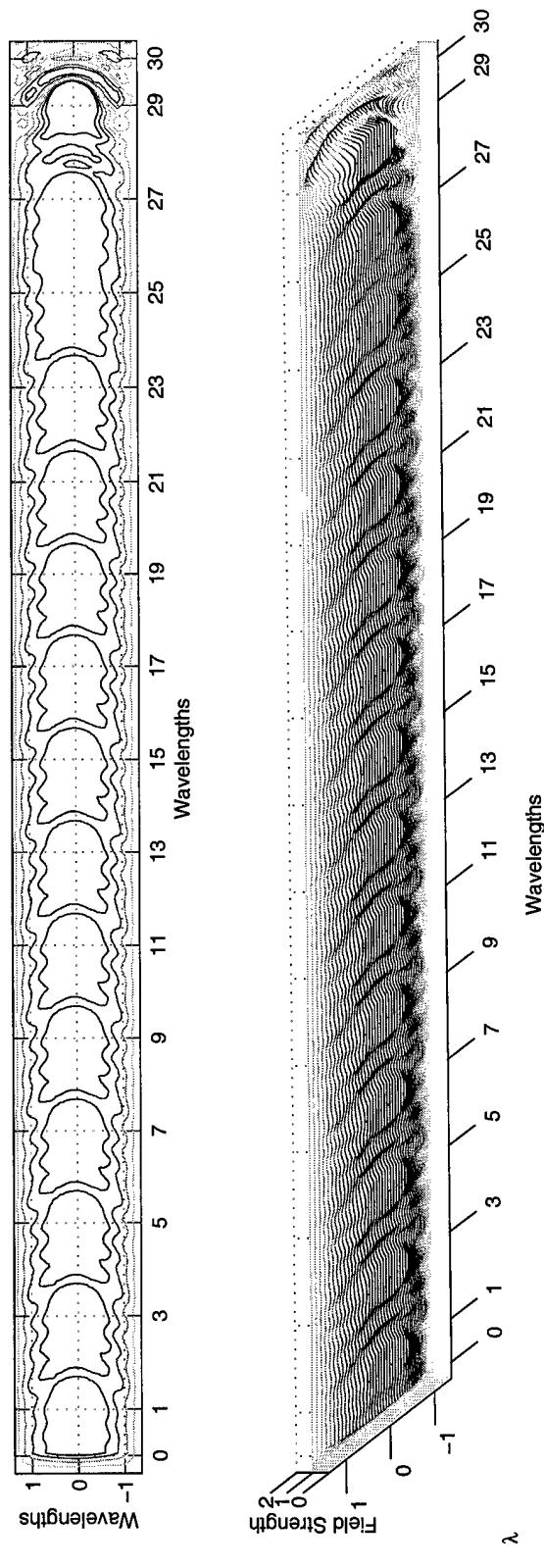
Figure A.1 Contour Map and Three-Dimensional Map of the Total Fields of a $1 - \lambda$ Diameter, 15-Cylinder Finite Array at 0° Incidence.
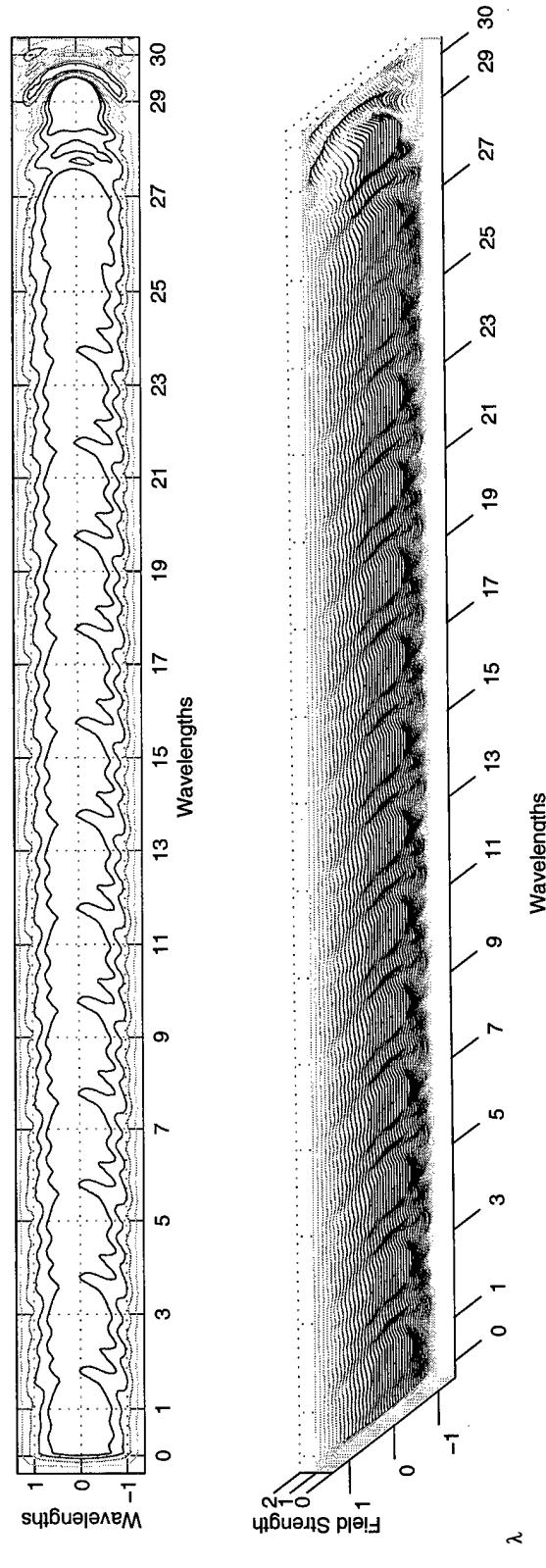
Figure A.2 Contour Map and Three-Dimensional Map of the Total Fields of a $1 - \lambda$ Diameter, 15-Cylinder Finite Array at 5° Incidence.
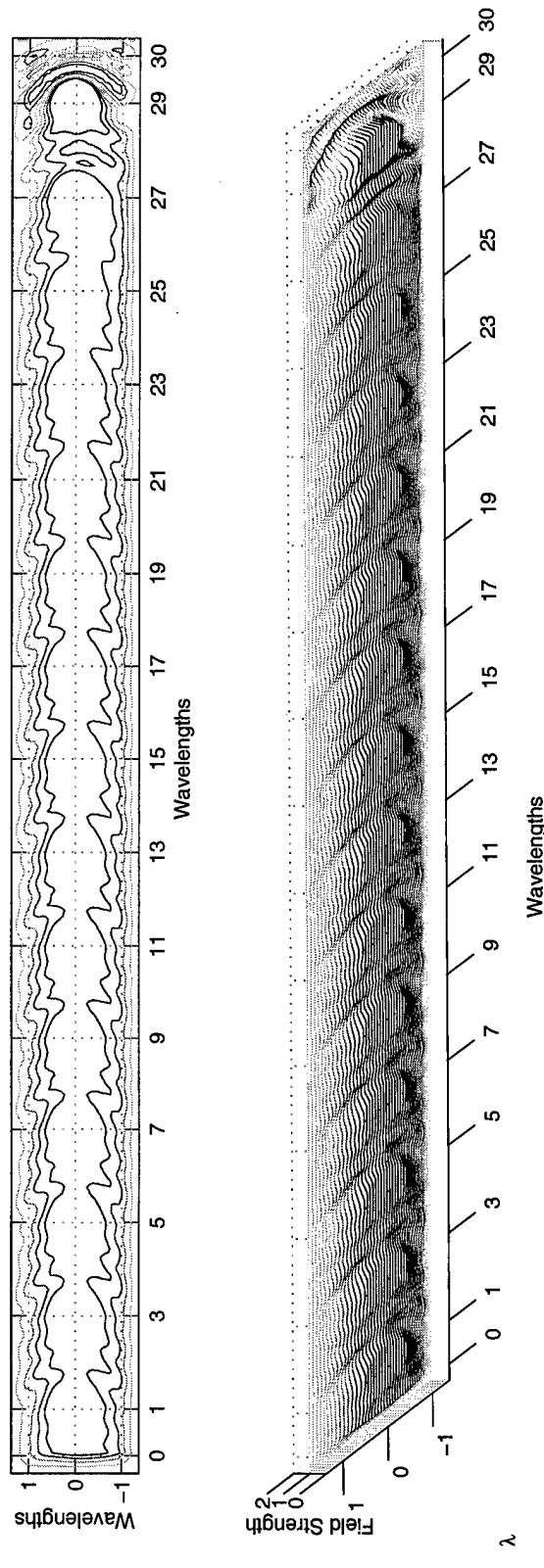
Figure A.3   Contour Map and Three-Dimensional Map of the Total Fields of a $1 - \lambda$ Diameter, 15-Cylinder Finite Array at 10° Incidence.
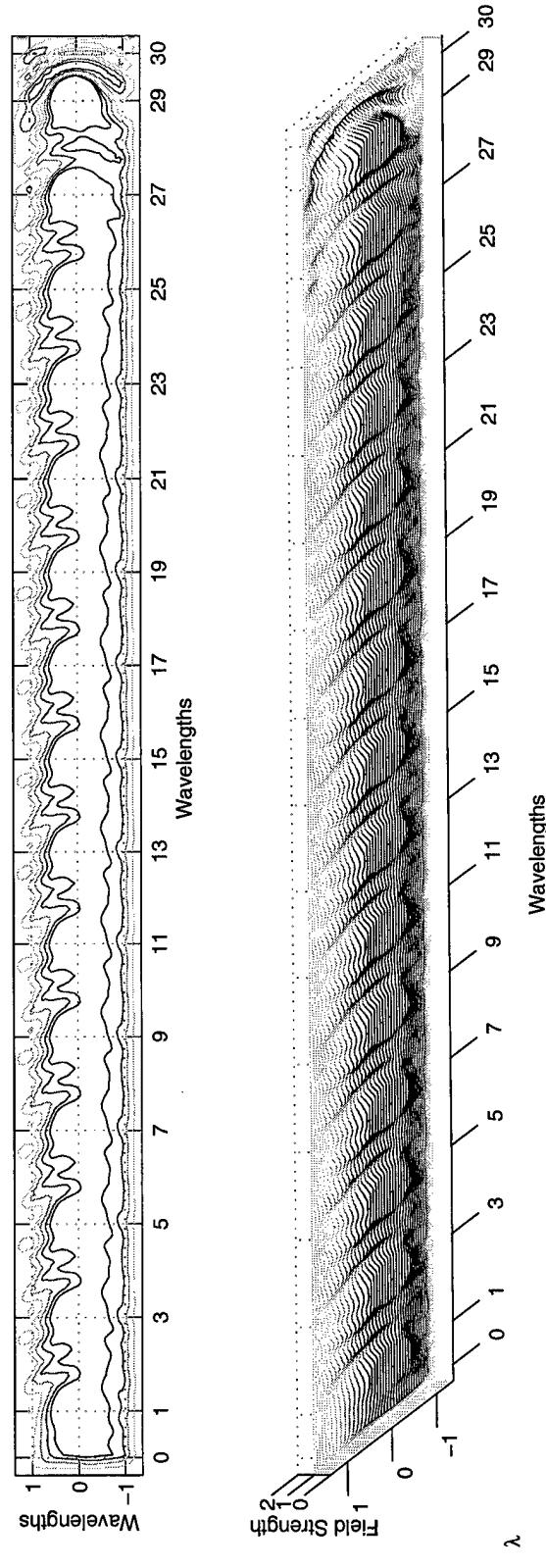
Figure A.4 Contour Map and Three-Dimensional Map of the Total Fields of a $1 - \lambda$ Diameter, 15-Cylinder Finite Array at 15° Incidence.
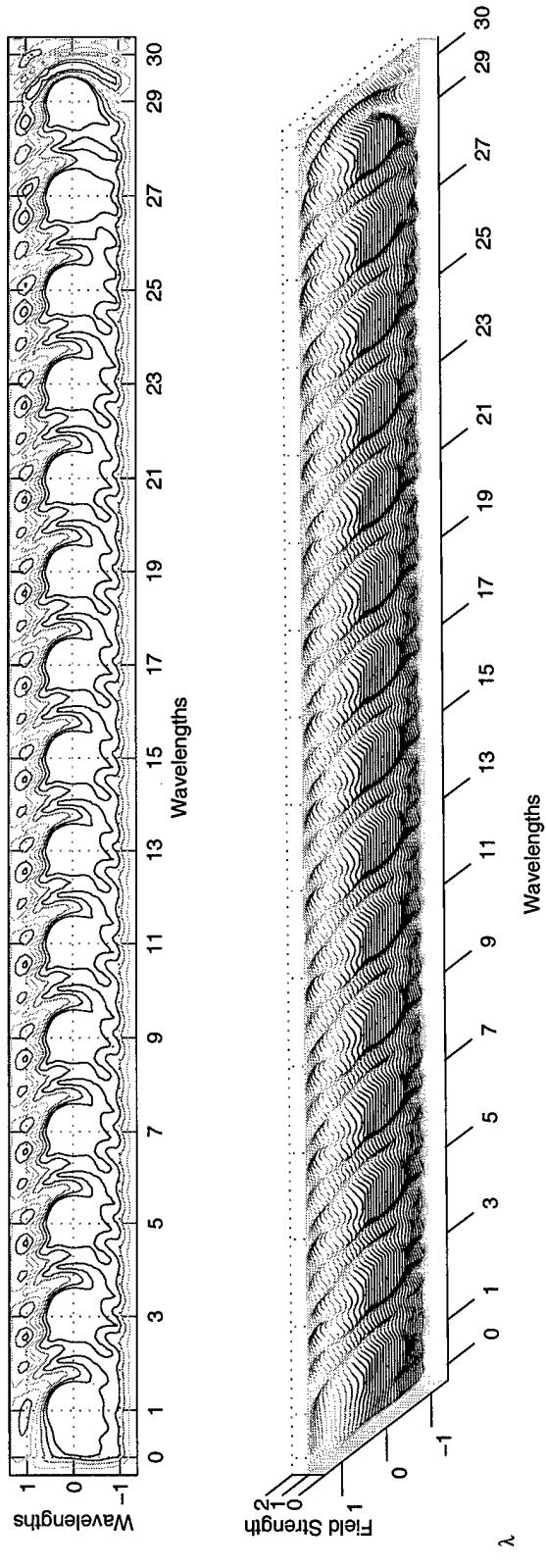
Figure A.5   Contour Map and Three-Dimensional Map of the Total Fields of a $1 - \lambda$ Diameter, 15-Cylinder Finite Array at 20° Incidence.
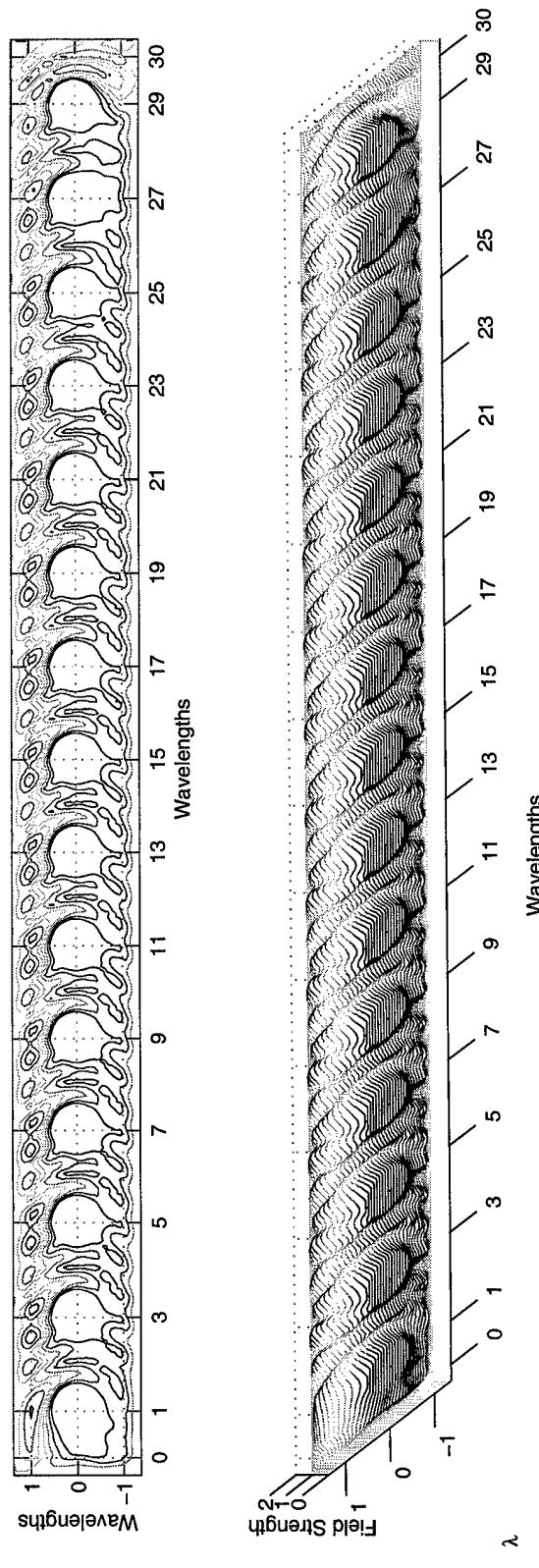
Figure A.6   Contour Map and Three-Dimensional Map of the Total Fields of a $1 - \lambda$ Diameter, 15-Cylinder Finite Array at 25° Incidence.
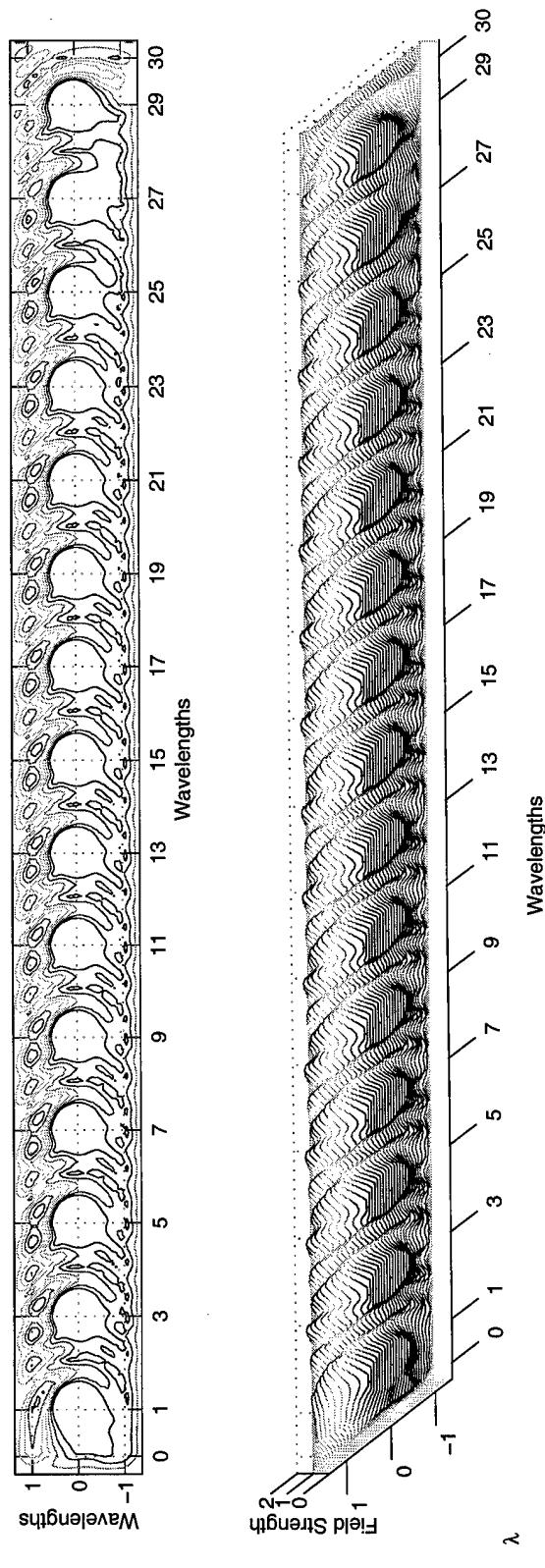
Figure A.7   Contour Map and Three-Dimensional Map of the Total Fields of a $1 - \lambda$ Diameter, 15-Cylinder Finite Array at 30° Incidence.
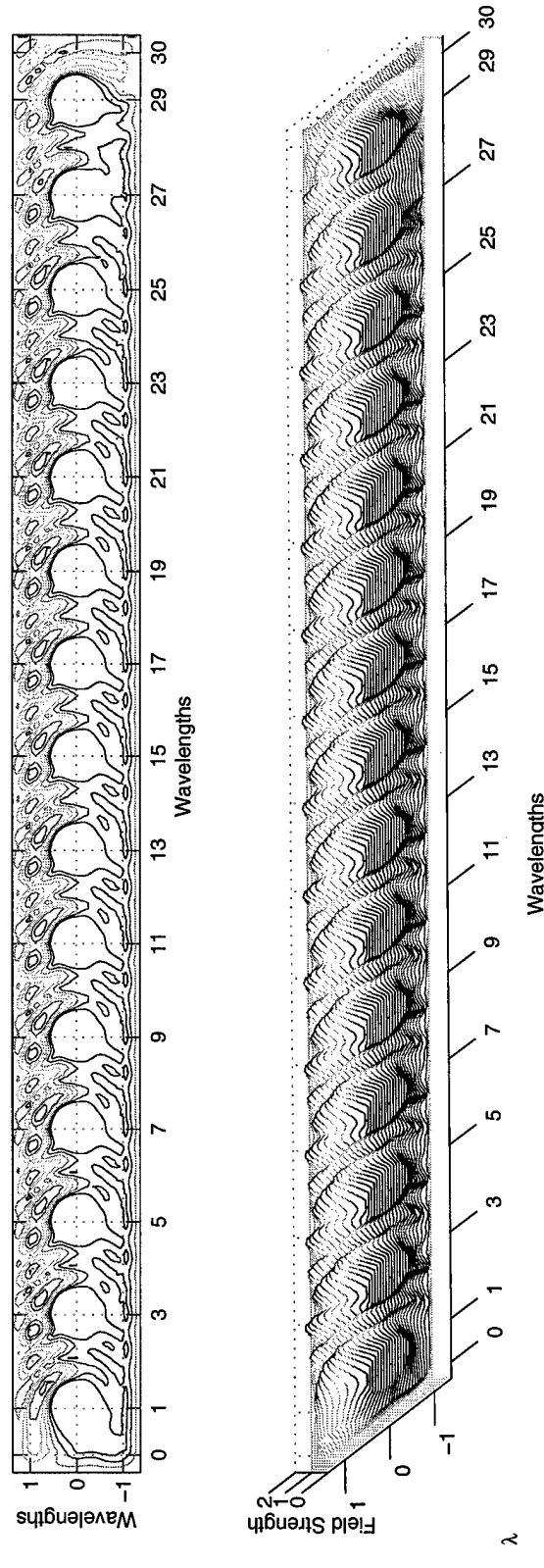
Figure A.8   Contour Map and Three-Dimensional Map of the Total Fields of a $1 - \lambda$ Diameter, 15-Cylinder Finite Array at 35° Incidence.
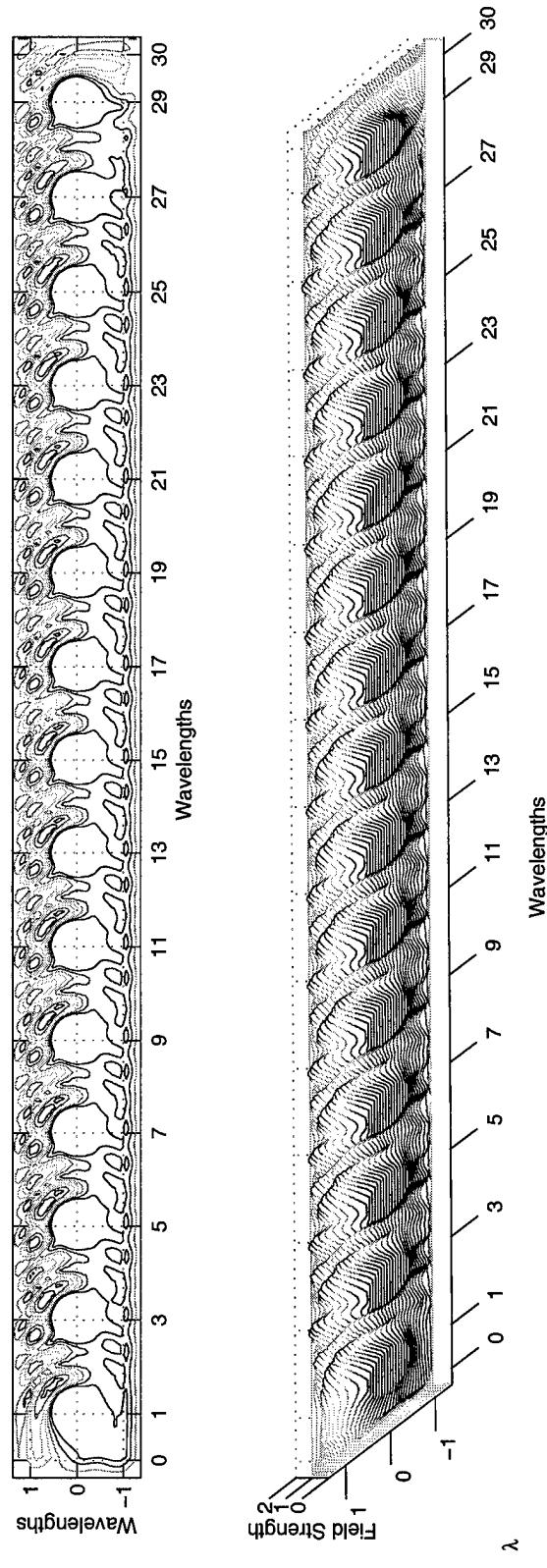
Figure A.9 Contour Map and Three-Dimensional Map of the Total Fields of a $1 - \lambda$ Diameter, 15-Cylinder Finite Array at 40° Incidence.
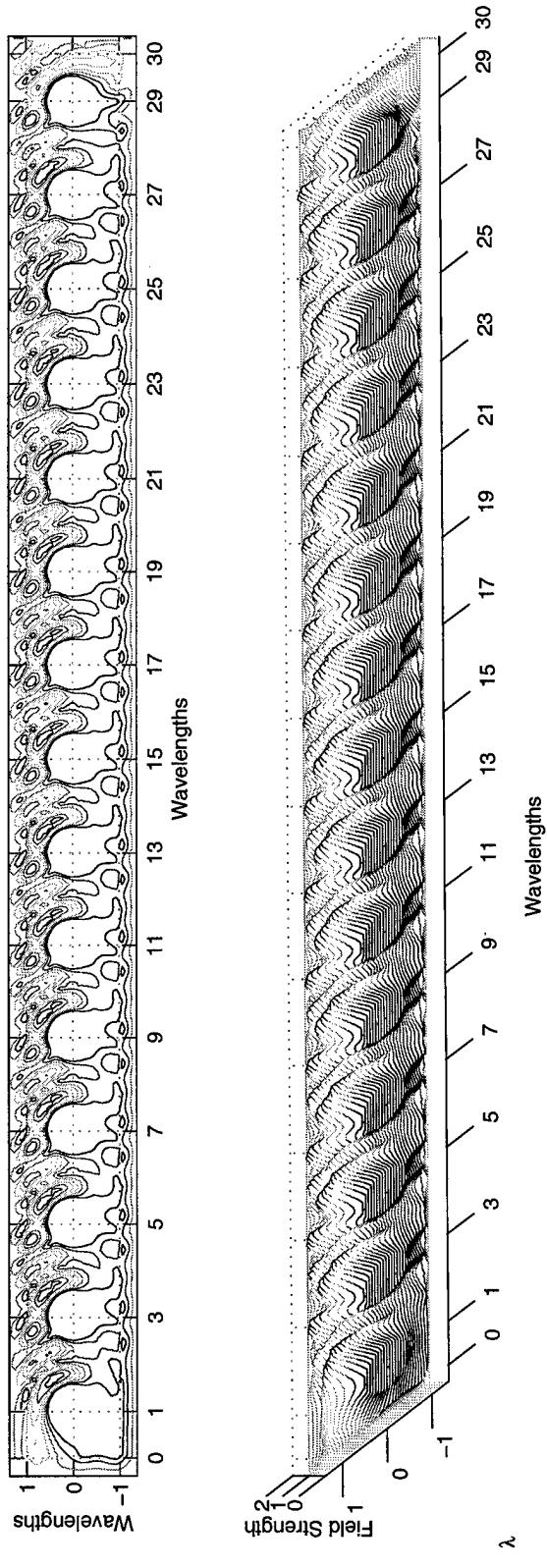
Figure A.10 Contour Map and Three-Dimensional Map of the Total Fields of a $1 - \lambda$ Diameter, 15-Cylinder Finite Array at 45° Incidence.
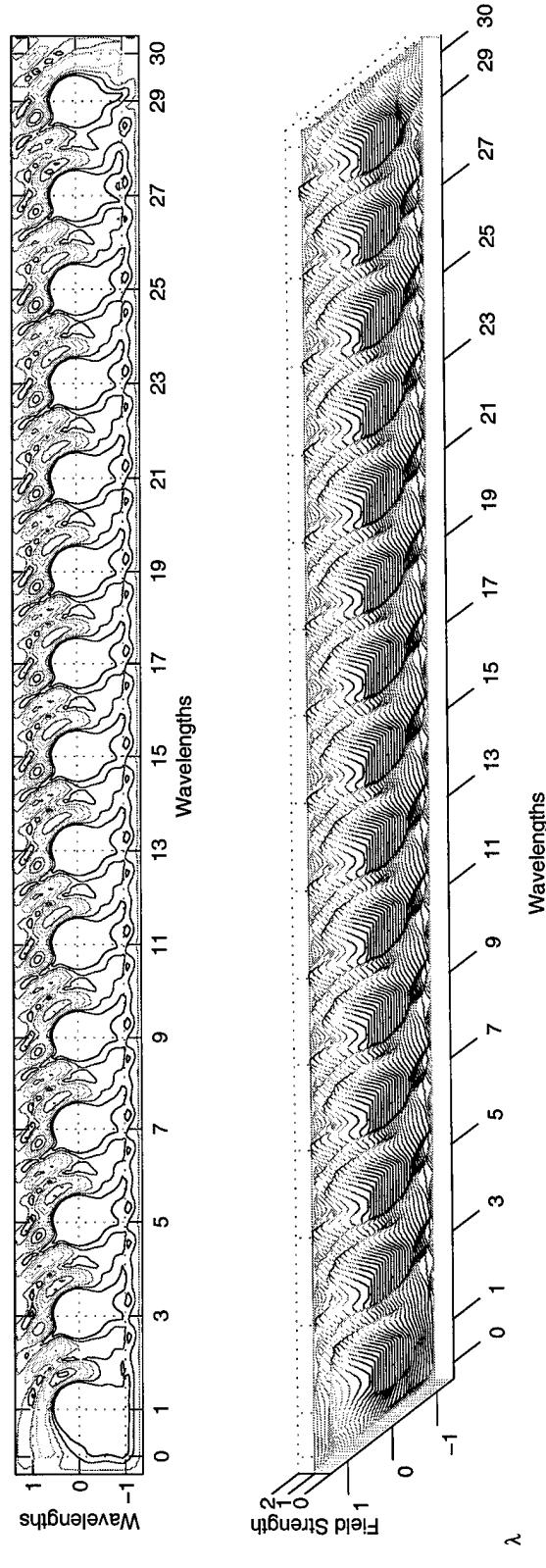
Figure A.11　Contour Map and Three-Dimensional Map of the Total Fields of a $1 - \lambda$ Diameter, 15-Cylinder Finite Array at 50° Incidence.
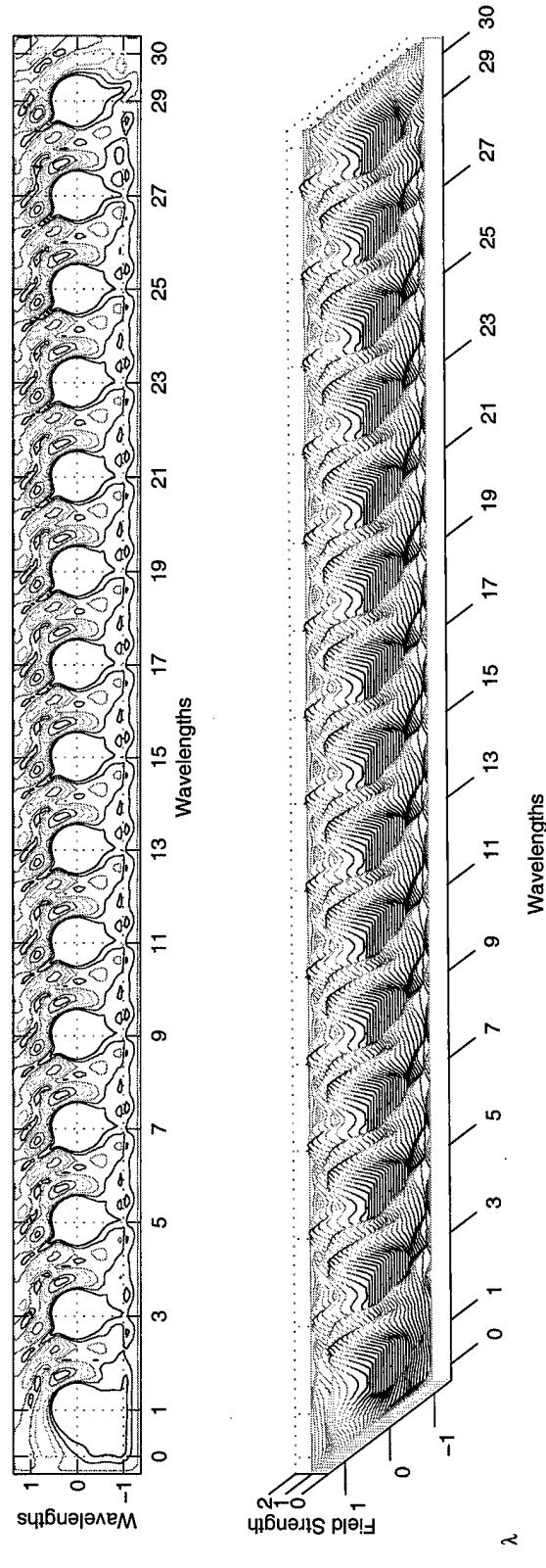
Figure A.12 Contour Map and Three-Dimensional Map of the Total Fields of a $1 - \lambda$ Diameter, 15-Cylinder Finite Array at 55° Incidence.
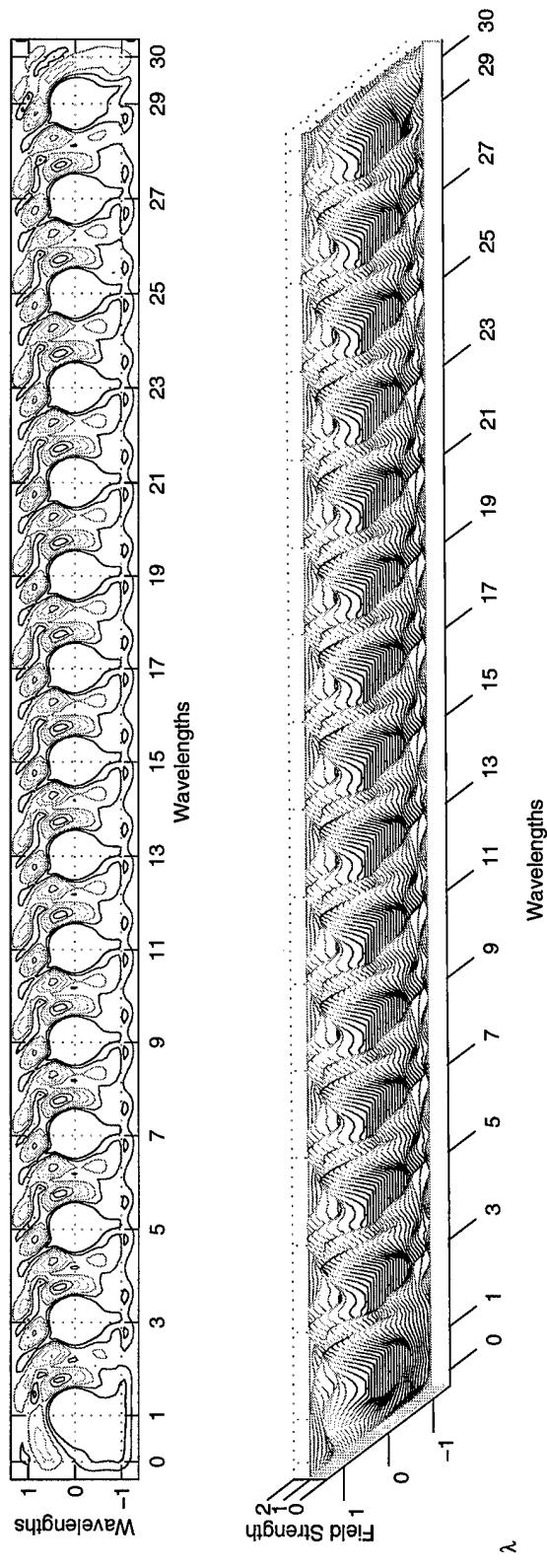
Figure A.13   Contour Map and Three-Dimensional Map of the Total Fields of a $1 - \lambda$ Diameter, 15-Cylinder Finite Array at 60° Incidence.
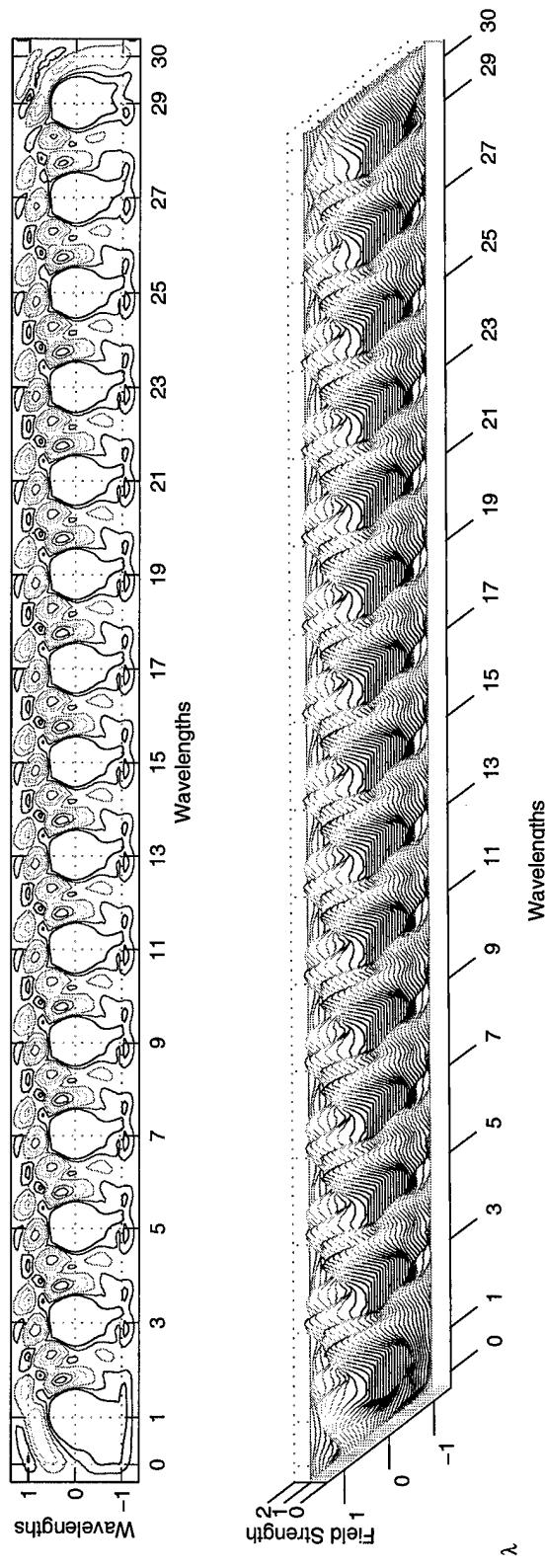
Figure A.14   Contour Map and Three-Dimensional Map of the Total Fields of a $1 - \lambda$ Diameter, 15-Cylinder Finite Array at 65° Incidence.
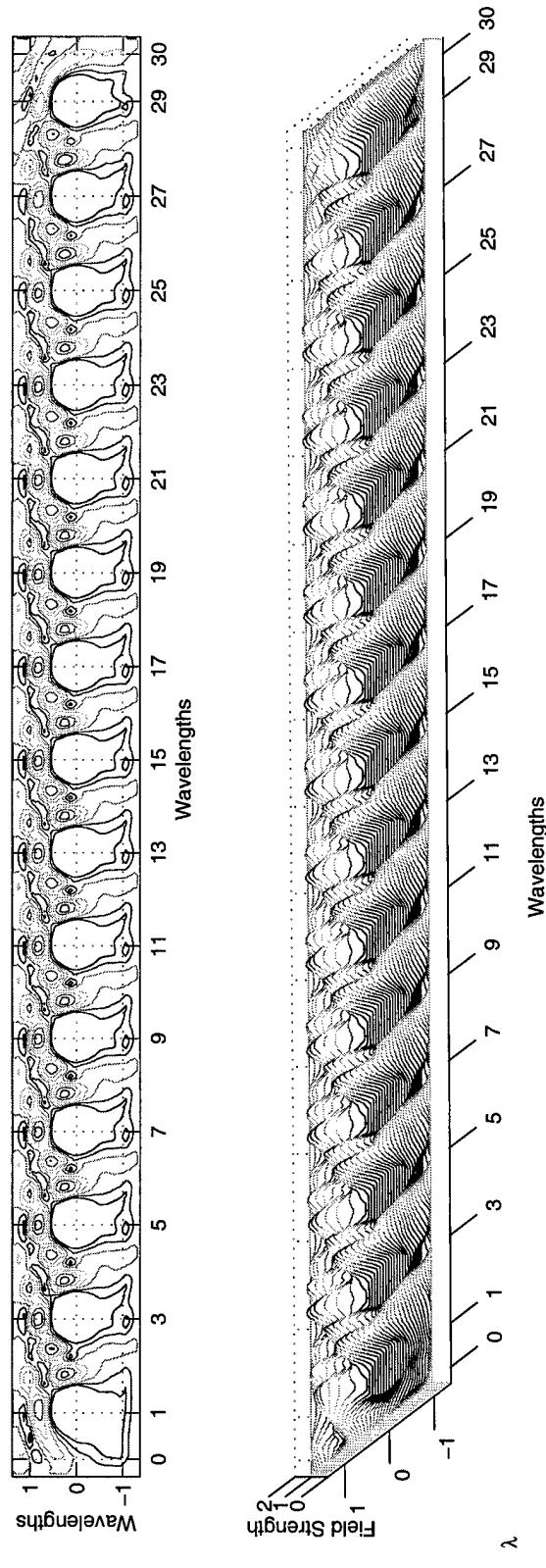
Figure A.15   Contour Map and Three-Dimensional Map of the Total Fields of a $1 - \lambda$ Diameter, 15-Cylinder Finite Array at 70° Incidence.
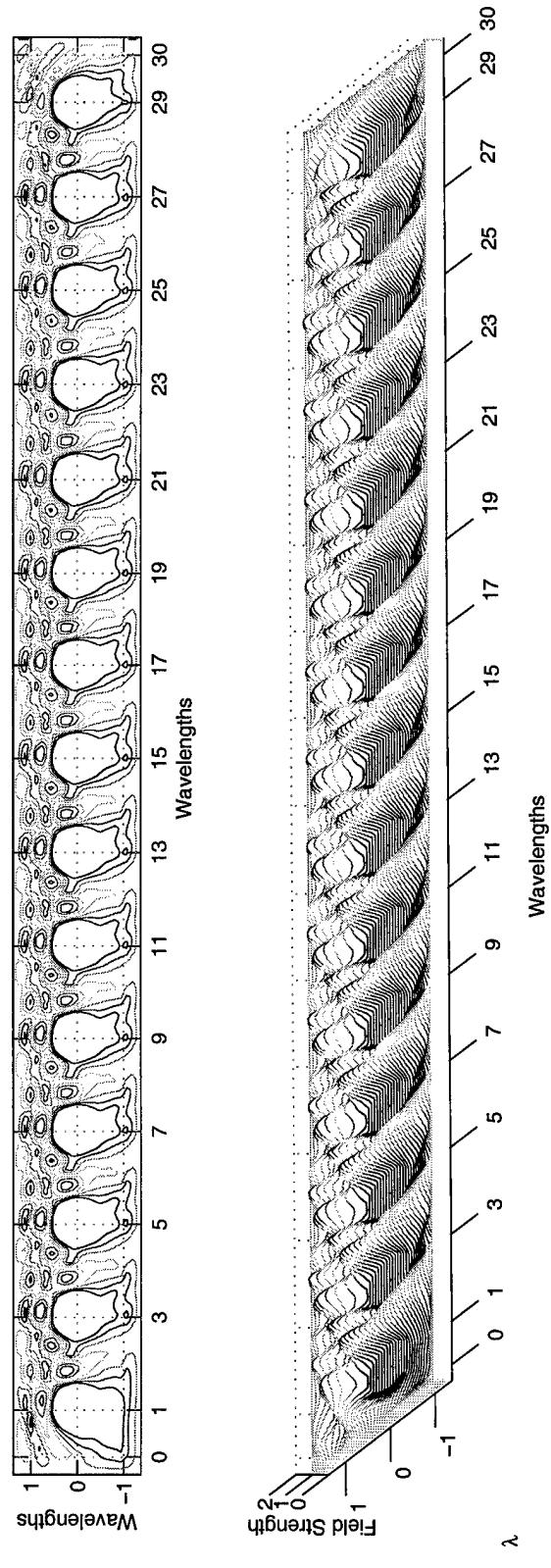
Figure A.16 Contour Map and Three-Dimensional Map of the Total Fields of a $1 - \lambda$ Diameter, 15-Cylinder Finite Array at 75° Incidence.
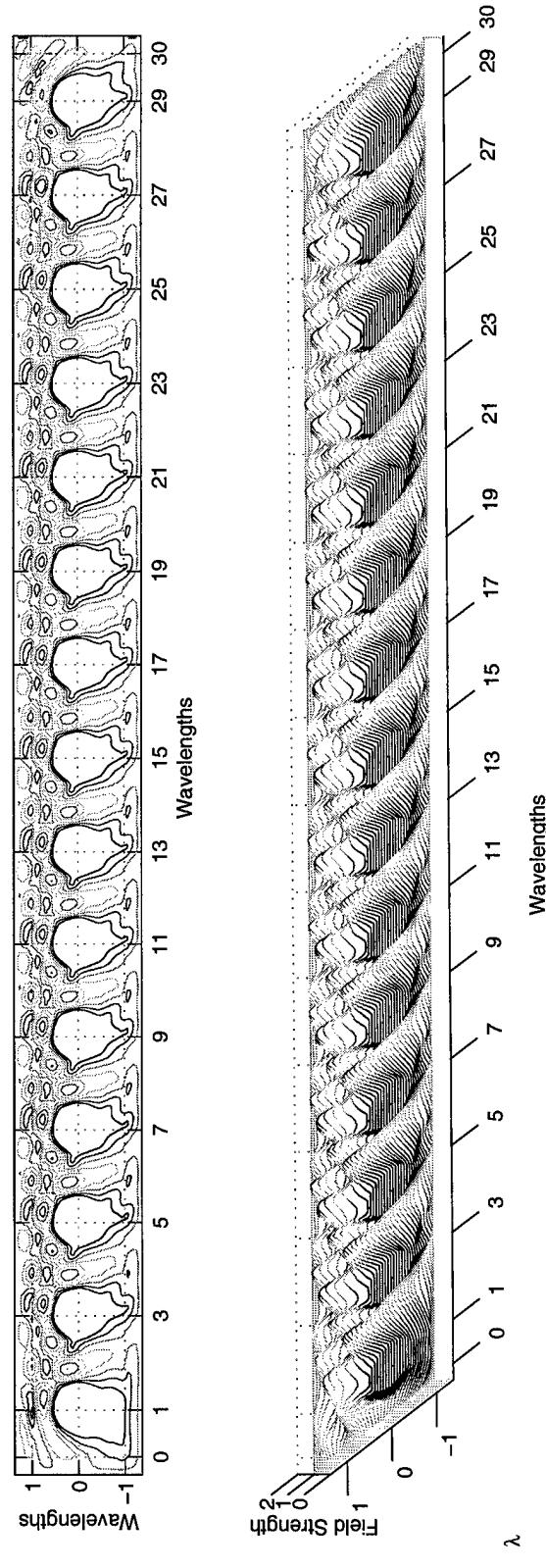
Figure A.17   Contour Map and Three-Dimensional Map of the Total Fields of a $1 - \lambda$ Diameter, 15-Cylinder Finite Array at 80° Incidence.

A-18
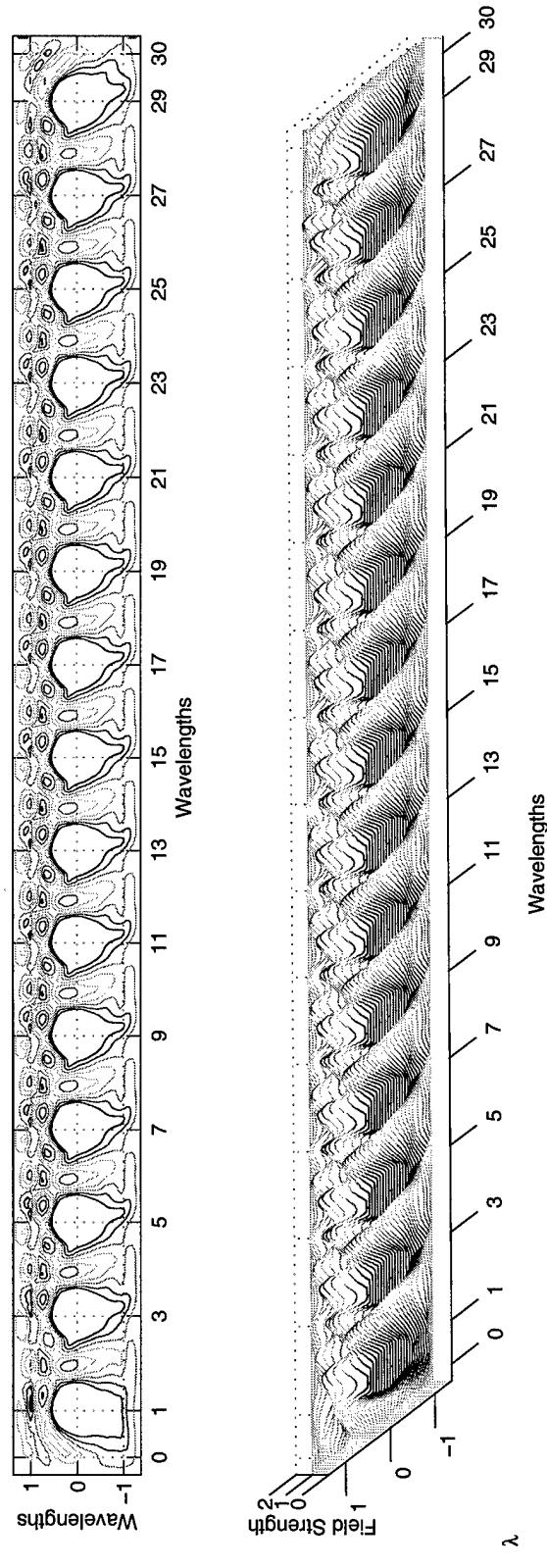
Figure A.18   Contour Map and Three-Dimensional Map of the Total Fields of a $1-\lambda$ Diameter, 15-Cylinder Finite Array at 85° Incidence.
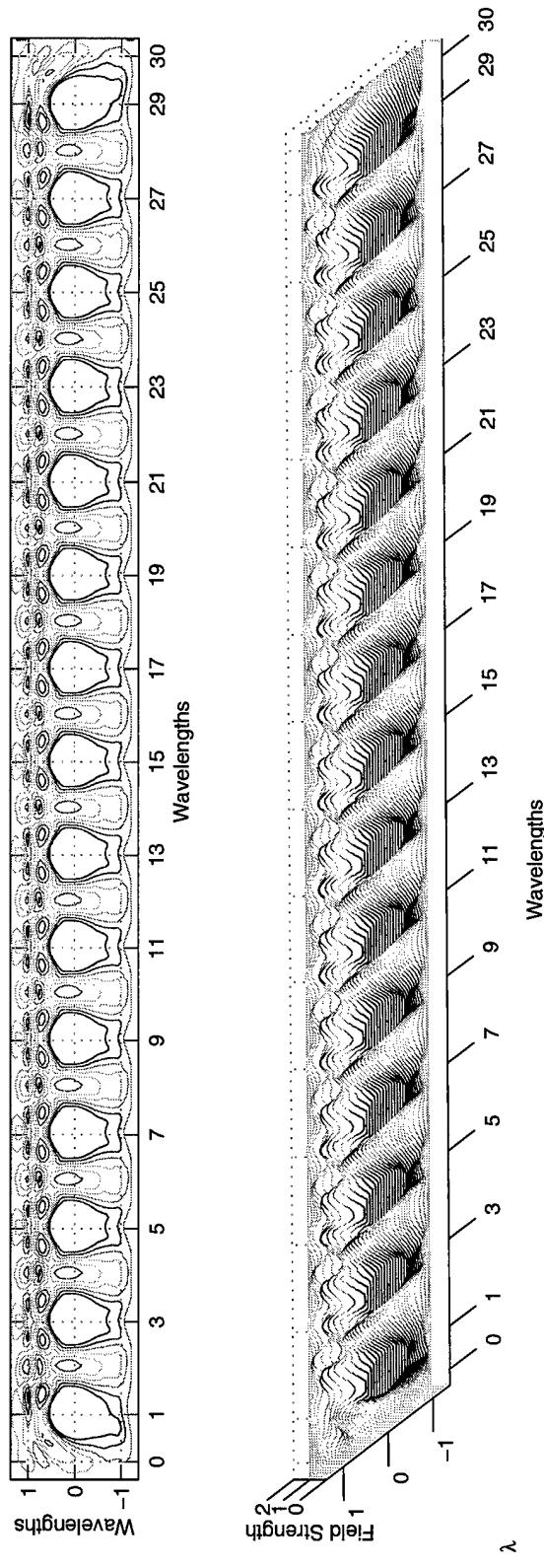
Figure A.19   Contour Map and Three-Dimensional Map of the Total Fields of a $1 - \lambda$ Diameter, 15-Cylinder Finite Array at 90° Incidence.

A.2   Field Plots for the Five-Cylinder Semi-Infinite Periodic Structure
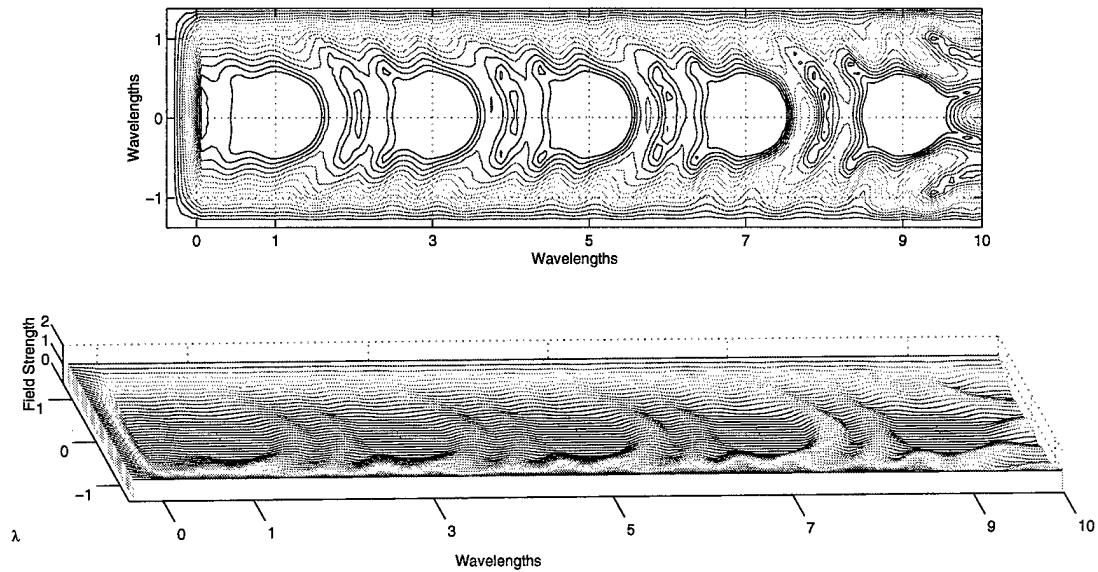
Figure A.20   Contour Map and Three-Dimensional Map of the Total Fields of a $1 - \lambda$ Diameter, 5-Cylinder Semi-Infinite Periodic Array at 0° Incidence.
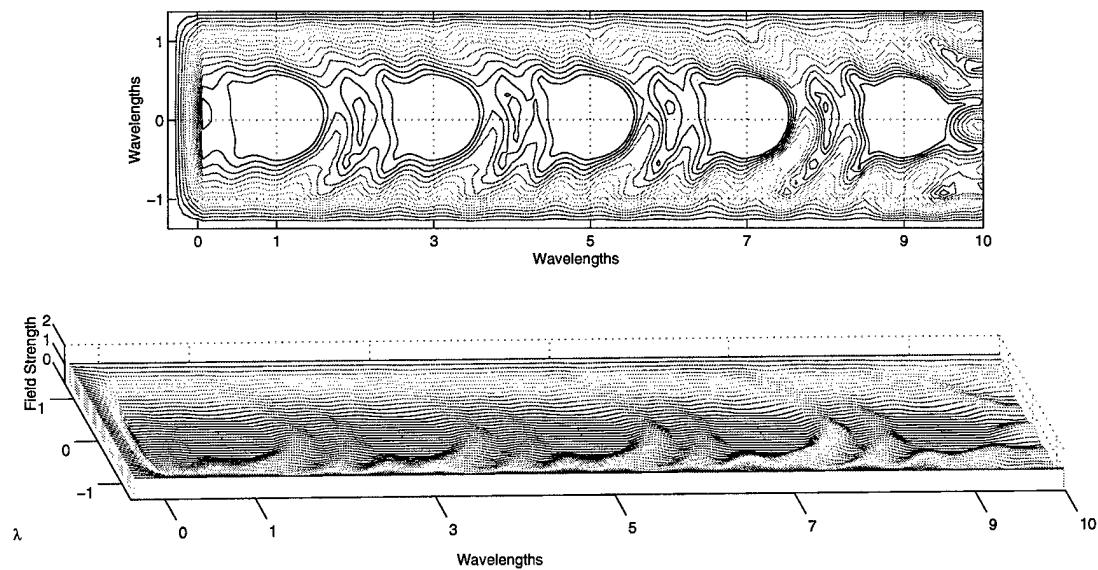
Figure A.21   Contour Map and Three-Dimensional Map of the Total Fields of a $1 - \lambda$ Diameter, 5-Cylinder Semi-Infinite Periodic Array at 5° Incidence.
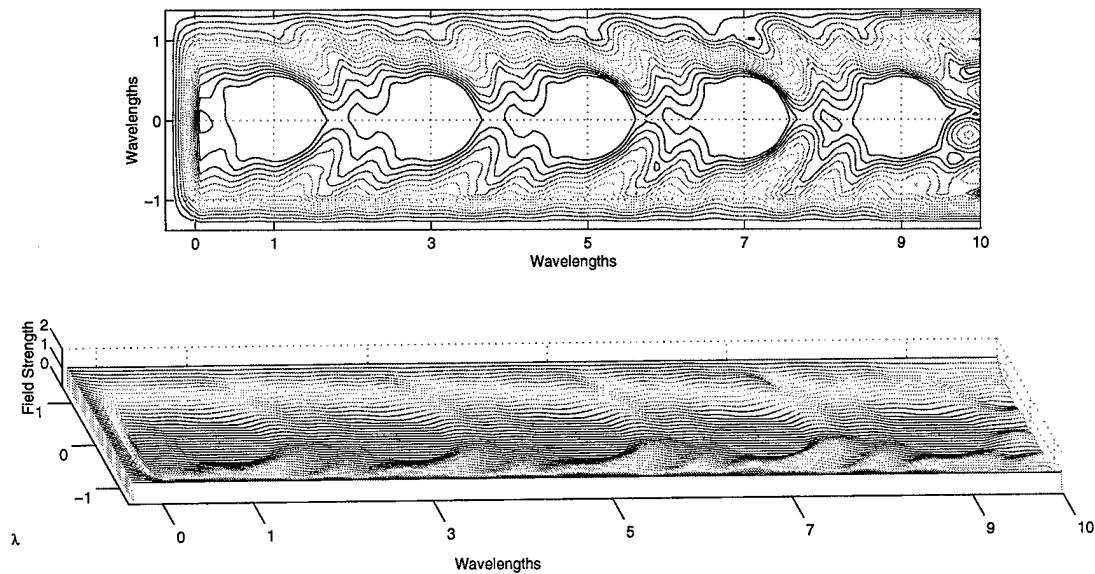
Figure A.22   Contour Map and Three-Dimensional Map of the Total Fields of a $1 - \lambda$ Diameter, 5-Cylinder Semi-Infinite Periodic Array at 10° Incidence.
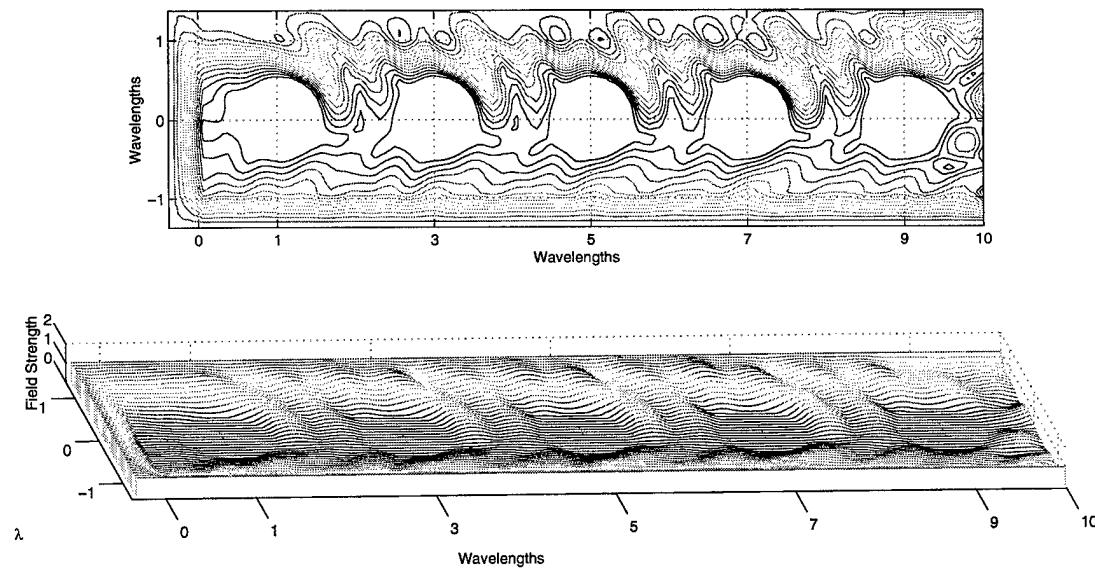
Figure A.23   Contour Map and Three-Dimensional Map of the Total Fields of a $1 - \lambda$ Diameter, 5-Cylinder Semi-Infinite Periodic Array at 15° Incidence.
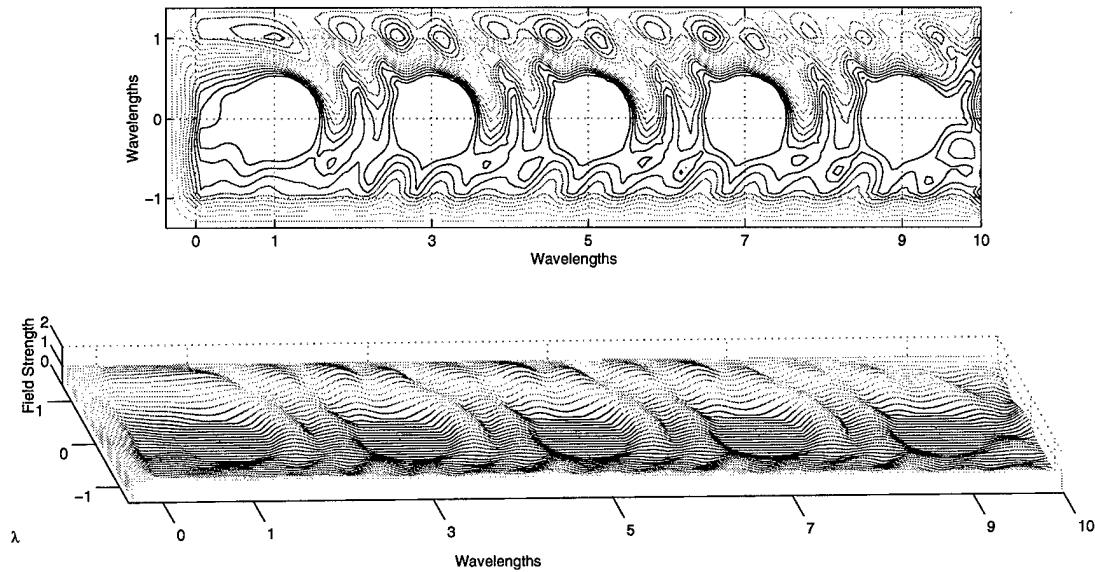
Figure A.24   Contour Map and Three-Dimensional Map of the Total Fields of a $1 - \lambda$ Diameter, 5-Cylinder Semi-Infinite Periodic Array at 20° Incidence.
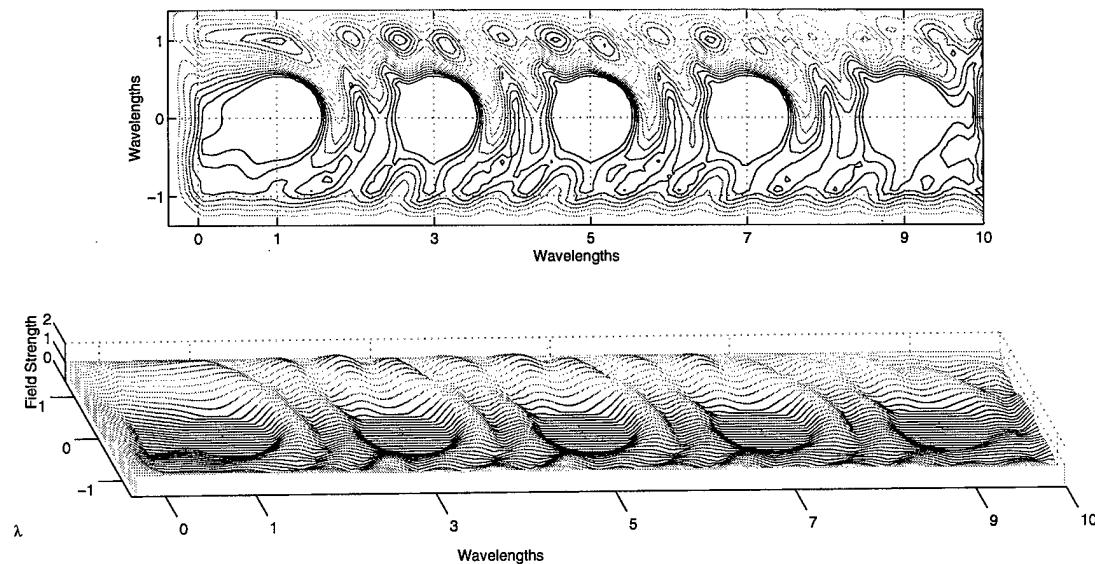

Figure A.25   Contour Map and Three-Dimensional Map of the Total Fields of a $1 - \lambda$ Diameter, 5-Cylinder Semi-Infinite Periodic Array at 25° Incidence.
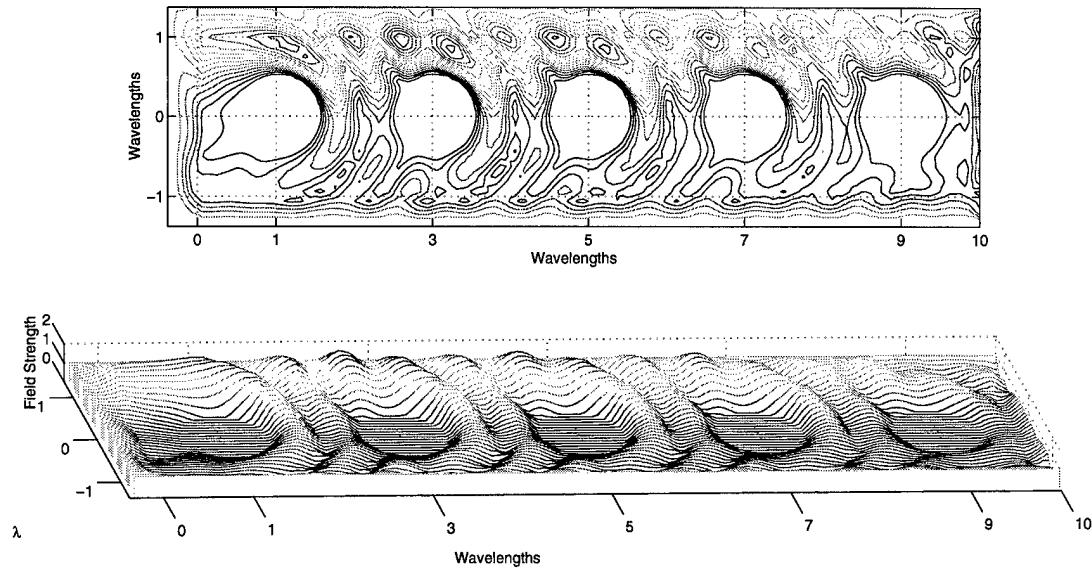
Figure A.26   Contour Map and Three-Dimensional Map of the Total Fields of a $1 - \lambda$ Diameter, 5-Cylinder Semi-Infinite Periodic Array at 30° Incidence.
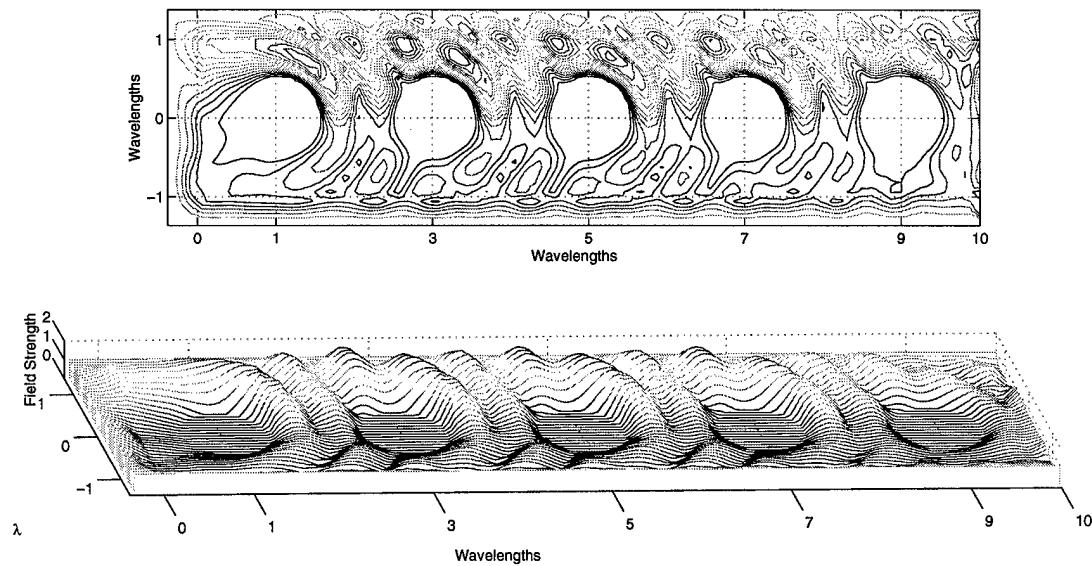

Figure A.27   Contour Map and Three-Dimensional Map of the Total Fields of a $1 - \lambda$ Diameter, 5-Cylinder Semi-Infinite Periodic Array at 35° Incidence.
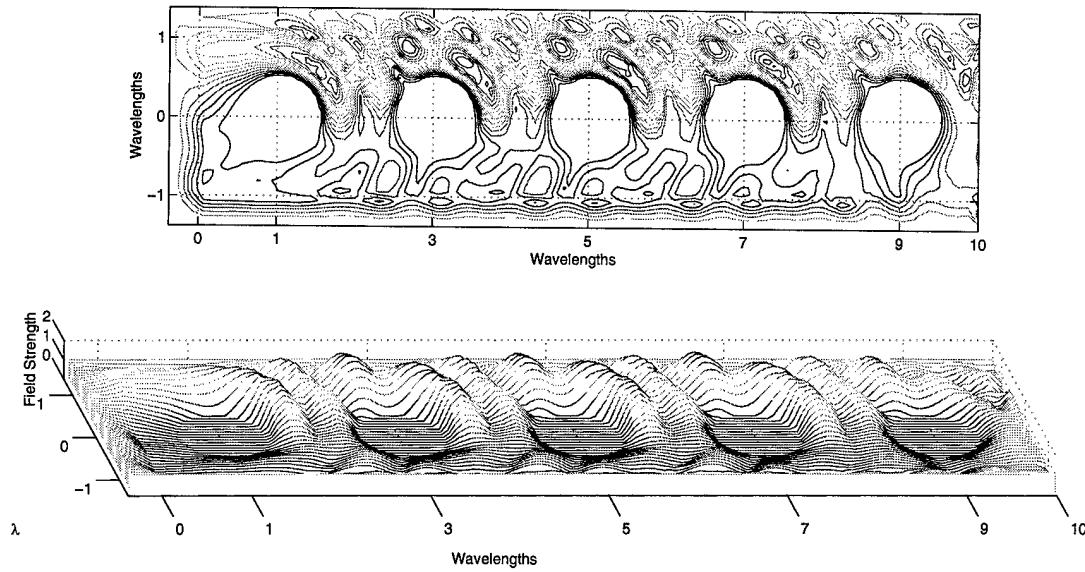
Figure A.28   Contour Map and Three-Dimensional Map of the Total Fields of a $1 - \lambda$ Diameter, 5-Cylinder Semi-Infinite Periodic Array at 40° Incidence.
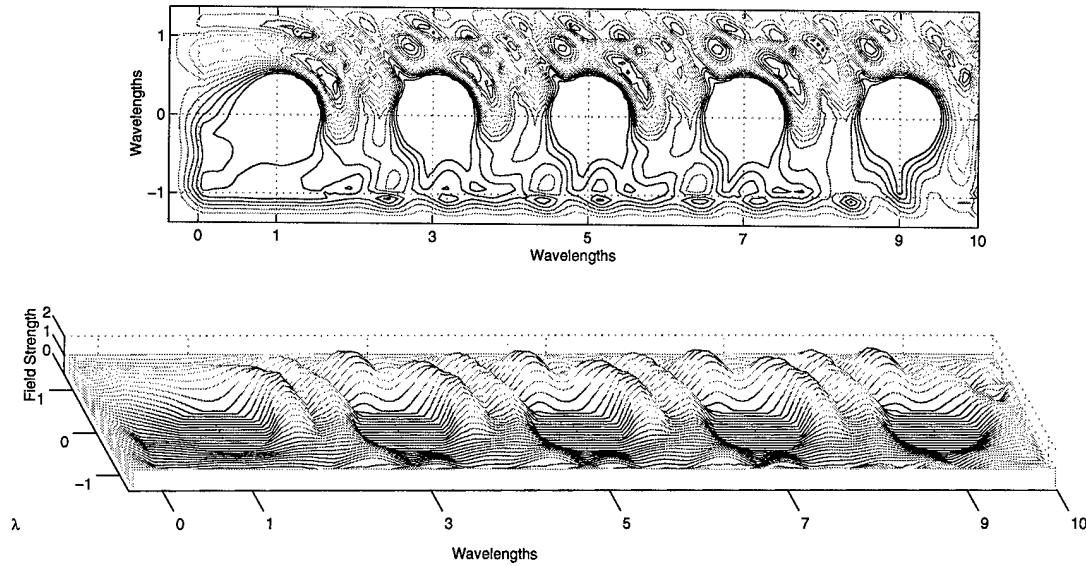
Figure A.29   Contour Map and Three-Dimensional Map of the Total Fields of a $1 - \lambda$ Diameter, 5-Cylinder Semi-Infinite Periodic Array at 45° Incidence.
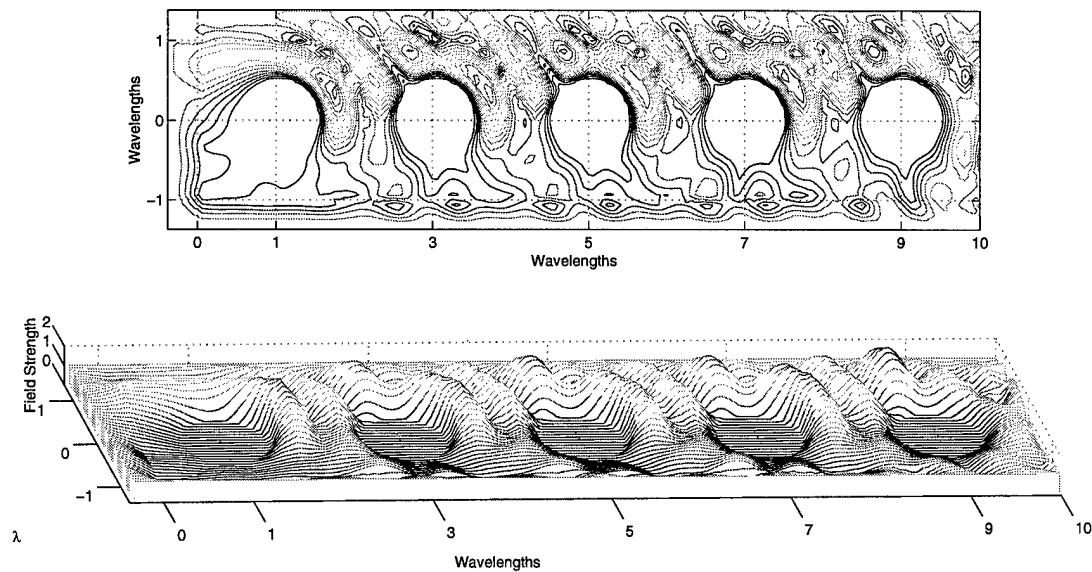
Figure A.30   Contour Map and Three-Dimensional Map of the Total Fields of a $1 - \lambda$ Diameter, 5-Cylinder Semi-Infinite Periodic Array at 50° Incidence.
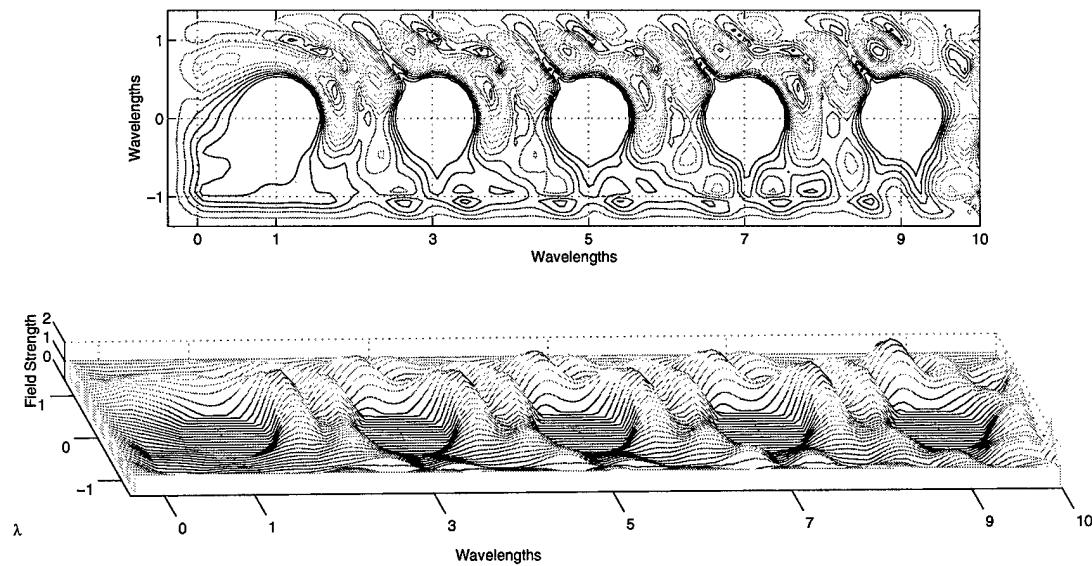
Figure A.31   Contour Map and Three-Dimensional Map of the Total Fields of a $1 - \lambda$ Diameter, 5-Cylinder Semi-Infinite Periodic Array at 55° Incidence.
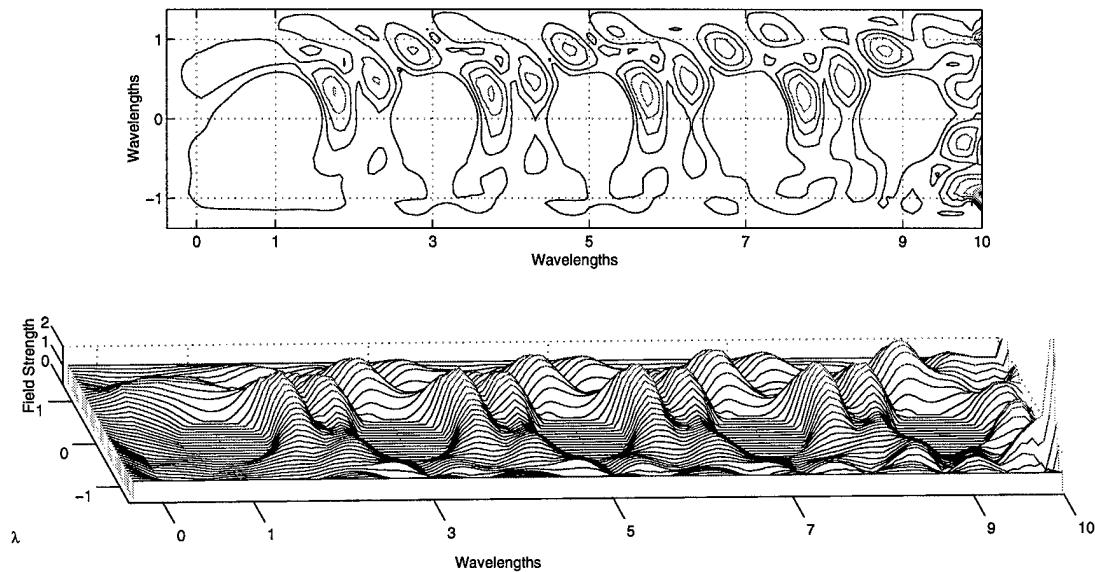
Figure A.32   Contour Map and Three-Dimensional Map of the Total Fields of a $1 - \lambda$
Diameter, 5-Cylinder Semi-Infinite Periodic Array at 60° Incidence.
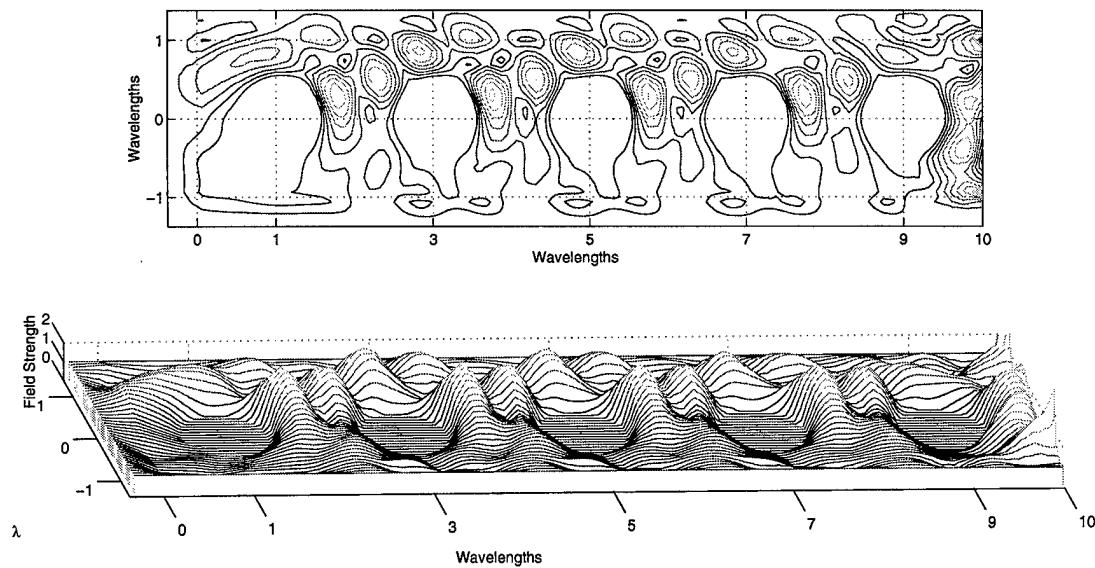
Figure A.33   Contour Map and Three-Dimensional Map of the Total Fields of a $1 - \lambda$
Diameter, 5-Cylinder Semi-Infinite Periodic Array at 65° Incidence.
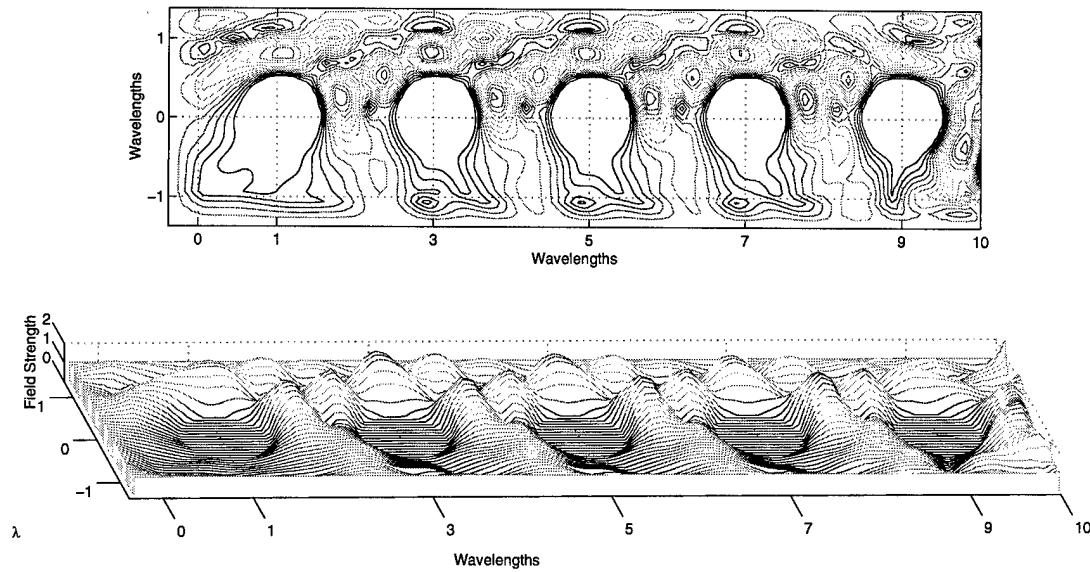
Figure A.34   Contour Map and Three-Dimensional Map of the Total Fields of a $1 - \lambda$ Diameter, 5-Cylinder Semi-Infinite Periodic Array at 70° Incidence.
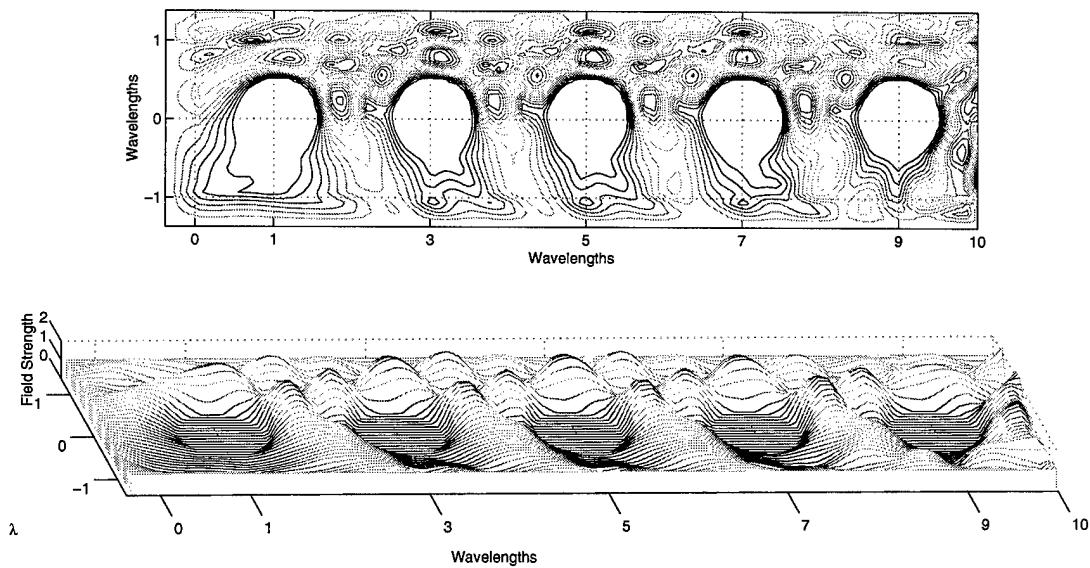
Figure A.35   Contour Map and Three-Dimensional Map of the Total Fields of a $1 - \lambda$ Diameter, 5-Cylinder Semi-Infinite Periodic Array at 75° Incidence.
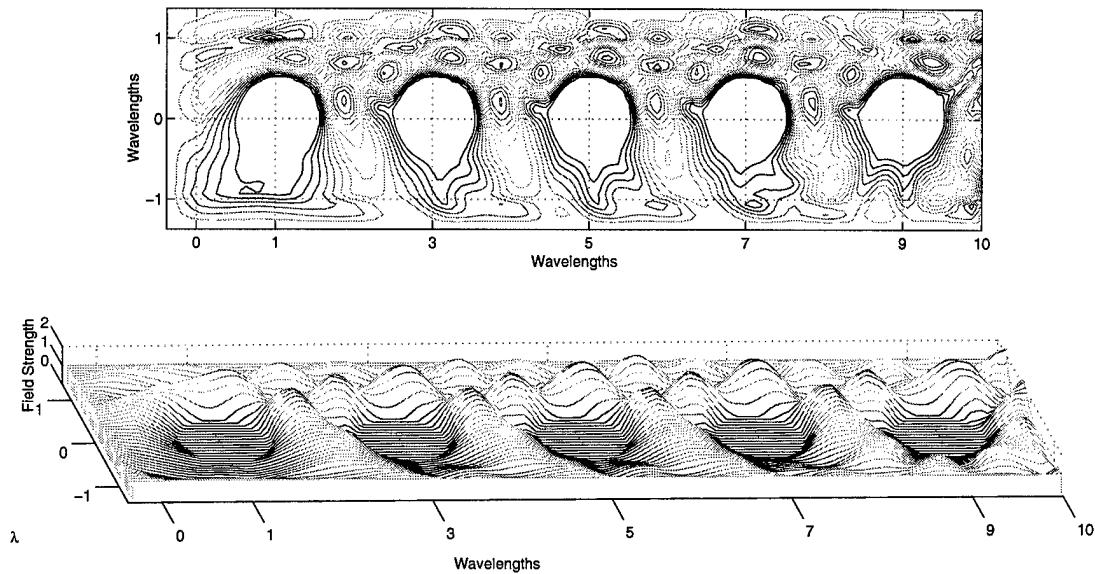
Figure A.36   Contour Map and Three-Dimensional Map of the Total Fields of a $1 - \lambda$ Diameter, 5-Cylinder Semi-Infinite Periodic Array at 80° Incidence.
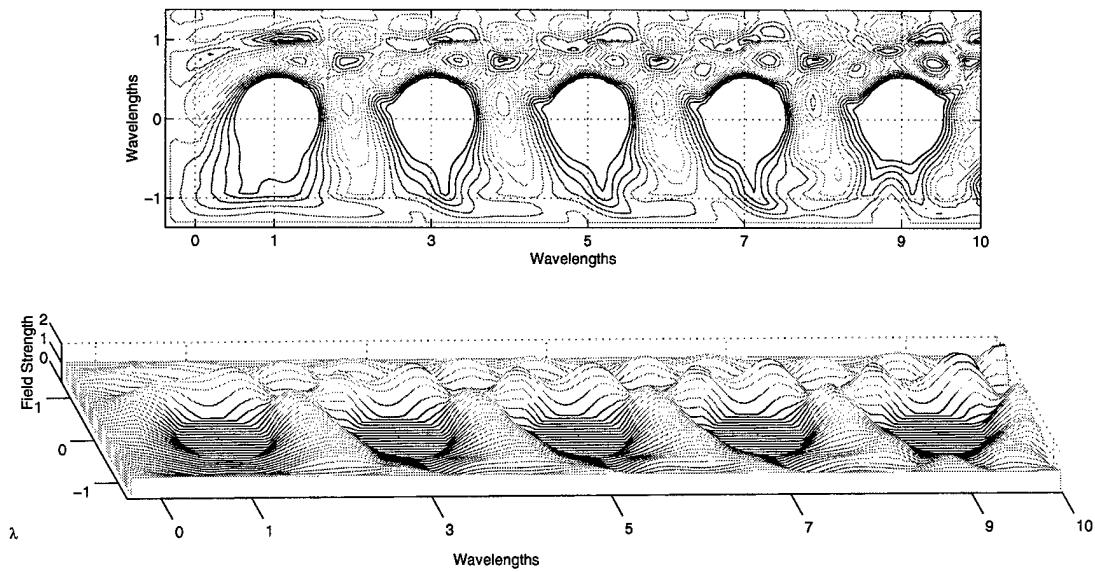

Figure A.37   Contour Map and Three-Dimensional Map of the Total Fields of a $1 - \lambda$ Diameter, 5-Cylinder Semi-Infinite Periodic Array at 85° Incidence.
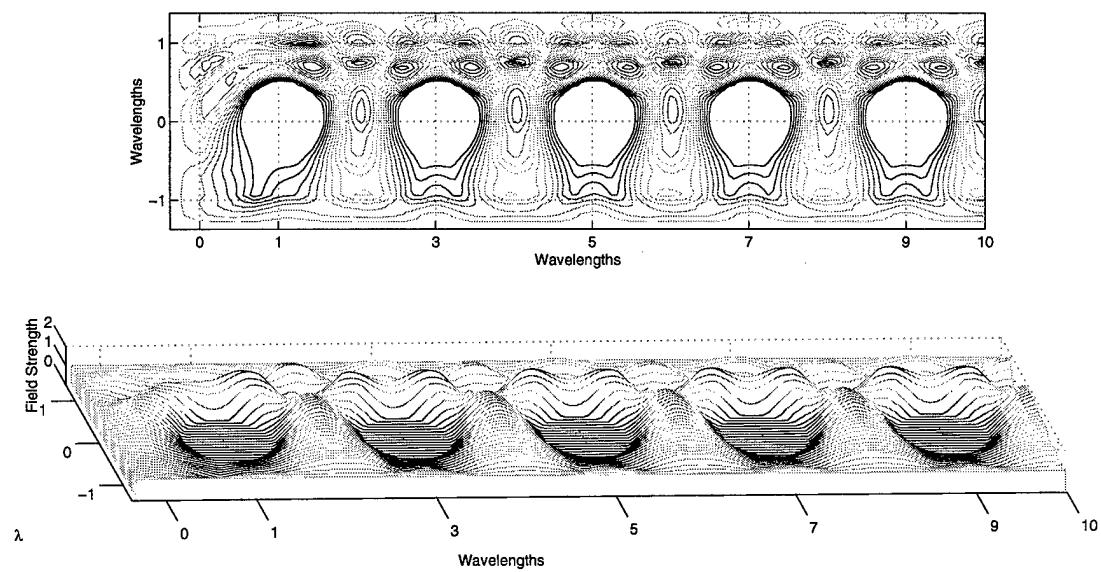
Figure A.38   Contour Map and Three-Dimensional Map of the Total Fields of a $1 - \lambda$ Diameter, 5-Cylinder Semi-Infinite Periodic Array at 90° Incidence.

## A.3 Field Plots for the Five-Cylinder Finite Periodic Structure
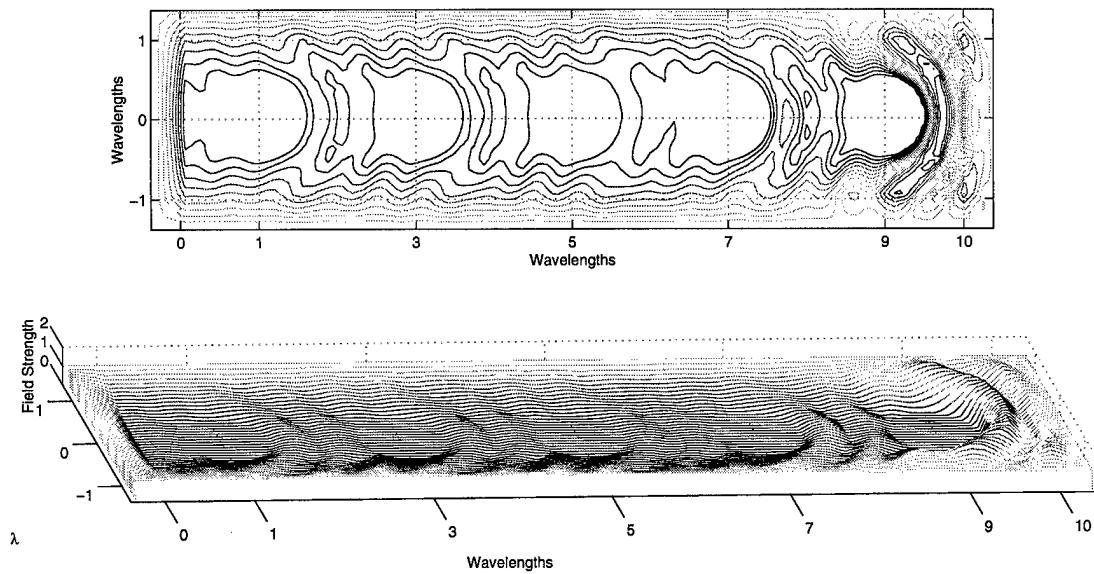
Figure A.39   Contour Map and Three-Dimensional Map of the Total Fields of a $1 - \lambda$ Diameter, 5-Cylinder Finite Periodic Array at 0° Incidence.
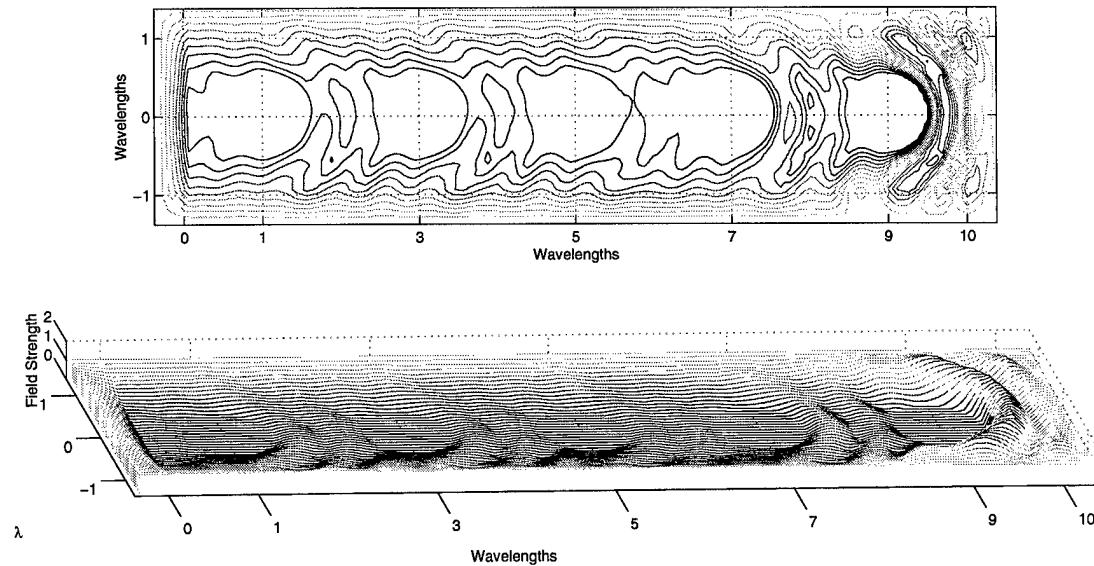
Figure A.40   Contour Map and Three-Dimensional Map of the Total Fields of a $1 - \lambda$ Diameter, 5-Cylinder Finite Periodic Array at 5° Incidence.
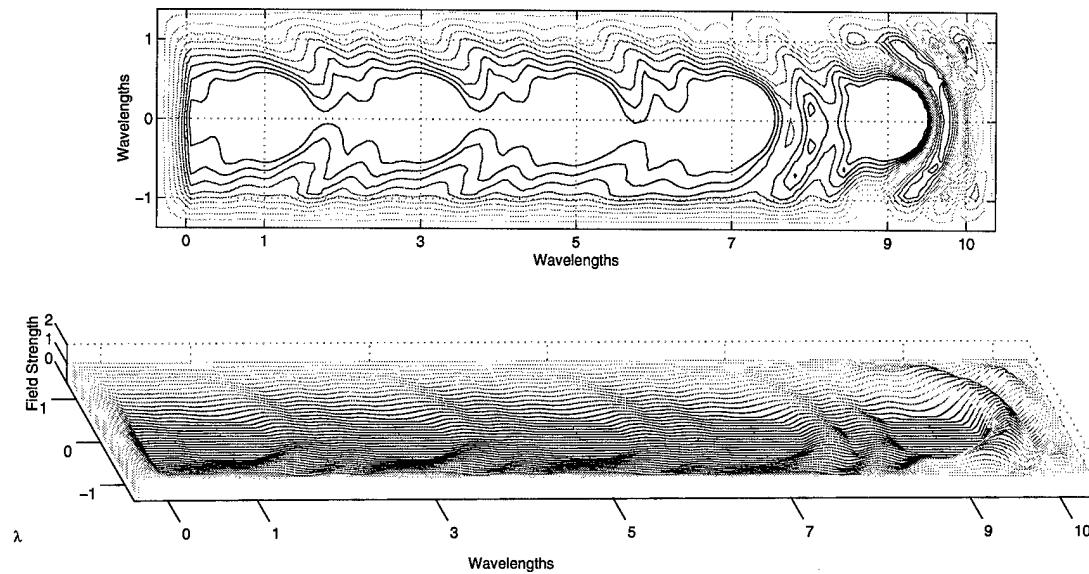
Figure A.41   Contour Map and Three-Dimensional Map of the Total Fields of a $1 - \lambda$ Diameter, 5-Cylinder Finite Periodic Array at 10° Incidence.
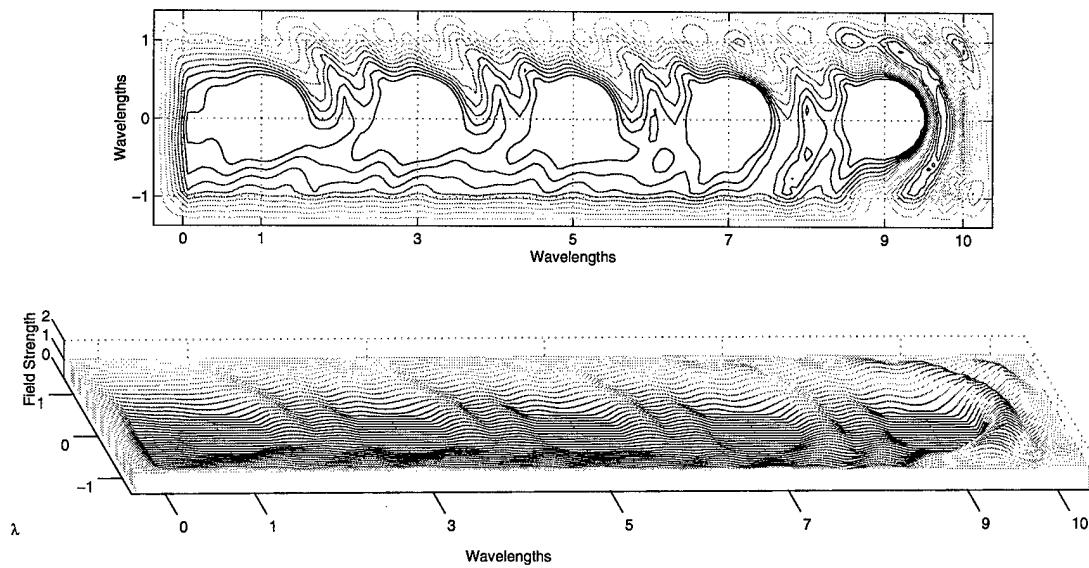

Figure A.42   Contour Map and Three-Dimensional Map of the Total Fields of a $1 - \lambda$ Diameter, 5-Cylinder Finite Periodic Array at 15° Incidence.
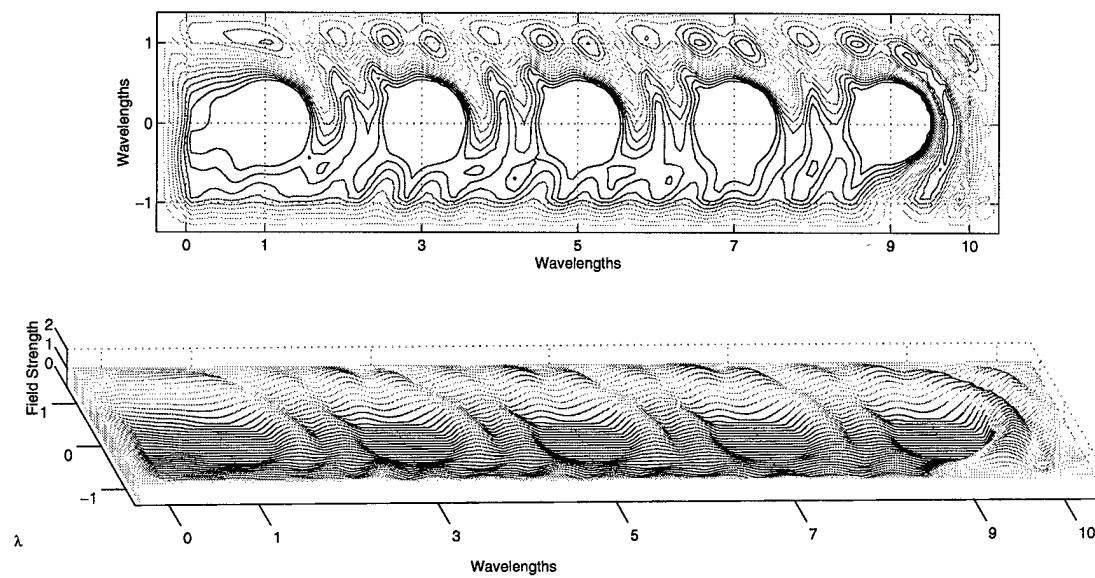
Figure A.43   Contour Map and Three-Dimensional Map of the Total Fields of a $1 - \lambda$ Diameter, 5-Cylinder Finite Periodic Array at 20° Incidence.
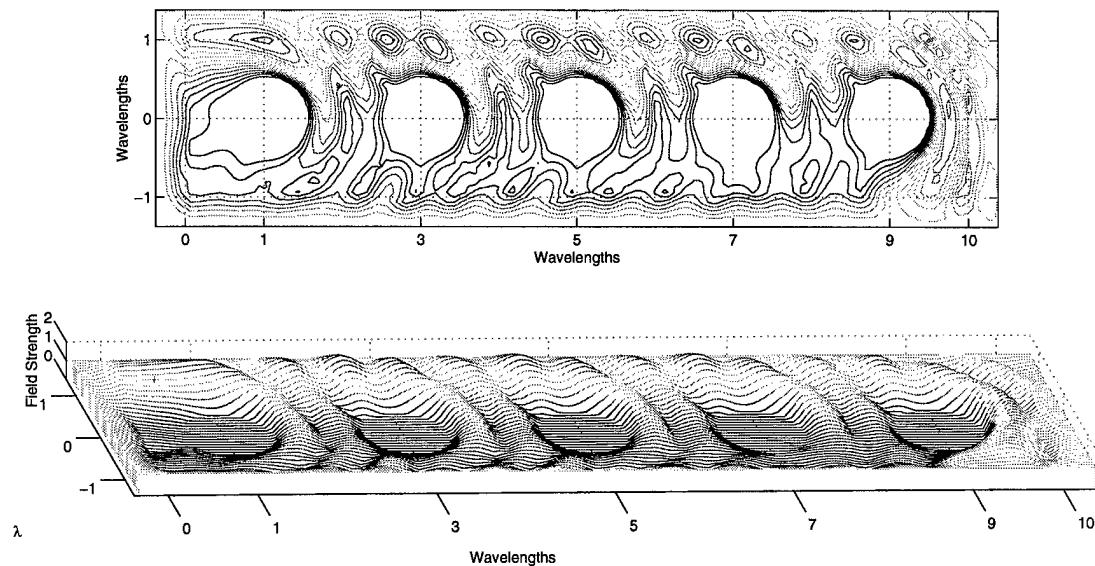
Figure A.44   Contour Map and Three-Dimensional Map of the Total Fields of a $1 - \lambda$ Diameter, 5-Cylinder Finite Periodic Array at 25° Incidence.
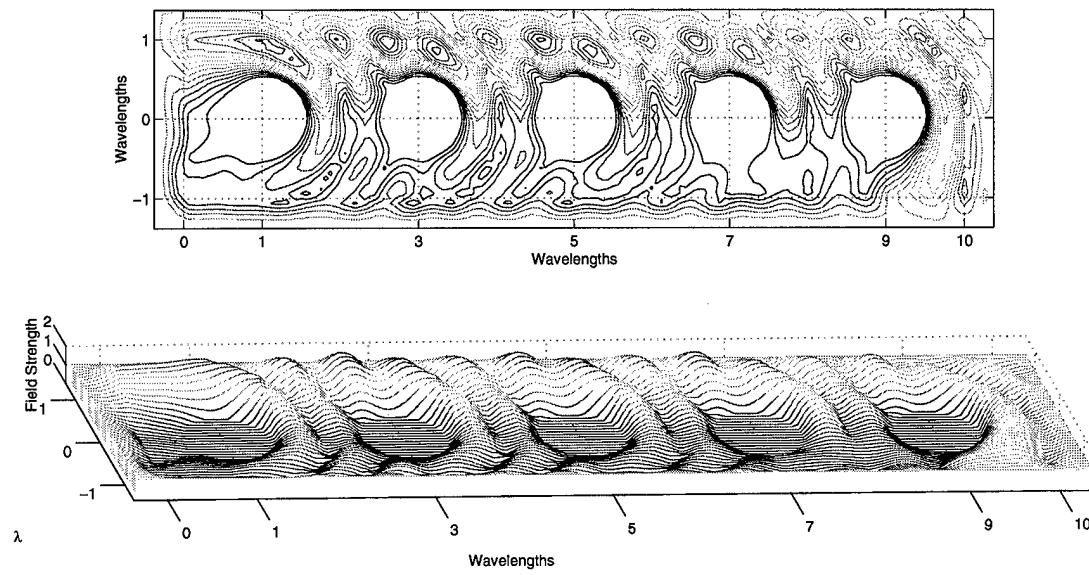
Figure A.45   Contour Map and Three-Dimensional Map of the Total Fields of a $1 - \lambda$ Diameter, 5-Cylinder Finite Periodic Array at 30° Incidence.
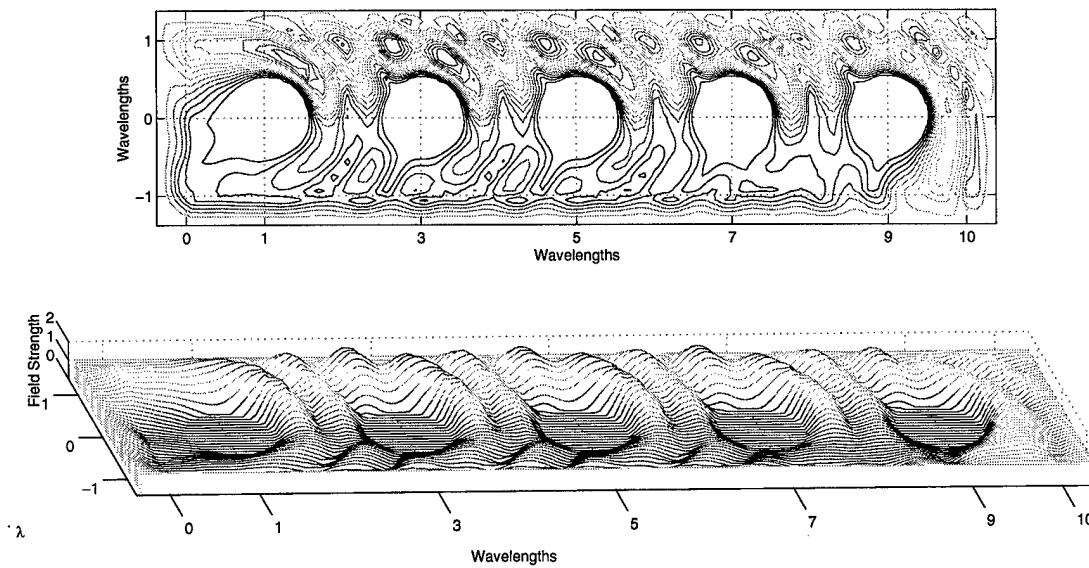

Figure A.46   Contour Map and Three-Dimensional Map of the Total Fields of a $1 - \lambda$ Diameter, 5-Cylinder Finite Periodic Array at 35° Incidence.
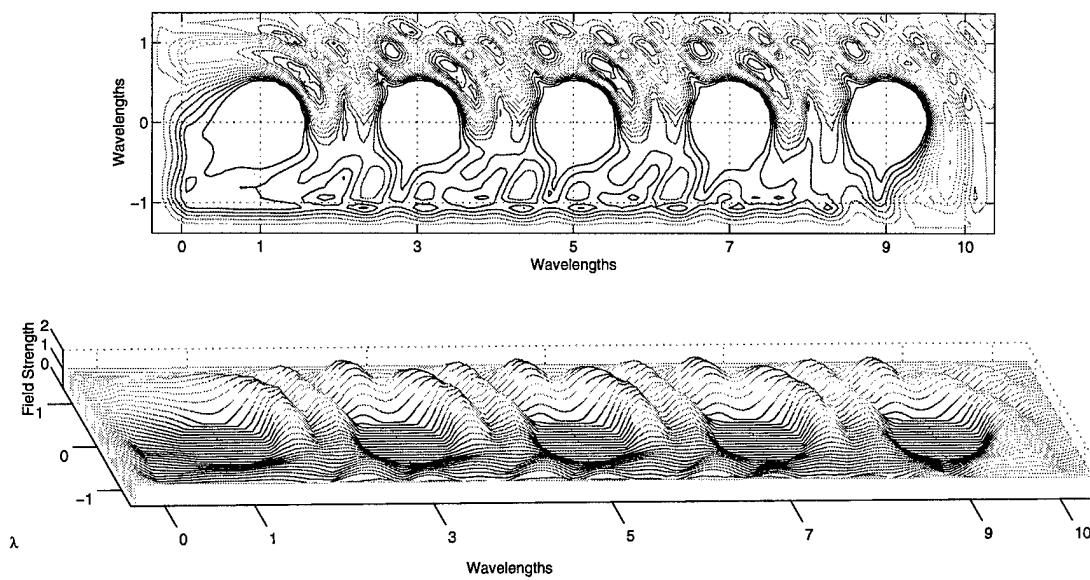
Figure A.47   Contour Map and Three-Dimensional Map of the Total Fields of a $1 - \lambda$ Diameter, 5-Cylinder Finite Periodic Array at 40° Incidence.
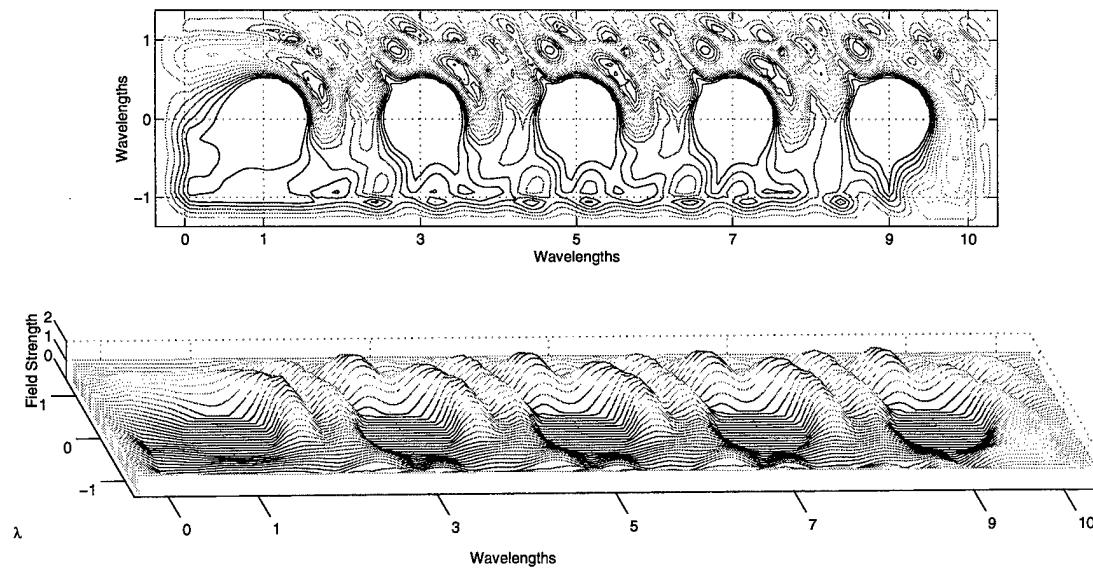
Figure A.48   Contour Map and Three-Dimensional Map of the Total Fields of a $1 - \lambda$ Diameter, 5-Cylinder Finite Periodic Array at 45° Incidence.
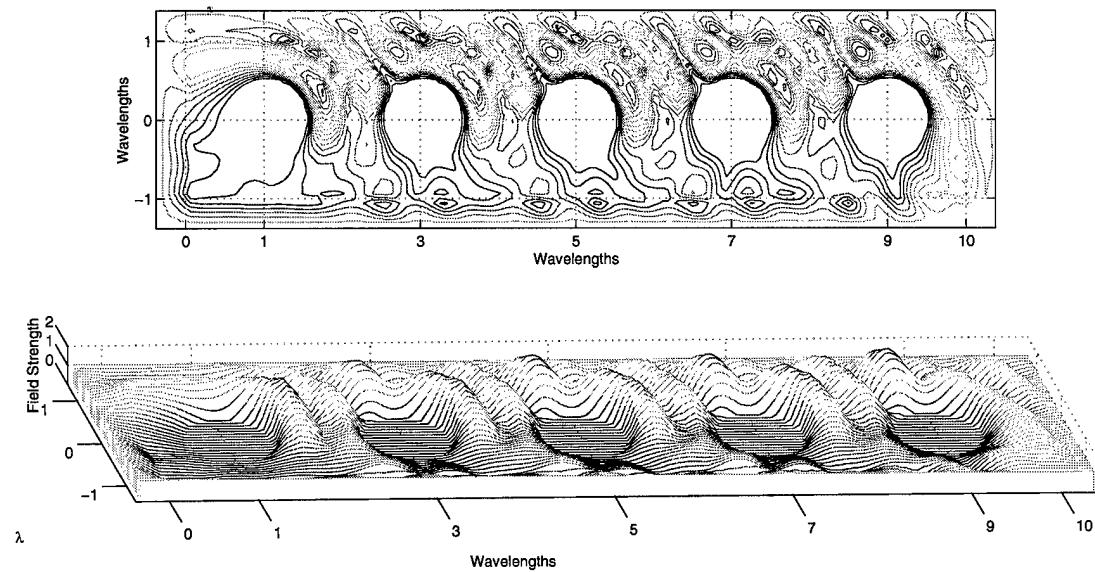
Figure A.49   Contour Map and Three-Dimensional Map of the Total Fields of a $1 - \lambda$ Diameter, 5-Cylinder Finite Periodic Array at 50° Incidence.
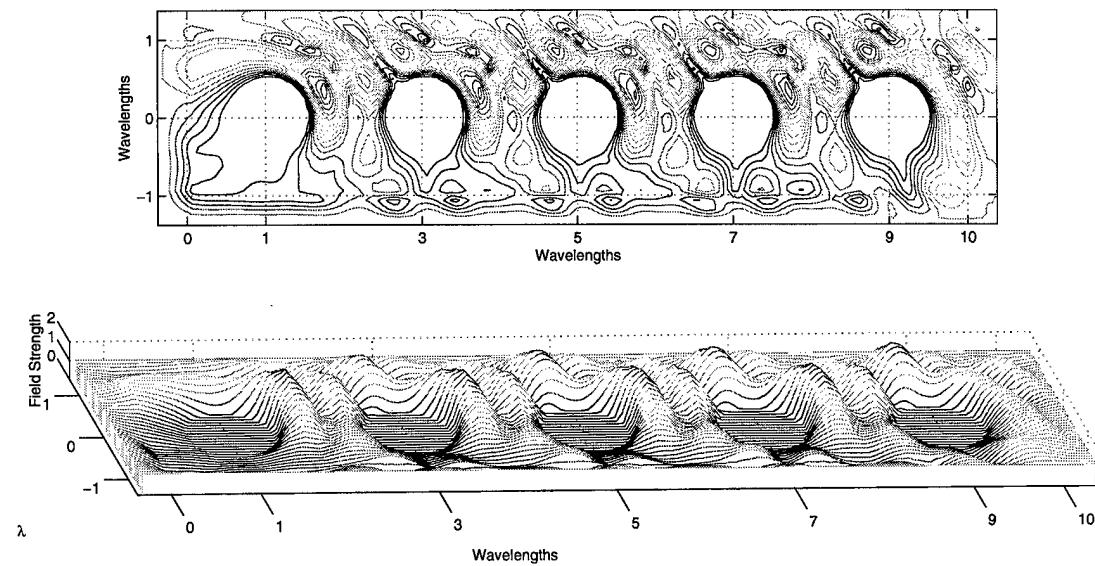

Figure A.50   Contour Map and Three-Dimensional Map of the Total Fields of a $1 - \lambda$ Diameter, 5-Cylinder Finite Periodic Array at 55° Incidence.
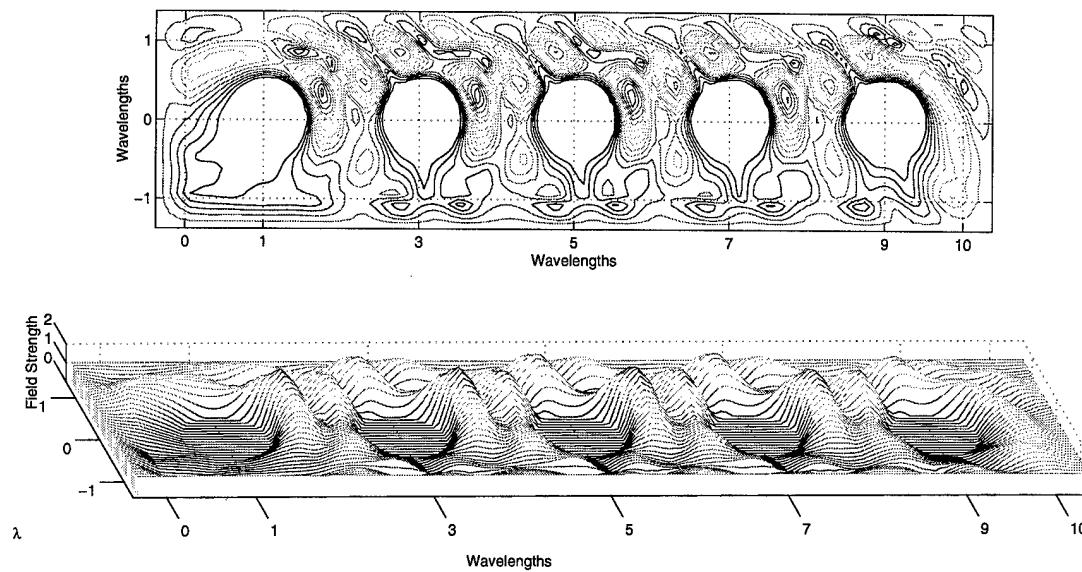
Figure A.51   Contour Map and Three-Dimensional Map of the Total Fields of a $1 - \lambda$ Diameter, 5-Cylinder Finite Periodic Array at 60° Incidence.
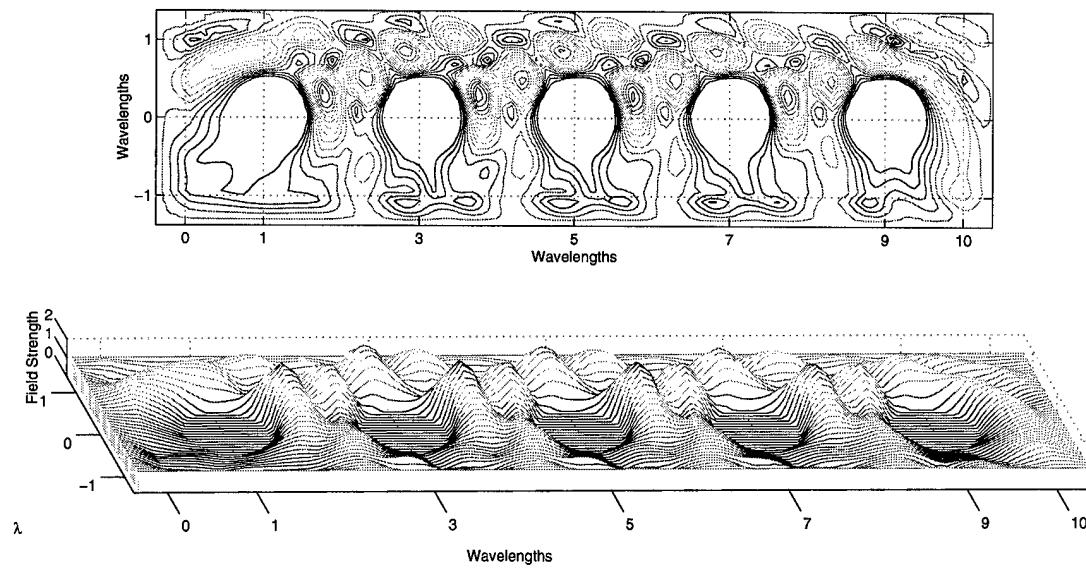
Figure A.52   Contour Map and Three-Dimensional Map of the Total Fields of a $1 - \lambda$ Diameter, 5-Cylinder Finite Periodic Array at 65° Incidence.
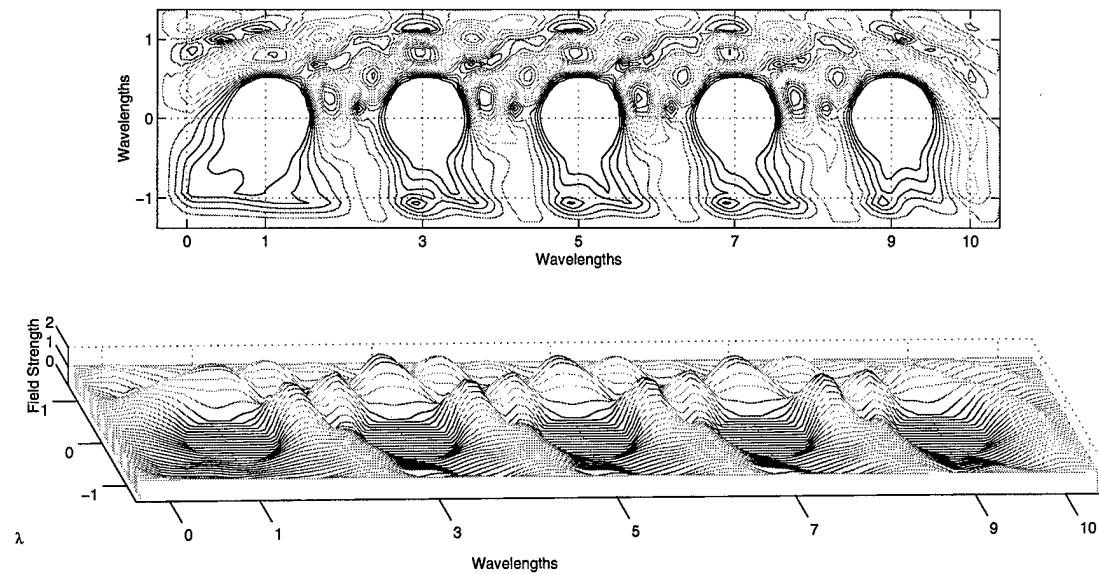
Figure A.53   Contour Map and Three-Dimensional Map of the Total Fields of a $1 - \lambda$ Diameter, 5-Cylinder Finite Periodic Array at 70° Incidence.
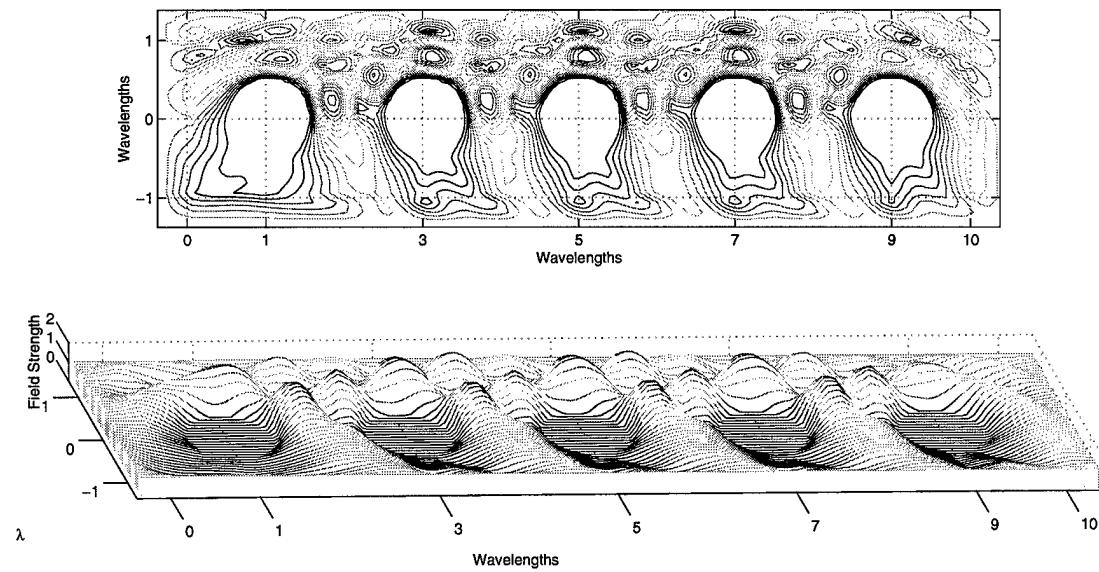

Figure A.54   Contour Map and Three-Dimensional Map of the Total Fields of a $1 - \lambda$ Diameter, 5-Cylinder Finite Periodic Array at 75° Incidence.
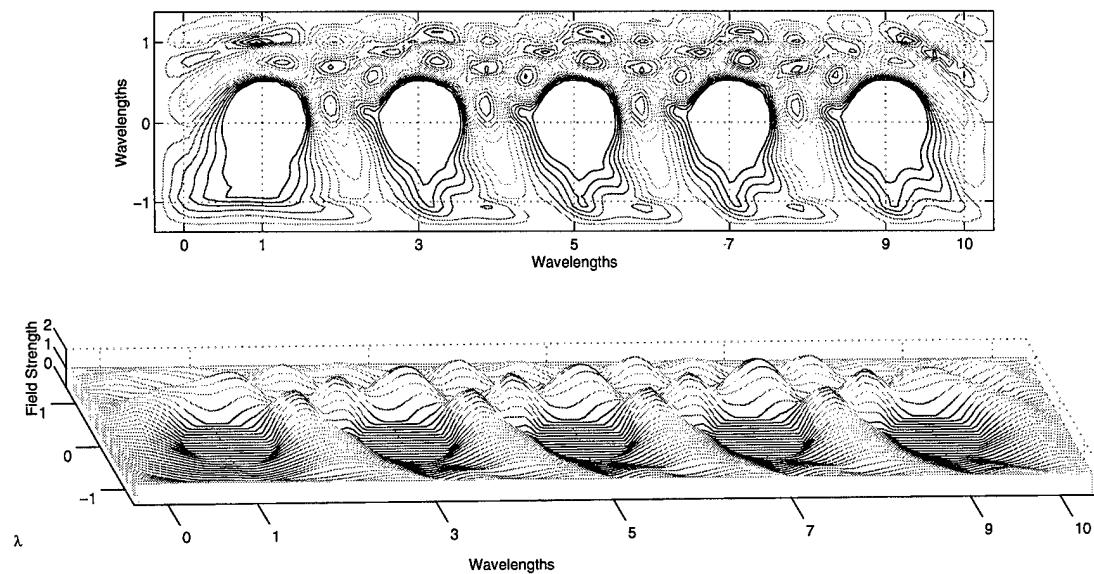
Figure A.55   Contour Map and Three-Dimensional Map of the Total Fields of a $1 - \lambda$ Diameter, 5-Cylinder Finite Periodic Array at 80° Incidence.
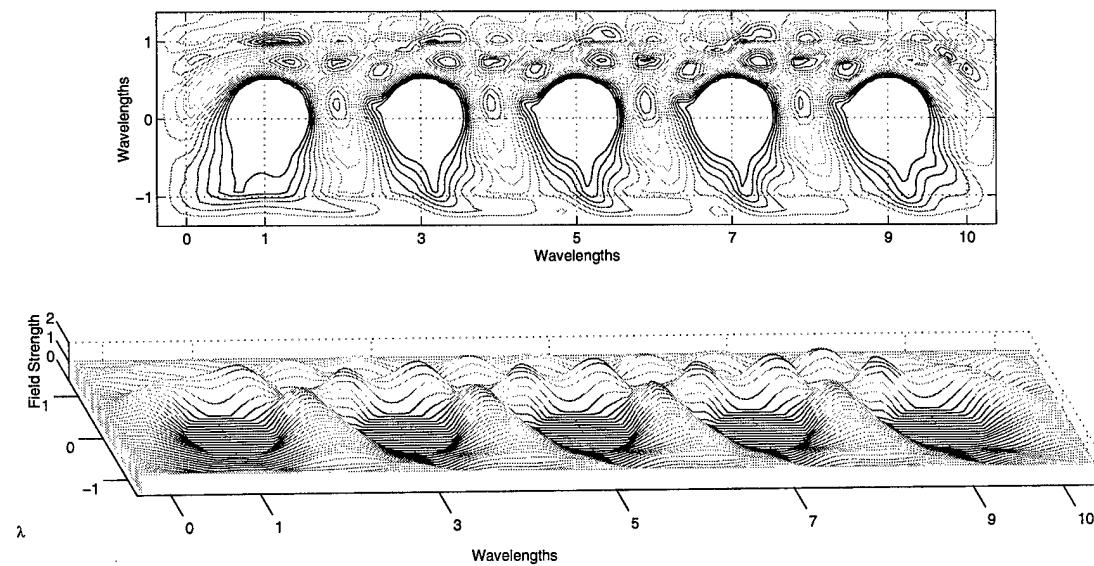

Figure A.56   Contour Map and Three-Dimensional Map of the Total Fields of a $1 - \lambda$ Diameter, 5-Cylinder Finite Periodic Array at 85° Incidence.
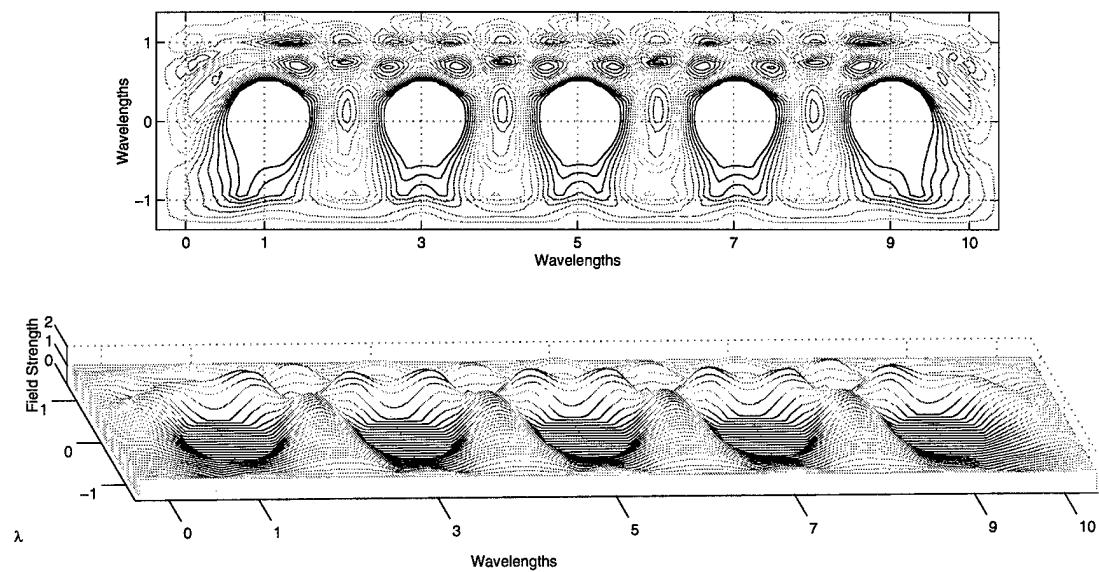
Figure A.57   Contour Map and Three-Dimensional Map of the Total Fields of a $1 - \lambda$ Diameter, 5-Cylinder Finite Periodic Array at 90° Incidence.

B.1   Finite Element Method Software Modification

```
      subroutine EMBEDB (UPLO,MAXNODE,MAXNXE,MAXELE,MAXDIEL,MAXBAND,
     &                   ELE,xy,NLAB,ELAB,LPMAX,LPMAY,LPMAXY,APMA,LDIR,
     &                   DIRC,COEFFP,COEFFQ,nele,nnode,A,B,ku,
     &                   kl,kd,phi,Ndie)
C
C  =======================================================================
C     EMBEDS LOCAL MATRIX SL OF THE ELEMENT IE INTO THE GLOBAL MATRIX
C     A OR INTO THE RIGHT HAND SIDE, AS APPROPRIATE. THIS EXPLOITS
C     PMA TYPE ABC.
C     DUMMY ARGUMENTS ARE COMMENTED IN THE CALLING MODULE
C     QUICK_FEM (C) 1997 PELOSI - COCCIOLI - SELLERI
C     This code allows the inclusion of a periodic boundary on one side
C     and PMA layers on the other three sides.  This enables computation
C     of a HALF-INFINITE periodic cylinders.
C
C     Modified to accommodate the Right Hand Side Boundary not enclosed
C     by PMA.  Also hard coded to run on a specific geometry:
C             --> fivepecyl_ren.fem
C
C     Modification only occurs in the subroutine:  EMBEDB
C
C
C     PERRY N. VILLANUEVA
C     Air Force Institute of Technology
C     6 January 1999
C
C  =======================================================================
C     [IN]
      IMPLICIT NONE
      CHARACTER*1 UPLO      !'U' Stores only Upper Triangle
                            !'L' Stores only Lower Triangle
                            !'T' Stores all matrix
      integer MAXNODE,MAXNXE,MAXELE,MAXDIEL,MAXBAND,ELE(0:MAXNXE,MAXELE)
      integer NLAB(MAXNODE),ELAB(MAXELE)
      integer LPMAX,LPMAY,LPMAXY ! Label of elements on the PMA
      integer LDIR          ! Label of nodes on Dirichlet boundary
      integer DIRC          ! Coefficient of scattered field
                            ! at Dirichlet boundary (Uscat=DIRC*Uinc)
```

```fortran
      complex CoeffP(MAXDIEL),CoeffQ(MAXDIEL),APMA,AA,BB,CC
      integer Nele,NNode,Ndie,ku,kl,kd,ie
      real    xy(2,MAXNODE),SXE(8,8),SYE(8,8),TE(8,8),phi

C     [IN/OUT]
      complex A(3*MAXBAND+1,MAXNODE)        ! Left hand side matrix
      complex B(MAXNODE)                    ! Right Hand side vector

C     [LOCAL]
      integer I,J                           ! indices
      integer IROW,ICOL                     ! indexes to entries global FEM Matrix
      complex caux
      real    PI,KO,KO2

C     [EXTERNAL FUNCTIONS]
      complex CBGET
      complex EINC

      parameter (PI = 3.141592653589793238)
      KO = 2. * PI
      KO2= KO * KO

      do ie=1,nele

         call ELEAMAT(MAXNODE,MAXNXE,MAXELE,XY,ELE,IE,SXE,SYE,8,TE,8)

         DO I = 1,3
            IROW = ELE(I,IE)
            IF (NLAB(IROW) .EQ. LDIR) THEN
C     ---------- ENFORCE DIRICHLET BOUNDARY CONDITIONS
               call CBPUT((1.,0.),
     &                    A,IROW,IROW,ku,kl,kd,3*MAXBAND+1,NNODE,'U')
               if (ELAB(ie).ne.LPMAX.and.ELAB(ie).ne.LPMAY.and.
     &             ELAB(ie).ne.LPMAXY) then
                  B(IROW) = DIRC * EINC(Xy(1,IROW),xY(2,IROW),PHI)
               endif
            ELSE
               DO J = 1,3
                  ICOL = ELE(J,IE)
                  IF (ELAB(IE).le.NDIE) THEN

C     ----------AUGMENT THE GLOBAL MATRIX A
C
C     ---------->NODES ARE IN AIR (INTERIOR)

                     caux = CBGET(A,irow,icol,ku,kl,kd,3*MAXBAND+1,
     &                            NNODE,'U')
```

```fortran
            if ( (icol.eq.1895) .or. (icol.eq.1897) .or.
     &           (icol.eq.1911) .or. (icol.eq.1913) .or.
     &           (icol.eq.1926) .or. (icol.eq.1939) .or.
     &           (icol.eq.1952) .or. (icol.eq.1966) .or.
     &           (icol.eq.1981) .or. (icol.eq.1995) .or.
     &           (icol.eq.2010) .or. (icol.eq.2026) .or.
     &           (icol.eq.2042) .or. (icol.eq.2057) .or.
     &           (icol.eq.2073) .or. (icol.eq.2077) .or.
     &           (icol.eq.2078) ) then

                caux = caux + Coeffp(ELAB(IE))
     &                  * (SXE(i,j) + SYE(i,j))
     &                  * exp(-(0., 1.)*k0*cos(phi))
     &                  - k02 * COEFFQ(ELAB(IE)) * TE(i,j)
            else
                caux = caux + Coeffp(ELAB(IE))
     &                  * (SXE(i,j) + SYE(i,j))
     &                  - k02 * COEFFQ(ELAB(IE)) * TE(i,j)
            endif
            call CBPUT(caux,
     &                  A,IROW,ICOL,ku,kl,kd,3*MAXBAND+1,NNODE,'U')

C       ----------AUGMENT THE RIGHT HAND SIDE


            if ( (icol.eq.1895) .or. (icol.eq.1897) .or.
     &           (icol.eq.1911) .or. (icol.eq.1913) .or.
     &           (icol.eq.1926) .or. (icol.eq.1939) .or.
     &           (icol.eq.1952) .or. (icol.eq.1966) .or.
     &           (icol.eq.1981) .or. (icol.eq.1995) .or.
     &           (icol.eq.2010) .or. (icol.eq.2026) .or.
     &           (icol.eq.2042) .or. (icol.eq.2057) .or.
     &           (icol.eq.2073) .or. (icol.eq.2077) .or.
     &           (icol.eq.2078) ) then

                B(IROW) = B(IROW) - (coeffp(ELAB(IE))*
     &                  (SXE(i,j) + SYE(i,j))
     &                  *exp(-(0., 1.)*k0*cos(phi))
     &                  - K02*COEFFQ(ELAB(IE)) *
     &                  TE(I,J)) * EINC(Xy(1,ICOL),xY(2,ICOL),PHI)
            else
                B(IROW) = B(IROW) - (coeffp(ELAB(IE))*
     &                  (SXE(i,j) + SYE(i,j)) - K02*
     &                  COEFFQ(ELAB(IE)) *
     &                  TE(I,J)) * EINC(Xy(1,ICOL),xY(2,ICOL),PHI)
```

```
                 endif
             ELSE

C      ----------AUGMENT THE GLOBAL MATRIX A
C
C      ----------> NODES ARE IN PMA

             if(ELAB(IE).EQ.LPMAX) then
               AA=APMA
               BB=1./APMA
               CC=APMA
             else if(ELAB(IE).EQ.LPMAY) then
               AA=1./APMA
               BB=APMA
               CC=APMA
             else
               AA=1.
               BB=1.
               CC=APMA*APMA
             endif
             caux = CBGET(A,irow,icol,ku,kl,kd,3*MAXBAND+1,
     &                  NNODE,'U')
             if ( (icol.eq.1880) .or. (icol.eq.1894) .or.
     &          (icol.eq.2082) .or. (icol.eq.2085) ) then
                caux = caux +
     &                (SXE(i,j)/BB + SYE(i,j)/AA)
     &                * exp(-(0., 1.)*k0*cos(phi))
     &                - k02 * CC * TE(i,j)

             else
                caux = caux +
     &                SXE(i,j)/BB +
     &                SYE(i,j)/AA +
     &                - k02 * CC * TE(i,j)
             endif

             call CBPUT(caux,
     &                A,IROW,ICOL,ku,kl,kd,3*MAXBAND+1,NNODE,'U')


             if (nlab(ele(i,ie)).eq.0) then

                if ( (icol.eq.1880) .or. (icol.eq.1894) .or.
     &             (icol.eq.2082) .or. (icol.eq.2085) ) then

                   B(IROW) = B(IROW) -
     &                     ((SXE(i,j) + SYE(i,j))
```

```
&                                 *exp(-(0., 1.)*k0*cos(phi)))
&                                 - K02* TE(I,J))
&                                 * EINC(Xy(1,ICOL),xY(2,ICOL),PHI)
                     else
                         B(IROW) = B(IROW) -
&                                 (SXE(i,j) + SYE(i,j) - K02* TE(I,J))
&                                 * EINC(Xy(1,ICOL),xY(2,ICOL),PHI)
                     endif
                 endif
              ENDIF
           ENDDO
        ENDIF
     ENDDO
  enddo

  RETURN
  END
```

```
fivepecyl_open.fem
133 33
 1 3    1    2    3   15   23   22   21   14   55
 2 3  101  102  103  115  123  122  121  114   55
 3 3    3    4    5   16   25   24   23   15    5
 4 3    5    6    7   17   27   26   25   16    5
 5 3    7    8    9   18   29   28   27   17    5
 6 3    9   10   11   19   31   30   29   18    5
 7 3   11   12   13   20   33   32   31   19    5
 8 3   21   22   23   60  103  102  101   59   50
 9 3  103  104  105  116  125  124  123  115    5
10 3  105  106  107  117  127  126  125  116    5
11 3  107  108  109  118  129  128  127  117    5
12 3  109  110  111  119  131  130  129  118    5
13 3  111  112  113  120  133  132  131  119    5
14 3   23   24   25   35   46   45   44   34    1
15 3   25   63  105   92   78   62   46   35    1
16 3  105  104  103   91   76   77   78   92    1
17 3  103   60   23   34   44   61   76   91    1
18 3   25   26   27   37   49   48   47   36    1
19 3   27   66  107   94   81   65   49   37    1
20 3  107  106  105   93   79   80   81   94    1
21 3  105   63   25   36   47   64   79   93    1
22 3   27   28   29   39   52   51   50   38    1
23 3   29   69  109   96   84   68   52   39    1
24 3  109  108  107   95   82   83   84   96    1
25 3  107   66   27   38   50   67   82   95    1
26 3   29   30   31   41   55   54   53   40    1
27 3   31   72  111   98   87   71   55   41    1
28 3  111  110  109   97   85   86   87   98    1
29 3  109   69   29   40   53   70   85   97    1
30 3   31   32   33   43   58   57   56   42    1
31 3   33   75  113  100   90   74   58   43    1
32 3  113  112  111   99   88   89   90  100    1
33 3  111   72   31   42   56   73   88   99    1
 1 -5.375   -1.375  1
 2 -5.1875  -1.375   1
 3 -5.0   -1.375  1
 4 -4.0   -1.375  1
 5 -3.0   -1.375  1
 6 -2.0   -1.375  1
 7 -1.0   -1.375  1
```

```
 8   0.0   -1.375   1
 9   1.0   -1.375   1
10   2.0   -1.375   1
11   3.0   -1.375   1
12   4.0   -1.375   1
13   5.0   -1.375   1
14  -5.375  -1.1875  1
15  -5.0   -1.1875  0
16  -3.0   -1.1875  0
17  -1.0   -1.1875  0
18   1.0   -1.1875  0
19   3.0   -1.1875  0
20   5.0   -1.1875  0
21  -5.375  -1.0    1
22  -5.1875  -1.0   0
23  -5.0   -1.0    0
24  -4.0   -1.0    0
25  -3.0   -1.0    0
26  -2.0   -1.0    0
27  -1.0   -1.0    0
28   0.0   -1.0    0
29   1.0   -1.0    0
30   2.0   -1.0    0
31   3.0   -1.0    0
32   4.0   -1.0    0
33   5.0   -1.0    0
34  -4.65   -0.65   0
35  -3.35   -0.65   0
36  -2.65   -0.65   0
37  -1.35   -0.65   0
38  -0.65   -0.65   0
39   0.65   -0.65   0
40   1.35   -0.65   0
41   2.65   -0.65   0
42   3.35   -0.65   0
43   4.65   -0.65   0
44  -4.35355339059327373  -0.35355339059327373  1
45  -4.0   -0.5   1
46  -3.64644660940672627  -0.35355339059327373  1
47  -2.35355339059327373  -0.35355339059327373  1
48  -2.0   -0.5   1
49  -1.64644660940672627  -0.35355339059327373  1
50  -0.35355339059327373  -0.35355339059327373  1
51   0.0   -0.5   1
52   0.35355339059327373  -0.35355339059327373  1
53   1.64644660940672627  -0.35355339059327373  1
54   2.0   -0.5   1
```

```
55   2.35355339059327373  -0.35355339059327373  1
56   3.64644660940672627  -0.35355339059327373  1
57   4.0   -0.5   1
58   4.35355339059327373  -0.35355339059327373  1
59  -5.375   0.0   1
60  -5.0   0.0   0
61  -4.5   0.0   1
62  -3.5   0.0   1
63  -3.0   0.0   0
64  -2.5   0.0   1
65  -1.5   0.0   1
66  -1.0   0.0   0
67  -0.5   0.0   1
68   0.5   0.0   1
69   1.0   0.0   0
70   1.5   0.0   1
71   2.5   0.0   1
72   3.0   0.0   0
73   3.5   0.0   1
74   4.5   0.0   1
75   5.0   0.0   0
76  -4.35355339059327373   0.35355339059327373  1
77  -4.0   0.5   1
78  -3.64644660940672627   0.35355339059327373  1
79  -2.35355339059327373   0.35355339059327373  1
80  -2.0   0.5   1
81  -1.64644660940672627   0.35355339059327373  1
82  -0.35355339059327373   0.35355339059327373  1
83   0.0   0.5   1
84   0.35355339059327373   0.35355339059327373  1
85   1.64644660940672627   0.35355339059327373  1
86   2.0   0.5    1
87   2.35355339059327373   0.35355339059327373  1
88   3.64644660940672627   0.35355339059327373  1
89   4.0   0.5   1
90   4.35355339059327373   0.35355339059327373  1
91  -4.65   0.65   0
92  -3.35   0.65   0
93  -2.65   0.65   0
94  -1.35   0.65   0
95  -0.65   0.65   0
96   0.65   0.65   0
97   1.35   0.65   0
98   2.65   0.65   0
99   3.35   0.65   0
100   4.65   0.65   0
101  -5.375   1.0   1
```

```
102 -5.1875  1.0   0
103 -5.0   1.0   0
104 -4.0   1.0   0
105 -3.0   1.0   0
106 -2.0   1.0   0
107 -1.0   1.0   0
108  0.0   1.0   0
109  1.0   1.0   0
110  2.0   1.0   0
111  3.0   1.0   0
112  4.0   1.0   0
113  5.0   1.0   0
114 -5.375  1.1875  1
115 -5.0   1.1875  0
116 -3.0   1.1875  0
117 -1.0   1.1875  0
118  1.0   1.1875  0
119  3.0   1.1875  0
120  5.0   1.1875  0
121 -5.375  1.375  1
122 -5.1875  1.375  1
123 -5.0   1.375  1
124 -4.0   1.375  1
125 -3.0   1.375  1
126 -2.0   1.375  1
127 -1.0   1.375  1
128  0.0   1.375  1
129  1.0   1.375  1
130  2.0   1.375  1
131  3.0   1.375  1
132  4.0   1.375  1
133  5.0   1.375  1
1 3 3
1 1 1
1 1 1
2 3 3
1 1 1
1 1 1
3 16 3
1 1 1 1 1 1 1 1 1 1 1 1 1 1 1 1
1 1 1
4 16 3
1 1 1 1 1 1 1 1 1 1 1 1 1 1 1 1
1 1 1
5 16 3
1 1 1 1 1 1 1 1 1 1 1 1 1 1 1 1
1 1 1
```

```
6 16 3
1 1 1 1 1 1 1 1 1 1 1 1 1 1 1 1
1 1 1
7 16 3
1 1 1 1 1 1 1 1 1 1 1 1 1 1 1 1
1 1 1
8 3 16
1 1 1
1 1 1 1 1 1 1 1 1 1 1 1 1 1 1 1
9 16 3
1 1 1 1 1 1 1 1 1 1 1 1 1 1 1 1
1 1 1
10 16 3
1 1 1 1 1 1 1 1 1 1 1 1 1 1 1 1
1 1 1
11 16 3
1 1 1 1 1 1 1 1 1 1 1 1 1 1 1 1
1 1 1
12 16 3
1 1 1 1 1 1 1 1 1 1 1 1 1 1 1 1
1 1 1
13 16 3
1 1 1 1 1 1 1 1 1 1 1 1 1 1 1 1
1 1 1
14 16 4
1 1 1 1 1 1 1 1 1 1 1 1 1 1 1 1
1 1 1 1
15 16 4
1 1 1 1 1 1 1 1 1 1 1 1 1 1 1 1
1 1 1 1
16 16 4
1 1 1 1 1 1 1 1 1 1 1 1 1 1 1 1
1 1 1 1
17 16 4
1 1 1 1 1 1 1 1 1 1 1 1 1 1 1 1
1 1 1 1
18 16 4
1 1 1 1 1 1 1 1 1 1 1 1 1 1 1 1
1 1 1 1
19 16 4
1 1 1 1 1 1 1 1 1 1 1 1 1 1 1 1
1 1 1 1
20 16 4
1 1 1 1 1 1 1 1 1 1 1 1 1 1 1 1
1 1 1 1
21 16 4
1 1 1 1 1 1 1 1 1 1 1 1 1 1 1 1
```

```
1 1 1 1
22 16 4
1 1 1 1 1 1 1 1 1 1 1 1 1 1 1 1
1 1 1 1
23 16 4
1 1 1 1 1 1 1 1 1 1 1 1 1 1 1 1
1 1 1 1
24 16 4
1 1 1 1 1 1 1 1 1 1 1 1 1 1 1 1
1 1 1 1
25 16 4
1 1 1 1 1 1 1 1 1 1 1 1 1 1 1 1
1 1 1 1
26 16 4
1 1 1 1 1 1 1 1 1 1 1 1 1 1 1 1
1 1 1 1
27 16 4
1 1 1 1 1 1 1 1 1 1 1 1 1 1 1 1
1 1 1 1
28 16 4
1 1 1 1 1 1 1 1 1 1 1 1 1 1 1 1
1 1 1 1
29 16 4
1 1 1 1 1 1 1 1 1 1 1 1 1 1 1 1
1 1 1 1
30 16 4
1 1 1 1 1 1 1 1 1 1 1 1 1 1 1 1
1 1 1 1
31 16 4
1 1 1 1 1 1 1 1 1 1 1 1 1 1 1 1
1 1 1 1
32 16 4
1 1 1 1 1 1 1 1 1 1 1 1 1 1 1 1
1 1 1 1
33 16 4
1 1 1 1 1 1 1 1 1 1 1 1 1 1 1 1
1 1 1 1
```

```matlab
function [matrix_file] = gnu2mat(gnufile, rows, cols)
% This function converts a GNU file generated by the output of the
% code found in the book "Quick Finite Elements for Electromagnetic
% Waves" by Pelosi, Coccioli, Selleri to a matrix format readable
% by Matlab.
%
% Syntax:
%
% filename = gnu2mat(GNU_file, #row, #cols);

% Perry N. Villanueva
% 1 December 1998
%
index = 1;
for i = 1:rows
   for j = 1:cols
      matrix_file(i,j) = gnufile(index);
      index = index + 1;
   end
end

figure
set(gcf, 'Position', [152   289   946   542])

subplot 211
set(gca, 'Units', 'inches')

%FOR FIVE CYLINDER CONFIGURATION (PBF), UNCOMMENT NEXT LINE
set(gca, 'Position', [0.75 3.5 9.55 2.0])
%FOR ELEVEN CYLINDER CONFIGURATION, UNCOMMENT NEXT LINE
% set(gca, 'Position', [0.75 3.25 9.55 2.0])

contour(matrix_file, 8)
grid
axis equal
axis([0 cols 0 rows])
%title('Contour Map')
xlabel('Pixels')
ylabel('Pixels')

subplot 212
waterfall(matrix_file)
```

```
%colormap(gray)
axis([0 cols 0 rows 0 3])
%set(gcf, 'Position', [10    396    945    340])
set(gca, 'Units', 'inches')
set(gca, 'Position', [0.75 0.55 9.55 2.0])
set(gca, 'Position', [0.8500    0.7500    9.5500    2.25000])
view(-4,72)
%title('Field Map')
xlabel('Pixels')
ylabel('Pixels')
rotate3d

%figure
%waterfall(matrix_file)
%axis([0 728 0 88 0 4])
%set(gcf, 'Position', [10    396    945    340])
%set(gca, 'Units', 'inches')
%set(gca, 'Position', [0.8500    0.7500    9.5500    2.25000])
%view(-4,65)
%title('Waterfall Plot of Fields')
%xlabel('Pixels')
%ylabel('Pixels')
```

Bibliography

1. Anderson, E., et al. *LAPACK User's Guide*. Philadelphia, PA: SIAM, 1994.

2. Bayliss, A. and E. Turkel. "Radiation Boundary Conditions for Wave-Like Equations," *Communications on Pure and Applied Mathematics, 33*:707–725 (May 1980).

3. Berenger, J. P. "A Perfectly Matched Layer for the Absorption of Electromagnetic Waves," *Journal of Computational Physics, 114*:185–200 (May 1994).

4. Collins, P. J. *Electromagnetic Scattering from Semi-Infinite Planar Arrays*. PhD dissertation, Air Force Institute of Technology, 1996.

5. Collins, P. J. and J.P. Skinner. "A One-Sided Version of the Poisson Sum Formula for Semi-Infinite Array Green's Function," *IEEE Transactions on Antennas and Propagation, AP-45*:601–607 (April 1997).

6. Cwik, T. and R. Mittra. "The Effects of the Truncation and Curvature of Periodic Surfaces: A Strip Grating," *IEEE Transactions on Antennas and Propagation, AP-36*(5):612–622 (May 1988).

7. Engquist, B. and A. Majda. "Absorbing Boundary Conditions for the Numerical Simulation of Waves," *Mathematics of Computation, 31*(139):629–651 (July 1977).

8. Gedney, S. D., et al. "A Combined FEM/MoM Approach to Analyze the Plane Wave Diffraction by Arbitrary Gratings," *IEEE Transactions on Microwave Theory and Techniques, MTT-40*(2):363–370 (February 1992).

9. Harrington, R. F. *Field Computation by Moment Methods*. Robert E. Krieger Publishing Company, Inc., 1968.

10. McGrath, D. T. *Phased Array Antenna Analysis Using Hybrid Finite Element Methods*. PhD dissertation, Air Force Institute of Technology, 1993.

11. Munk, B. A. *A General Theory of Periodic Surfaces in a Stratified Dielectric Medium*. Technical 715582-4, ElectroScience Laboratory: Ohio State University, February 1986. Generated under contract F33615-83-C-1013 for Aeronautical Systems Division, Wright-Patterson AFB, OH.

12. Pelosi, G., et al. *Quick Finite Elements for Electromagnetic Waves*. Artech House, 1998.

13. Peterson, A. F., et al. *Computational Methods for Electromagnetics*. IEEE/Oxford University Press, 1998.

14. Reddy, J. N. *An Introduction to the Finite Elements for Electrical Engineers* (Second Edition). McGraw-Hill, Inc., 1993.

15. Sacks, Z. S., et al. "A Perfectly Matched Anisotropic Absorber for Use as an Absorbing Boundary Condition," *IEEE Transactions on Antennas and Propagation, AP-43*(12):1461–1464 (December 1995).

16. Silvester, P. P. and R. L. Ferrari. *Finite Elements for Electrical Engineers* (Third Edition). Cambridge University Press, 1996.

17. Silvester, P. P. and G. Pelosi. *Finite Elements for Wave Electromagnetics*. IEEE Press, 1994.

18. Skinner, J. P. "Frequency Selective Sufaces." Class notes for EENG 727 at the Air Force Institute of Technology.

19. Sun, D., et al. "Spurious Modes in Finite-Element Method," *IEEE Antennas and Propagation Magazine*, *37*(5):12–24 (October 1995).

20. Vardaxoglou, J. C. *Frequency Selective Surfaces - Analysis and Design*. Research Studies Press, Ltd., 1997.

21. Volakis, J. L., et al. *Finite Element Method for Electromagnetics: Antennas, Microwave Circuits, and Scattering Applications*. IEEE/Oxford University Press, 1998.

22. Wasylkiwskyj, W. "Mutual Coupling Effects in Semi-Infinite Arrays," *IEEE Antennas and Propagation Magazine*, *AP-21*(5):277–285 (May 1973).

Vita

Captain Perry Nathan F. Villanueva was born the son of Luperio F. and Min Vi Luz F. Villanueva in Manila, Philippines on September 20, 1960. He graduated from the University of the Philippines in 1982 with a Bachelor of Science Degree in Mechanical Engineering.

After a 7-year tour in the U.S. Navy, he attended Memphis State University (now the University of Memphis) in 1990. He graduated with a Bachelor of Science Degree in Electrical Engineering in 1993 and was selected for commissioning in the U.S. Air Force. After graduation from Officer Training School in Maxwell AFB, he was assigned to Wright Laboratory, Wright-Patterson AFB as a research engineer. He conducted research in automatic target recognition of non-cooperative targets. He later on managed the Radar Target Modeling program in support of the Non - Cooperative Target Identification program. He was responsible for developing the DoD's first database of advanced Computer-Aided Design (CAD) aircraft models and synthetic radar signatures. He was awarded the Air Force Commendation Medal for his work.

In August 1997 he was assigned to AFIT to pursue his Master of Science degree in Electrical Engineering specializing in communications and computational electromagnetics, an area of personal interest.

After leaving AFIT he will join the Air Force Information Warfare Center (AFIWC), Air Intelligence Agency (AIA), Kelly AFB, San Antonio, Texas.

Permanent address: 518 S. Alameda Avenue
Azusa, California 91702